Imaging Lymphatics

Beeldvorming van het lymfestelsel

(met een samenvatting in het Nederlands)

Imaging Lymphatics
Meijer, Eelco Franciscus Jacobus
Ph.D. thesis, Utrecht University
Proefschrift met een samenvatting in het Nederlands, Universiteit Utrecht

ISBN/EAN: 978-90-393-6859-6
Cover: Artwork 'Lymphatics' by Dmitriy Kedrin
Printed by: ProefschriftMaken | www.proefschriftmaken.nl
Thesis printing was financially supported by the Department of Surgery at *Gelderse Vallei Hospital* (vakgroep Heelkunde Ziekenhuis Gelderse Vallei)

Imaging Lymphatics

Beeldvorming van het lymfestelsel

(met een samenvatting in het Nederlands)

Proefschrift

ter verkrijging van de graad van doctor aan de Universiteit Utrecht op gezag van de rector magnificus, prof. dr. G.J. van der Zwaan, ingevolge het besluit van het college voor promoties in het openbaar te verdedigen op vrijdag 1 december 2017 des avonds te 6.00 uur

door

Eelco Franciscus Jacobus Meijer

geboren op 13 december 1988 te Rotterdam

Promotor: Prof. dr. I.H.M. Borel Rinkes

Copromotoren: Dr. J. Hagendoorn
Dr. T.P. Padera

The author of this thesis was financially supported by: E.L. Steele Laboratory for Tumor Biology (Padera lab), FY15 Ira J. Spiro Translational Research Program award, Stichting Prof. Michaël-van Vloten Fonds. Financial support was generously offered by the Van Oosterom Onderwijsfonds.

Contents

Introduction

1. Thesis introduction

Parts of this chapter were taken from:

The Lymphatic System in Disease Processes and Cancer Progression

Timothy P. Padera, Eelco F.J. Meijer, and Lance L. Munn

Edwin L. Steele Laboratories, Department of Radiation Oncology, and Cancer Center, Massachusetts General Hospital and Harvard Medical School, Boston, Massachusetts 02114; email: tpadera@steele.mgh.harvard.edu

Annual Review of Biomedical Engineering, 2016 Jul 11;18:125-58.

Research into the development, structure and function of the lymphatic system has been accelerating over the past decade, fueled by the seminal discoveries of the first lymphatic growth factor [1] and markers to help identify lymphatic vessels in tissue [2, 3]. These critical molecular tools have allowed the exploration of formation of the lymphatic system in the embryo [3-5], the growth, maturation and function of lymphatics in the adult [1, 6] and the role of lymphatic vessels in disease processes including cellulitis, neurological disease, rheumatoid arthritis, glaucoma, hypertension, graft rejection, atherosclerosis, lymphedema, and cancer [7-18]. Moreover, interest in the lymphatic system has grown rapidly as its functional role in immune function has become more evident [19-21]. With the advances in research, many questions have arisen. In this thesis, I specifically address several critical unmet needs in the field of lymphatic research by (co-) developing and implementing several state-of-the-art imaging methods to boost our knowledge on lymphatic vessel and lymph node functioning in normal and disease settings.

The lymphatic system is critical for maintaining tissue-fluid balance, transporting antigen and antigen presenting cells to lymph nodes to generate adaptive immune responses, and carrying lipids absorbed in the gut to the blood circulation. Correspondingly, disruption of the lymphatic system can lead to lymphedema, gut malabsorption, and localized immune compromise and infections therefrom (*e.g.* cellulitis). The lymphatic system is also involved in cancer progression, as metastatic cancer cells can spread to lymph nodes through lymphatic vessels. Below, I will discuss the current understanding of the role of the lymphatic system in physiology and cancer.

1. The lymphatic system

Lymph is created from a tissue's extracellular fluid and contains unique components derived from that tissue, reflecting its current functional state. Thus, the composition of lymph will be different when sampled from lymphatic vessels draining different tissues and will change with time as a tissue undergoes physiological or pathological processes. Lymph production occurs as tissue fluid enters initial lymphatic vessels (Figure 1), which consist of a single layer of overlapping endothelial cells on a discontinuous basement membrane, typically with sparse association with perivascular cells. Initial lymphatic endothelial cells (LECs) are connected by button-like intercellular junctions that facilitate the collection of interstitial fluid and its contents [22]. The unique microarchitecture of these oak leaf-shaped LECs create overlapping flaps of adjacent cells which form primary valve structures in the wall of initial lymphatics [23]. When tissue fluid pressure is greater than that in an initial lymphatic, the primary LEC valves open and extracellular fluid freely enters [23, 24]. When the fluid pressure is higher inside the lymphatic vessel, the LEC valves close therewith trapping the newly formed lymph inside. Functionally, the primary LEC flaps act as one-way valves and are critical for the production of lymph. The primary LEC valves also allow for dendritic cells (DCs) to pass through and enter the vessel without requiring integrin adhesion or pericellular proteolysis [25]. Dendritic cells and other antigen presenting cells are attracted to initial lymphatic vessels by local chemokine CCL21 gradients produced by LECs and interstitial flow [26-29]. After entering an initial lymphatic vessel, DCs can interact with and crawl on LECs as they travel to the lymph node [21].

After lymph is produced in initial lymphatic vessels, it travels toward lymph nodes and eventually back to the blood circulation. Vessels proximal to the initial lymphatics—pre-collecting and collecting lymphatic vessels—have an increase in coverage by specialized lymphatic muscle cells (LMCs) [30]. In contrast to initial lymphatic vessels, the LECs in collecting lymphatic vessels have a continuous "zipper-like" junction pattern [22], creating tight junctions and reducing the transport of material across the vessel wall under normal conditions. Collecting lymphatic vessels also contain intraluminal valves, which are composed primarily of ECs and matrix. These valves maintain unidirectional proximal lymph flow by preventing flow distally when closed and functioning properly [31]. The vessel segment between two intraluminal valves is known as a lymphangion, which is the primary pumping structure of the lymphatic system. In physiological conditions, both active pumping by LMCs and passive forces—such as pulsatile blood flow, skeletal or smooth muscle contraction, fluid pressure gradients, and gravity—drive lymph flow [23, 32]. However, in the absence of these passive mechanisms, autonomous LMC-mediated contractions of lymphatics vessels can drive lymph through lymph nodes toward the blood circulation [6, 33]. Many signaling molecules have been shown to regulate lymphatic contractions, including endothelial cell-derived nitric oxide (NO), calcium signaling and certain neurotransmitters [34].

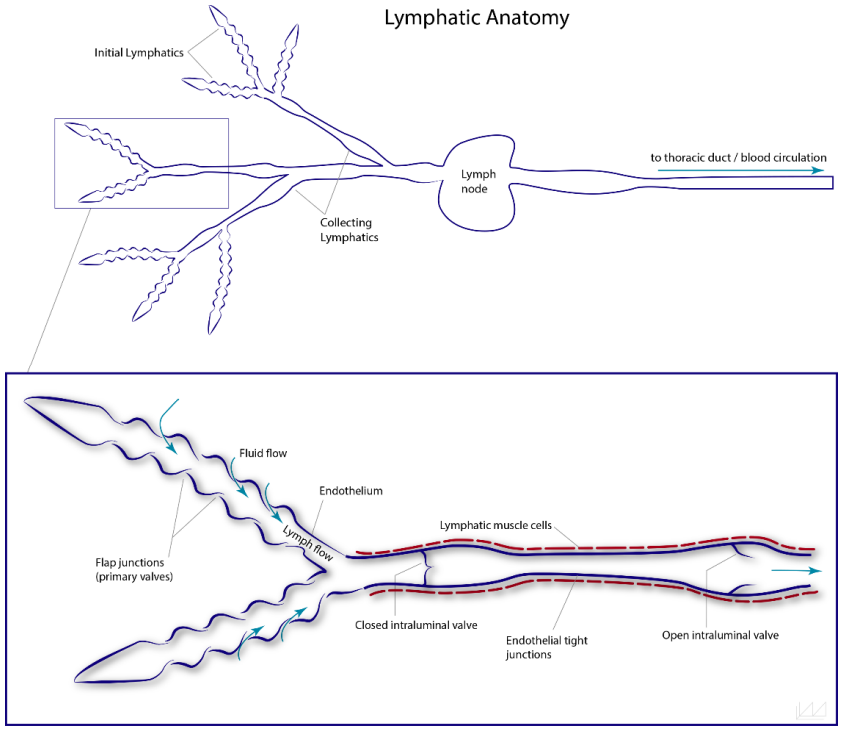

Figure 1. Anatomy of the lymphatic network and valve function. The lymphatic network consists of initial lymphatic vessels—which are responsible for collecting interstitial fluid to create lymph—and collecting lymphatic vessels—which carry fluid from the periphery to lymph nodes. The endothelial cells of initial lymphatic vessels overlap each other to create one-way valves to permit cell and pressure driven fluid entry. The collecting lymphatic vessels are invested in specialized lymphatic muscle cells that contract to drive flow. Intraluminal valves in the collecting lymphatic vessels are critical to preventing back flow. The vessel segment between two valves is called a lymphangion and is the primary pump for lymph flow.

Coordination of lymphatic pumping

The relationship between tissue fluid pressures and lymph drainage has been explored with mathematical models [35-37], and studied *in vivo* by tracking the movement of fluorescent tracers [38]. However, it is not obvious how a series of lymphangions in a lymphatic network can be controlled so that the contractions are coordinated efficiently. In the blood system, a single pump (the heart) drives flow through the diverging arterial network, and the network itself is relatively passive (with the exception of vasodilation, which adjusts vessel diameters to distribute the flow to capillary beds according to local demand). In the lymphatic system, we have the inverse problem: because the network is converging rather that diverging, the individual contractions need to be coordinated along vessels and at branch points so that the system does not "fight against itself". Because of the complexity in driving such a system by long-range nervous system actuation, it seems reasonable that local feedback is primarily responsible for controlling the contractions and relaxations. Lymph flow and fluid pressure are two primary indicators of how well the lymphatic system is functioning. Methods to study lymph flow and lymphangion

coordination *in vivo* to truly unravel the functioning of lymphatic collecting vessels however, are lacking.

Current methods used in research to investigate lymphatic vessel functioning include near infrared fluorescence (NIRF) imaging, direct fluorescence imaging of lymphatic contraction [39, 40] and lymphoscintigraphy. NIRF imaging is used both in research and clinically and can observe how injected contrast moves though lymphatic vessels [41-43]. The technique measures changes in vessel region intensity that likely correspond to lymphatic contraction and/or movement of lymph fluid [44]. Direct fluorescent imaging of lymphatic contraction acquires images at high resolution, allowing for quantification of contraction frequency and the percentage of volume change per contraction (ejection fraction) [39, 45]. Both NIRF and direct fluorescent imaging can visualize lymphatic valves. Lymphoscintigraphy is still considered the gold standard of imaging modalities [15, 46, 47], which uses clearance of radioactive tracers injected intradermally or subcutaneously to quantify lymphatic clearance rates, map aberrant drainage patterns and identify dermal backflow by imaging a location and assessing the increase in signal over time.

Unfortunately, existing methods need injection of a radioactive, fluorescent or chromatic dye into the tissue, perturbing the physiologic state of the lymphatic vessel. Although these methods can be used to look at specific parameters of lymphatic functioning like contractions, valve functioning and fluid transport, they intrinsically change the parameters to be measured and cannot directly quantify lymph flow. Developing a method that could directly quantify lymph flow without injecting any fluid, or one that could look at multiple parameters in several lymphangions, could drastically catalyze our understanding of lymphatic vessel (patho-) physiology. Therefore, we developed an *in vivo* label-free method to measure lymph flow velocity and volumetric flow rates using Doppler optical coherence tomography (DOCT) **(Chapter 4)**. Subsequently, we modified that method to allow for simultaneous measurements of lymphatic vessel contraction, flow and valve dynamics in multiple lymphangions **(Chapter 5)**. The label free method was then employed to evaluate lymphatic function in skin and soft tissue infections, as described in **Chapter 7**.

2. Role of Lymphatic System in Cancer Progression

Lymph Node Metastasis: Clinical Role

Lymph nodes are the most common sites of solid tumor metastases. Their presence signals a poorer prognosis and the recommendation for systemic therapy in most cancer patients. However, why lymph node metastases are such strong predictors of outcome in cancer patients is the subject of much debate. On one hand, it is possible that the presence of cancer cells in lymph nodes simply reflects the ability of the primary tumor to metastasize, and the actual disease in the lymph nodes is inconsequential [48, 49]. On the other hand, the strong predictive power of lymph node metastases could be due to the ability of cancer cells in the lymph node to leave and spread to distant metastatic sites [50-52]. This argument suggests that lymph node metastases need to be treated in order to prevent distant metastasis and ultimately eliminate all disease from the patient [53-55]. For an individual patient, the truth likely lies in between, depending on where in the spectrum of progression to distant metastasis the cancer is diagnosed [56]. The status of distant metastasis in individual patients will determine how much of a role lymph node metastases will play in the outcome for the patient—i.e., whether there is risk of further spread from lymph nodes or whether distant spread has already occurred.

Tumor draining lymphatic vessels

Initially thought to be a passive process, evidence now suggests that lymphatic metastasis is regulated at multiple steps including the attraction and entry of cancer cells to lymphatic vessels and the successful penetration into draining lymph nodes [57]. Solid tumors commonly induce an expansion of the surrounding lymphatic network [14, 58]. However, functional lymphatic vessels are restricted to the tumor margin and peri-tumor regions surrounding tumors [59]. As tumors lack intratumor functional lymphatic vessels, the interstitial fluid pressure is elevated and this can alter lymph flow to tumor draining lymph nodes [12]. In experimental mouse models of cancer, overexpression of lymphangiogenic growth factors VEGF-C and VEGF-D enhanced peripheral tumor lymphatic vessel growth and increased lymph node metastasis [14, 59-61]. This was shown to be a result of an increased number of cancer cells that arrive in the lymph node [12, 62]. CCL21 production by the lymphatic endothelium can also be enhanced by VEGF-C, thereby promoting lymphatic entry of CCR7+ tumor cells [63]. Thus, tumor cells that arrive at the lymphatic vessels may enter passively or by active signaling mechanisms.

After entry of tumor cells into tumor margin initial lymphatic vessels, the cancer cells travel through collecting lymphatic vessels to the lymph node. Tumor-derived VEGF-C/D has been shown to increase the contraction of proximal collecting lymphatic vessels [1], potentially increasing lymph flow and tumor cell dissemination [12, 64]. By preventing tumor induced lymphatic vessel remodeling, the spread of cancer cells to lymph nodes was reduced [12, 62, 65, 66]. In collecting lymphatic vessels draining melanoma, it is thought that lymph flow promotes the spread of “in-transit metastases”—cancer cells that are initially spread locally to tissues between the primary tumor and the lymph nodes—ultimately leading to lymphatic metastasis [67].

Better understanding of lymphatic vessel and lymph node functioning, as well as changes that occur during disease, are of paramount importance in developing therapies to prevent or cure diseases including cancer. A major limitation to study lymph node (patho-) physiology however, was the lack of a model system that would allow for long-term and real time intravital imaging of lymph nodes. Such a model would be extremely valuable in studying lymph node morphology as well as cell behavior in lymph nodes during the generation of immune responses in a variety of disease settings and during the formation of metastatic lesions in cancer bearing mice. Therefore, we developed a chronic lymph node window (CLNW) surgical preparation to facilitate longitudinal intravital imaging of the inguinal lymph node in mice **(Chapter 2)**.

Cancer cell survival in the lymphatic system

Cancer cells that enter the lymphatics need to survive in a low oxygen environment [68, 69]. Cancer cells that subsequently reach the lymph node first encounter the subcapsular sinus (SCS), which is devoid of blood vessels. Here, they experience hypoxia [70] which effects tumor cell metabolism and selects for clones that are more aggressive and metastatic. This selection and adaptation may enable cancer cells to survive in the avascular SCS, spread further in the patient or, alternatively, enter a state of dormancy while in the SCS. Furthermore, it is known that angiogenesis is induced in response to hypoxic environments. However, increases in blood vessel density in lymph node metastasis have not been observed [66, 70-72]. Sprouting angiogenesis was not observed using intravital microscopy to longitudinally follow the growth of spontaneous lymph node metastases in mouse models [70]. Instead, cancer cells in the SCS invaded into the lymph

node where they could utilize the native vasculature of the lymph node. In doing so, these cells no longer experienced hypoxia [70].

Treating lymph node metastases

Although it is known that metastasis remains the major cause of cancer mortality, the challenge of eradicating cancer cells that have spread to lymph nodes or distant organs remains. Seminal discoveries defining the molecular and cellular mechanisms that drive metastasis have yet to improve survival for many patients with metastatic disease. One limitation is that most anti-cancer drugs are optimized by studying the primary tumor growing in its native microenvironment. It is well known that the local microenvironment in which tumor cells grow greatly affects the growth rate, metabolism, vascularization, immune response and ultimately response to therapy. Thus, drugs designed to work in the primary tumor are less effective in treating metastasis. Pre-clinical and clinical studies show that lymph node metastases and primary tumors can respond differently to the same therapeutic regimen [62, 70, 73-76]. Systematic studies of drug penetration into lymph nodes are lacking, and could offer a better understanding. Therefore, by implementing the CLNW and using multiphoton microscopy, we developed a method to measure vascular permeability *in vivo* **(Chapter 3).** We then employed this method to investigate and alter lymph node effective vascular permeability and its effects on chemotherapy penetration in the lymph node (**Chapter 6)**.

References

1. Zheng, W., A. Aspelund, and K. Alitalo, Lymphangiogenic factors, mechanisms, and applications. J Clin Invest, 2014. 124(3): p. 878-87.
2. Banerji, S., et al., LYVE-1, a new homologue of the CD44 glycoprotein, is a lymph-specific receptor for hyaluronan. J Cell Biol, 1999. 144(4): p. 789-801.
3. Wigle, J.T. and G. Oliver, Prox1 function is required for the development of the murine lymphatic system. Cell, 1999. 98(6): p. 769-78.
4. Martinez-Corral, I., et al., Nonvenous origin of dermal lymphatic vasculature. Circ Res, 2015. 116(10): p. 1649-54.
5. Yang, Y. and G. Oliver, Development of the mammalian lymphatic vasculature. J Clin Invest, 2014. 124(3): p. 888-97.
6. Zawieja, D.C., Contractile physiology of lymphatics. Lymphat Res Biol, 2009. 7(2): p. 87-96.
7. Iliff, J.J., et al., A Paravascular Pathway Facilitates CSF Flow Through the Brain Parenchyma and the Clearance of Interstitial Solutes, Including Amyloid β. Sci Transl Med, 2012. 4(147): p. 147ra111.
8. Li, J., et al., Efficacy of B cell depletion therapy for murine joint arthritis flare is associated with increased lymphatic flow. Arthritis Rheum, 2013. 65(1): p. 130-8.
9. Aspelund, A., et al., The Schlemm's canal is a VEGF-C/VEGFR-3–responsive lymphatic-like vessel. The Journal of Clinical Investigation, 2014. 124(9): p. 3975-3986.
10. Wiig, H., et al., Immune cells control skin lymphatic electrolyte homeostasis and blood pressure. The Journal of Clinical Investigation, 2013. 123(7): p. 2803-2815.
11. Klotz, L., et al., Cardiac lymphatics are heterogeneous in origin and respond to injury. Nature, 2015. 522(7554): p. 62-67.
12. Hoshida, T., et al., Imaging steps of lymphatic metastasis reveals that vascular endothelial growth factor-C increases metastasis by increasing delivery of cancer cells to lymph nodes: therapeutic implications. Cancer Res, 2006. 66(16): p. 8065-75.

13. Dieterich, L.C., C.D. Seidel, and M. Detmar, Lymphatic vessels: new targets for the treatment of inflammatory diseases. Angiogenesis, 2014. 17(2): p. 359-71.
14. Skobe, M., et al., Induction of tumor lymphangiogenesis by VEGF-C promotes breast cancer metastasis. Nat Med, 2001. 7(2): p. 192-8.
15. Mortimer, P.S. and S.G. Rockson, New developments in clinical aspects of lymphatic disease. J Clin Invest, 2014. 124(3): p. 915-21.
16. Hos, D., et al., Antilymphangiogenic therapy to promote transplant survival and to reduce cancer metastasis: what can we learn from the eye? Semin Cell Dev Biol, 2015. 38: p. 117-30.
17. Goel, S., et al., Effects of vascular-endothelial protein tyrosine phosphatase inhibition on breast cancer vasculature and metastatic progression. J Natl Cancer Inst, 2013. 105(16): p. 1188-201.
18. Pereira, E.R., et al., The lymph node microenvironment and its role in the progression of metastatic cancer. Semin Cell Dev Biol, 2015. 38: p. 98-105.
19. Card, C.M., S.S. Yu, and M.A. Swartz, Emerging roles of lymphatic endothelium in regulating adaptive immunity. J Clin Invest, 2014. 124(3): p. 943-52.
20. Tewalt, E.F., et al., Lymphatic endothelial cells induce tolerance via PD-L1 and lack of costimulation leading to high-level PD-1 expression on CD8 T cells. Blood, 2012. 120(24): p. 4772-82.
21. Teijeira, A., E. Russo, and C. Halin, Taking the lymphatic route: dendritic cell migration to draining lymph nodes. Semin Immunopathol, 2014. 36(2): p. 261-74.
22. Baluk, P., et al., Functionally specialized junctions between endothelial cells of lymphatic vessels. J Exp Med, 2007. 204(10): p. 2349-62.
23. Schmid-Schonbein, G.W., Microlymphatics and lymph flow. Physiological Reviews, 1990. 70(4): p. 987-1028.
24. Witte, M.H., et al., Lymphangiogenesis and lymphangiodysplasia: from molecular to clinical lymphology. Microsc Res Tech, 2001. 55(2): p. 122-45.
25. Pflicke, H. and M. Sixt, Preformed portals facilitate dendritic cell entry into afferent lymphatic vessels. J Exp Med, 2009. 206(13): p. 2925-35.
26. Randolph, G.J., V. Angeli, and M.A. Swartz, Dendritic-cell trafficking to lymph nodes through lymphatic vessels. Nat Rev Immunol, 2005. 5(8): p. 617-28.
27. Schumann, K., et al., Immobilized chemokine fields and soluble chemokine gradients cooperatively shape migration patterns of dendritic cells. Immunity, 2010. 32(5): p. 703-13.
28. Miteva, D.O., et al., Transmural flow modulates cell and fluid transport functions of lymphatic endothelium. Circ Res, 2010. 106(5): p. 920-31.
29. Weber, M., et al., Interstitial dendritic cell guidance by haptotactic chemokine gradients. Science, 2013. 339(6117): p. 328-32.
30. von der Weid, P.Y. and D.C. Zawieja, Lymphatic smooth muscle: the motor unit of lymph drainage. Int J Biochem Cell Biol, 2004. 36(7): p. 1147-53.
31. Davis, M.J., et al., Determinants of valve gating in collecting lymphatic vessels from rat mesentery. Am J Physiol Heart Circ Physiol, 2011. 301(1): p. H48-60.
32. Skalak, T.C., G.W. Schmid-Schonbein, and B.W. Zweifach, New morphological evidence for a mechanism of lymph formation in skeletal muscle. Microvasc Res, 1984. 28(1): p. 95-112.

33. Eisenhoffer, J., et al., Importance of valves and lymphangion contractions in determining pressure gradients in isolated lymphatics exposed to elevations in outflow pressure. Microvasc Res, 1995. 49(1): p. 97-110.
34. Gasheva, O.Y., D.C. Zawieja, and A.A. Gashev, Contraction-initiated NO-dependent lymphatic relaxation: a self-regulatory mechanism in rat thoracic duct. J Physiol, 2006. 575(Pt 3): p. 821-32.
35. Margaris, K.N. and R.A. Black, Modelling the lymphatic system: challenges and opportunities. J R Soc Interface, 2012. 9(69): p. 601-12.
36. Baxter, L.T. and R.K. Jain, Transport of fluid and macromolecules in tumors. I. Role of interstitial pressure and convection. Microvasc Res, 1989. 37(1): p. 77-104.
37. Roose, T. and M.A. Swartz, Multiscale modeling of lymphatic drainage from tissues using homogenization theory. J Biomech, 2012. 45(1): p. 107-15.
38. Hagendoorn, J., et al., Endothelial nitric oxide synthase regulates microlymphatic flow via collecting lymphatics. Circ Res, 2004. 95(2): p. 204-9.
39. Liao, S., et al., Method for the quantitative measurement of collecting lymphatic vessel contraction in mice. J Biol Methods, 2014. 1(2).
40. Robinson, H.A., et al., Non-invasive Optical Imaging of the Lymphatic Vasculature of a Mouse. J Vis Exp, 2013(73).
41. Brandon Dixon, J. and M.J. Weiler, Bridging the divide between pathogenesis and detection in lymphedema. Semin Cell Dev Biol, 2015. 38: p. 75-82.
42. Tiwari, P., et al., Breast and gynecologic cancer-related extremity lymphedema: a review of diagnostic modalities and management options. World J Surg Oncol, 2013. 11: p. 237.
43. Rahimi, H., et al., Lymphatic imaging to assess rheumatoid flare: mechanistic insights and biomarker potential. Arthritis Res Ther, 2016. 18: p. 194.
44. Sevick-Muraca, E.M., S. Kwon, and J.C. Rasmussen, Emerging lymphatic imaging technologies for mouse and man. J Clin Invest, 2014. 124(3): p. 905-14.
45. Proulx, S.T., et al., Use of a PEG-conjugated bright near-infrared dye for functional imaging of rerouting of tumor lymphatic drainage after sentinel lymph node metastasis. Biomaterials, 2013. 34(21): p. 5128-37.
46. Chong, C., et al., In vivo visualization and quantification of collecting lymphatic vessel contractility using near-infrared imaging. Sci Rep, 2016. 6: p. 22930.
47. Weiler, M., T. Kassis, and J.B. Dixon, Sensitivity analysis of near-infrared functional lymphatic imaging. J Biomed Opt, 2012. 17(6).
48. Liao, S., et al., Impaired lymphatic contraction associated with immunosuppression. Proc Natl Acad Sci U S A, 2011. 108(46): p. 18784-9.
49. Cady, B., Regional lymph node metastases; a singular manifestation of the process of clinical metastases in cancer: contemporary animal research and clinical reports suggest unifying concepts. Ann Surg Oncol, 2007. 14(6): p. 1790-800.
50. Fisher, B., et al., Twenty-five-year follow-up of a randomized trial comparing radical mastectomy, total mastectomy, and total mastectomy followed by irradiation. N Engl J Med, 2002. 347(8): p. 567-75.
51. Halsted, W.S., I. The Results of Radical Operations for the Cure of Carcinoma of the Breast. Ann Surg, 1907. 46(1): p. 1-19.
52. Cascinelli, N., et al., Immediate or delayed dissection of regional nodes in patients with melanoma of the trunk: a randomised trial. WHO Melanoma Programme. Lancet, 1998. 351(9105): p. 793-6.

53. Starz, H., et al., A micromorphometry-based concept for routine classification of sentinel lymph node metastases and its clinical relevance for patients with melanoma. Cancer, 2001. 91(11): p. 2110-21.
54. Clarke, M., et al., Effects of radiotherapy and of differences in the extent of surgery for early breast cancer on local recurrence and 15-year survival: an overview of the randomised trials. Lancet, 2005. 366(9503): p. 2087-106.
55. Falkson, C.B., How do I deal with the axilla in patients with a positive sentinel lymph node? Curr Treat Options Oncol, 2011. 12(4): p. 389-402.
56. Morton, D.L., et al., Final trial report of sentinel-node biopsy versus nodal observation in melanoma. N Engl J Med, 2014. 370(7): p. 599-609.
57. Hellman, S., Karnofsky Memorial Lecture. Natural history of small breast cancers. J Clin Oncol, 1994. 12(10): p. 2229-34.
58. Podgrabinska, S. and M. Skobe, Role of lymphatic vasculature in regional and distant metastases. Microvasc Res, 2014. 95C: p. 46-52.
59. Stacker, S.A., et al., Lymphangiogenesis and lymphatic vessel remodelling in cancer. Nat Rev Cancer, 2014. 14(3): p. 159-72.
60. Padera, T.P., et al., Lymphatic metastasis in the absence of functional intratumor lymphatics. Science, 2002. 296(5574): p. 1883-6.
61. Karpanen, T., et al., Vascular endothelial growth factor C promotes tumor lymphangiogenesis and intralymphatic tumor growth. Cancer Res, 2001. 61(5): p. 1786-90.
62. Stacker, S.A., et al., VEGF-D promotes the metastatic spread of tumor cells via the lymphatics. Nat Med, 2001. 7(2): p. 186-91.
63. Padera, T.P., et al., Differential response of primary tumor versus lymphatic metastasis to VEGFR-2 and VEGFR-3 kinase inhibitors cediranib and vandetanib. Mol Cancer Ther, 2008. 7(8): p. 2272-9.
64. Issa, A., et al., Vascular endothelial growth factor-C and C-C chemokine receptor 7 in tumor cell-lymphatic cross-talk promote invasive phenotype. Cancer Res, 2009. 69(1): p. 349-57.
65. Gogineni, A., et al., Inhibition of VEGF-C modulates distal lymphatic remodeling and secondary metastasis. PLoS One, 2013. 8(7): p. e68755.
66. Karnezis, T., et al., VEGF-D promotes tumor metastasis by regulating prostaglandins produced by the collecting lymphatic endothelium. Cancer Cell, 2012. 21(2): p. 181-95.
67. Roberts, N., et al., Inhibition of VEGFR-3 activation with the antagonistic antibody more potently suppresses lymph node and distant metastases than inactivation of VEGFR-2. Cancer Res, 2006. 66(5): p. 2650-7.
68. Tammela, T., et al., Photodynamic ablation of lymphatic vessels and intralymphatic cancer cells prevents metastasis. Sci Transl Med, 2011. 3(69): p. 69ra11.
69. Barankay, T., et al., Oxygen pressure in small lymphatics. Pflugers Arch, 1976. 366(1): p. 53-9.
70. Hangai-Hoger, N., et al., Microlymphatic and tissue oxygen tension in the rat mesentery. Am J Physiol Heart Circ Physiol, 2004. 286(3): p. H878-83.
71. Jeong, H.S., et al., Investigation of the Lack of Angiogenesis in the Formation of Lymph Node Metastases. J Natl Cancer Inst, 2015. 107(9).

72. Arapandoni-Dadioti, P., et al., Angiogenesis in ductal breast carcinoma. Comparison of microvessel density between primary tumour and lymph node metastasis. Cancer Lett, 1999. 137(2): p. 145-50.
73. Naresh, K.N., A.Y. Nerurkar, and A.M. Borges, Angiogenesis is redundant for tumour growth in lymph node metastases. Histopathology, 2001. 38(5): p. 466-70.
74. Akita, H., et al., Effects of neoadjuvant chemotherapy on primary tumor and lymph node metastasis in esophageal squamous cell carcinoma: additive association with prognosis. Dis Esophagus, 2009. 22(4): p. 291-7.
75. Medich, D., et al., Preoperative chemoradiotherapy and radical surgery for locally advanced distal rectal adenocarcinoma: pathologic findings and clinical implications. Dis Colon Rectum, 2001. 44(8): p. 1123-8.
76. Kuerer, H.M., et al., Clinical course of breast cancer patients with complete pathologic primary tumor and axillary lymph node response to doxorubicin-based neoadjuvant chemotherapy. J Clin Oncol, 1999. 17(2): p. 460-9.
77. Cox, C., et al., What is the burden of axillary disease after neoadjuvant therapy in women with locally advanced breast cancer? Curr Oncol, 2013. 20(2): p. 111-7.

Part I: Imaging methods

2. Murine chronic lymph node window for longitudinal intravital lymph node imaging

Eelco FJ Meijer[1,5], Han-Sin Jeong[2,5], Ethel R Pereira[1], Thomas A Ruggieri[3], Cedric Blatter[4], Benjamin J Vakoc[4] & Timothy P Padera[1]

[1] Edwin L. Steele Laboratories, Department of Radiation Oncology, and Cancer Center, Massachusetts General Hospital and Harvard Medical School, Boston, Massachusetts, USA. [2] Department of Otorhinolaryngology–Head and Neck Surgery, Samsung Medical Center, Sungkyunkwan University School of Medicine, Seoul, South Korea. [3] Radiation Medicine Machine Shop, Department of Radiation Oncology, and Cancer Center, Massachusetts General Hospital and Harvard Medical School, Boston, Massachusetts, USA. [4] Wellman Center for Photomedicine, Department of Dermatology, Massachusetts General Hospital and Harvard Medical School, Boston, Massachusetts, USA. [5] These authors contributed equally to this work. Correspondence should be addressed to T.P.P. (tpadera@steele.mgh.harvard.edu).

Nature Protocols, 2017. 12(8): p. 1513-1520.
Full text and supplementary files openly available at http://rdcu.be/tYX0

Abstract
Chronic imaging windows in mice have been developed to allow intravital microscopy of multiple organs and have proven to be of paramount importance in advancing our knowledge of normal and disease processes. However, a model system that allows long-term intravital imaging of lymph nodes had previously not been developed. This was a major limitation in the study of cell behavior in lymph nodes during the generation of immune responses in a variety of disease settings and during the formation of metastatic lesions in cancer bearing mice. We describe a chronic lymph node window (CLNW) surgical preparation to facilitate intravital imaging of the inguinal lymph node in mice. The CLNW allows stable longitudinal imaging without the need for serial surgeries while preserving lymph node blood and lymph flow. The entire procedure takes approximately half an hour per mouse, and subsequently allows for longitudinal intravital imaging of the murine lymph node and surrounding structures for up to fourteen days. Small animal surgery experience is required to successfully carry out the protocol.

Introduction

Our protocol describes the surgical preparation and implantation of a chronic lymph node window (CLNW) in mice [1], as well as the design of the titanium CLNW frame, processes for using the CLNW with intravital microscopes and advice for post procedural follow-up. The subiliac (inguinal) lymph node of the mouse, which is situated in the fold of the flank (regio inguinalis) cranial to the thigh musculature [2], is revealed in this window preparation.

Ex vivo studies and intravital microscopy of the dynamic microenvironment of the lymph node has expanded our understanding of immune cell interactions [3-8]. This pioneering microscopy work utilized acute lymph node preparations that allowed lymph node imaging over several hours. However, to study the development of lymph node metastasis and immune cell trafficking in adaptive immune responses, longitudinal imaging is needed over days and weeks. Previously, an internal lymph node window was created to study the progression of lymphoma [9]. However, this method required successive surgeries to expose the imaging window. Motivated by these seminal methods, we developed the CLNW surgical preparation [1] to facilitate imaging of lymph node anatomy, cancer cell growth and immune cell trafficking over the course of fourteen days.

Applications of the method:

The CLNW was designed to be used in conjunction with intravital microscopy. Intravital microscopy of secondary lymphoid organs has proven valuable in understanding immune cell function and activation [3, 7, 8], as well as malignancy [1, 9]. Other applications may include studying or labelling blood and lymph to understand fluid and antigen flows in the lymph node [10, 11], as well as immune and tumor cell trafficking. Multiphoton microscopy (MPM) has proven useful because of its superior tissue penetration *in vivo* [12, 13] when compared to other fluorescence based techniques of similar spatial resolution. Images can be created in the CLNW from depths of several hundred microns using MPM *in vivo* [1]. Optical coherence tomography (OCT) [14-16] can be used for deeper imaging of the lymph node in the CLNW, although this technique has less spatial resolution at the current time.

Comparison with other chronic windows:

There are multiple chronic windows available for intravital microscopy, and each is optimized for its targeted organ. The mammary fat pad window [17] has been developed to study healthy and tumorigenic mammary tissue in mice [18]. The dorsal skinfold chamber is used to image the subcutaneous tissue as well as tumor growth in the skin [19, 20]. The cranial window, created by replacing a portion of the mouse skull with a glass coverslip that is permanently secured to the skull with glue, is used to image the brain [21]. Other chronic windows developed for imaging the nervous system include a mouse spinal cord window [22] and a rat peripheral nerve window [23], which transposes the sciatic nerve to surrounding muscle tissue, providing stable access to this nerve. Lastly, an abdominal imaging window has been developed to chronically image abdominal organs [24]. Our CLNW is comparable to these windows in concept. To image the inguinal lymph node using intravital microscopy as previously described in Jeong H. *et al*. [1], we modified the chronic mammary fat pad window model. Similar to the mammary and abdominal imaging windows, we allow for cover slip replacement in the CLNW, giving access to the tissue (e.g. for cleaning or experimental manipulation) without having to adjust the surgical preparation. This capability allows better image acquisition over time. Similar to other window chambers, we use

titanium for its known biocompatibility and favorable strength to weight properties. The CLNW and its schematic design are shown in Figure 1 and Supplementary Figures 1-3, respectively.

Limitations

The CLNW implantation will impair leg movement in mice below approximately 25 grams (age 6-8 weeks). The procedure is considered major surgery and therefore animals need time to recover before additional anesthesia is administered for imaging. We allow the animal to recover for 48 hours after surgery before imaging begins while administrating acetaminophen chronically in accordance with recommendations from the Massachusetts General Hospital (MGH) Institutional Animal Care and Use Committee (IACUC).

The inguinal LN has minimal morphological, cellular and biochemical changes for the first 14 days after CLNW implantation as described by Jeong H. *et al*. [1]. Briefly, local inflammation and vascular remodeling is microscopically absent in the physiologic lymph node post CLNW implantation as shown by imaging and immunofluorescent staining. In addition, lymphotoxin beta receptor (LTbR) and tumor necrosis factor (TNF) expression remains low for two weeks postoperatively (see Supplementary Figure 1d in Jeong H. *et al*. [1]). A transient increase in IFNg was noted two days postoperatively but returned to baseline short thereafter. Together, these data indicate that some transient regional inflammation due to the surgery is to be expected at day 2 postoperatively, which is resolved by day 4. Thereafter stable levels of inflammatory cytokines and little to no changes in lymph node architecture are to be expected. Based on longitudinal SHG imaging of collagen in the CLNW, fibrillar collagen content or organization does not change due to the presence of the CLNW. Further, we characterized the immune cell populations by flow cytometry data in Balb/c mice on days 2, 7 and 14 after CLNW implantation in comparison to mice without CLNW implantation (Supplementary Figure 4). These data show no significant changes in the total $CD45^+$ cell populations through day 7, although by day 14 there are differences in the number of $CD45^+$ cells, as well as in many $CD45^+$ subpopulations (Supplementary Figure 4c). After 14 days in animals where all subcutaneous fat covering the lymph node was removed, mild inflammation and gradual loss of perfusion in cortical blood vessels becomes apparent and therefore it is not recommended to continue to image in these animals.

This preparation provides visual access predominantly to the lymph node cortical region. With sufficient practice, a surgical success rate of 100% is achievable and significant movement of the lymph node over days can be prevented, although slight rotational changes cannot always be avoided. Therefore, we suggest using an imaging method that can acquire images in both horizontal and vertical axes to always be able to identify the same imaging region.

Experimental design

For optimal microscopy, the optical clarity of the CLNW is critical. The coverslip can be replaced when tissue exudate impairs image quality without altering the surgical preparation. This is accomplished based on the design of the titanium frame in which the coverslip is secured through the use of a tension C-ring. When employing imaging modalities using water immersion objectives, the cover slip should have precise dimensions to prevent leakage of water. When mounted to an imaging stage, the titanium frame prevents respiratory movement during imaging, permitting high-resolution imaging *in vivo*.

The titanium frame can cause skin damage on the ventral side, therefore a layer of surgical tape wrapped around the side of the ventral titanium frame will prevent unnecessary harm to the animal and improve the experimental conditions (Figure 2d-f). For longer-term experiments, the cover slip may cause superficial damage to the lymph node if the subcutaneous fat overlying the lymph node is removed, apparent from the gradual loss of perfusion in cortical blood vessels starting after 14 days. Depending on the question to be answered and keeping in mind the limitations of the imaging modality used, the direct exposure of the lymph node to the cover slip can be adjusted by the timing of when the subcutaneous fat is removed and the amount of fat removed. Complete removal of subcutaneous fat covering the lymph node will allow for at least 14 days of imaging, and all experiments described in this protocol were performed with complete removal of the subcutaneous fat covering the lymph node.

We have developed an imaging stage specifically designed for the CLNW to prevent (large) rotational changes, as well as respiratory movement (Supplementary Figures 5-10). Sequential imaging of the same location over multiple days is achieved at the macro-scale by returning to the same position within the CLNW as the lymph node will remain in place if the CLNW is implanted correctly. If needed, a small ink mark on the cover glass can be made to circumscribe the previous imaging area. At the micro-scale, the same location can be found by tracking anatomical landmarks, such as blood vessels and collagen structure (Figure 3). This works well for frequent imaging sessions in tissue not undergoing large scale remodeling.

In lymph nodes with extensive vascular remodeling, identifying collagen structure by second harmonic generation (SHG) imaging or larger unchanged blood vessels can help to image identical regions over time (Figure 3). In lymph nodes with extensive expansion, (*e.g.* caused by experimental inflammation models or metastasis) the cover slip will keep the lymph node in its same general orientation with respect to the imaging window. This is important for lymph nodes undergoing large changes due to inflammation, adaptive immune response or growth of metastatic cancer. With these scenarios, the ability to measure micro-level changes is less meaningful compared to the massive changes in cellular content and general architecture of the node. The CLNW allows for the kinetics of these processes to be monitored in a more efficient and controlled manner than could be achieved by looking collectively at cohorts of similarly treated animals at staggered time points.

Animals are not expected to have reduced vital signs or body weight. The researcher should be experienced with the surgery to get reproducible results. For experiments where pharmacological treatments are included, animals with and without CLNW should be compared to look at possible overall health effects of the CLNW and analgesics. When looking at effects using *in vivo* imaging, treated CLNW implanted animals should be compared to non-treated CLNW implanted animals.

Materials

REAGENTS

CRITICAL All reagents and equipment can be substituted with appropriate alternatives from other manufacturers.

- Mice: preferably aged 8-10 weeks or older and at least 25g. Strain and sex are dependent on experiment. We have successfully used C3H mice, BALB/c mice, C57BL/6 mice, Nude mice and

mice from a mixed background. All mice were bred and kept in our animal facility. We obtained institutional approval for this procedure from the MGH IACUC.
CAUTION: All animal studies must be reviewed and approved by the relevant local IACUC for your institution and conform to all relevant ethics regulations.

- Cell lines (optional): 4T1 mammary carcinoma cells (ATCC, cat. no. CRL-2539), B16-F10 melanoma cells (ATCC, cat. no. CRL-6475) and SCCVII squamous cell carcinoma cells (originally established in the E.L. Steele Laboratories, MGH, Boston, MA). Cell lines can be stored in liquid nitrogen, aliquoted in cryogenic storage vials.

- Dulbecco's Modified Eagle Medium (DMEM) (ThermoFisher Scientific, cat. no. 11965118): This compound can be stored at 2-8 ºC 12 months from date of manufacture if protected from light.

- Fetal Bovine Serum (FBS) (ThermoFisher Scientific, cat. no. 10437036): This compound can be stored at -5 to -20 ºC until the date of expiration.

- Buprenorphine hydrochloride (McKesson, cat. no. 54017713): This compound can be stored at room temperature (20 ºC) until the date of expiration.
CAUTION: This substance may cause prolonged respiratory depression. Wear protective clothing to avoid contact or inhalation. Buprenorphine is a controlled substance and should be handled accordingly.

- Acetaminophen: (McKesson cat. no. 633792). This compound can be stored at room temperature (20 ºC) until the date of expiration.
CAUTION: While correct dosing should be safe, overdosing can result in significant morbidity and mortality. To prevent overdosing, apply only to drinking water at 1mg/mL. Do not inject or gavage.

- Ketamine (McKesson cat. no. 409205310). This compound can be stored at room temperature (20 ºC) until the date of expiration.
CAUTION: Ketamine may cause prolonged respiratory depression. Ketamine is a controlled substance and should be handled accordingly. Inject intraperitoneally or subcutaneously.

- Xylazine (Webster, cat. no. 200204.00). This compound can be stored at room temperature (20 ºC) until the date of expiration.
CAUTION: Xylazine may cause prolonged respiratory depression. Xylazine is a controlled substance and should be handled accordingly. Inject intraperitoneally or subcutaneously.

- Ophthalmic ointment (Patterson, cat. no. 07-8882572). This compound can be stored at room temperature (20 ºC) until the date of expiration.

- Hair removal cream (CVSpharmacy, cat. no. 339826). This compound can be stored at room temperature (20 ºC) until the date of expiration.

- Glue (Krazy glue, Staples, cat. no. 654643)

- Tetramethylrhodamine-dextran (ThermoFisher Scientific, cat. no. D7139). For long-term storage, divide the aqueous solution into 1 mL 1% aliquots in sterile phosphate buffered saline and freeze at ≤ –20°C. This compound can be stored ≤ –20°C until the date of expiration.
CAUTION: Avoid repeated freezing and thawing. This compound can be stored at 2-6 °C for several weeks if protected from light.

Equipment:
- Gauze sponge (Owens & Minor, cat. no. 4352NON25334)
- Scalpel #10 (Fisher Scientific, cat. no. 08-916-5A)
- Custom-made titanium frame (Figure 1; Supplementary Figure 1)
- Custom-made titanium ring (Figure 1; Supplementary Figure 2)
- Tension C-ring insert (McMASTER, cat. no. 91580A146)
- M2x6 socket cap screws (McMASTER, cat. no. 91290A013)
- M2 nuts (McMASTER, cat. no. 94150A305)
- 5-0 polypropylene sutures (Owens & Minor, cat. no. X698G)
- Sterile cotton swabs (Owens & Minor, cat. no. 1314WOD1002)
- Coverslips, 11.7mm (Fisher Scientific, custom-made)
- Insulin syringe, 1 ml (BD Micro-Fine, cat. no. 329412)
- Microdissection scissors, 3.5 inch (Roboz Surgical, RS-5880)
- Scissors (Roboz Surgical, RS-5960)
- 2 Dumont forceps, no. 5 (WPI, cat. no. 500233)
- Heating pad (Shor-line, cat. no. 912.1000.05)
- Needle holder (Symmetry surgical, cat. no. 36-1006)
- Surgical tray (WPI, cat. no. 500254)
- Nitrile gloves (Fisher scientific, cat. no 19-166-107)
- Cautery (Cardinal Health, cat. no. 65410-185)
- Surgical bright-field microscope (Olympus America, cat. no. BIO-16700834)
- Shaving device (Patterson, cat. no. 07-858-3431)
- Laminar flow hood (DEL Lab Products, cat. no. 30909)
- Surgical tape (Owens & Minor, cat. no. 4509015270)
- Sterile saline for injection (McKesson Medical-Surgical Inc, cat. no. 239930)
- Sterile water (Owens & Minor, cat. no. 0706-2F7113)
- Scale, capable of measuring mouse weight (Fisher Scientific, cat. no. 01-919-33)
- Nutdriver M3 size (McMASTER, cat. no. 52965A23)
- Ring plier (Lawson, cat. no. 95436)

Equipment setup:
- Surgical station: The surgery must be performed in an aseptic working environment. Therefore, we recommend performing surgery in a laminar flow hood with sterile equipment inside, practicing sterile surgical technique.

- Surgical kit preparation: All items must be sterilized before surgery. Instruments to be sterilized are: the surgical tray, microdissection scissors, scissors, two Dumont no. 5 forceps, the needle holder and all CLNW components including coverslips.

- Animal housing: All animals are to be caged separately postoperatively. Food should be placed directly on the bedding and a cage discouraging climbing is preferred to prevent the animal getting stuck due to the titanium chamber. Mouse well-being should be monitored per the relevant guidelines and regulations in place.

- Anesthesia: Mix ketamine and xylazine with sterile saline to obtain a concentration of 100 mg/ml for ketamine and 10 mg/ml for xylazine in a single dilution. The ketamine/xylazine mixture can be stored for up to 3 months at room temperature (20 ºC).

Procedure:
Preparation. TIMING 5-60 minutes.

1 Option A in this step is optional, depending on whether spontaneous metastatic lymph nodes are to be studied.

A Murine tumor cell lines can be used to generate spontaneous inguinal lymph node metastasis in various immune-competent mouse strains. 4T1 mammary carcinoma cells can be implanted in the fourth mammary fat pad of BALB/c mice. B16-F10 melanoma cells can be implanted subcutaneously in the flank (caudal of inguinal lymph node) of C57BL/6 mice. SCCVII squamous cell carcinoma cell from the buccal mucosa can be grown subcutaneously in the flank of C3H/HeJ mice. Implant each cell line at a concentration of 0.1×10^6 cells/animal in 30µl DMEM with 10% FBS. Cell line implantation and subsequent CLNW implantation was reviewed and approved the IACUC at MGH. After primary tumors metastasize to lymph nodes (~7-10 days), the CLNW can be implanted.

B Add acetaminophen 1mg/ml to drinking water two days pre-operatively. Sterilize all necessary equipment.

Pre-operative. TIMING 10 minutes.

2 Place the mouse on the scale to weigh. Anaesthetize the mouse using the ketamine/xylazine mixture of 100mg/10mg per kg body weight. Maintain 37ºC body temperature throughout the procedure using a heating pad at 39ºC. Apply ophthalmic ointment on both eyes.

3 Remove hair by shaving the mouse between regio femoris, regio hypochondriaca, and both ventral and dorsal midline (Figure 2a). Subsequently, apply hair removal cream. Remove the cream after 30-60 seconds with sterile water and cotton gauze to prevent chemical skin burn.

Surgery. TIMING 15 minutes.
CRITICAL The surgical preparation is depicted in Figure 2.

4 Pull a suture through the left-most of the smaller holes of the CLNW frame. Place the suture above the subiliac lymph node 2 mm from the edge of the regio plicae genus with the mouse in supine position and secure the CLNW in this position with a surgical knot (Figure 2b-c, white arrow). The lymph node location (Figure 2b-d, yellow asterisk) can be noninvasively determined by highlighting the lymph node through the skin with bright light from the dorsal side, while looking at the ventral side. If the lymph node is not visible, use the nipple of the 4th mammary fat

pad to approximate its position. Optimal positioning of this suture is important for getting the lymph node centred in the imaging window.

5 Place two screws through the most lateral holes in the CLNW and secure them by tightening one nut each to the frame. Starting with the screw closest to the leg, pierce the skin directly above the screw using a scalpel or scissors and place the screw through the hole. Repeat for the second screw (Figure 2c).
See TROUBLESHOOTING

6 Wrap a layer of surgical tape around the side of the second CLNW frame to prevent unnecessary harm to the animal. Place the second CLNW frame on top of the other (Figure 4) with the skin in-between. Cut away tape obstructing the titanium ring opening. Secure this CLNW with two additional nuts, this time only loosely tightening (Figure 2d). CAUTION: Do not over tighten these nuts as this will impede blood flow to the inguinal region and subiliac lymph node. Check the range of motion of the limb so that the animal can move its limb. The position of these nuts will be secured in step 9.

7 Remove the suture placed in the dorsal CLNW in step 4 (Figure 2b, white arrowhead). Place two or three sutures through each of the holes on the ventral CLNW. Together with the CLNW, these sutures will keep the tissue in place for fourteen days. Placing the sutures through one but not both CLNW frames makes it harder for the animal to remove the sutures. Placing these sutures through only the ventral CLNW frame specifically allows for microscopy using water immersion objectives so that the water will remain in place.

8 Place the mouse under the surgical bright-field microscope. Use microdissection scissors to open one layer of ventral skin approximately 6mm in diameter (Figure 2e). If significant bleeding occurs from the cutaneous blood vessels, use cautery to stop the bleeding. Usually, the lymph node will be visible after opening the dermis. Any overlying subcutaneous fat can be removed using curved blunt 5.0 forceps. CRITICAL STEP If the lymph node is not directly visible, carefully explore the mammary fat pad using blunt dissection. Do not use cautery in the vicinity of the lymph node nor use forceps directly on the lymph node, as this will inflict irreversible damage.
See TROUBLESHOOTING

9 Apply sterile saline to the wound area to prevent tissue dehydration. Place a glass cover slip in the CLNW groove, covering and protecting the lymph node, and secure the cover slip using a tension C-ring (Figure 2f). Use glue to secure the nuts applied loosely to the screws in step 6 to prevent CLNW detachment.

Post-operative. TIMING 5 minutes.
10 Inject 10ml/kg body weight buprenorphine hydrochloride s.c. once postoperatively before the animal wakes up. Repeat if necessary at any point during daily post-operative follow-up if animal is showing signs of pain or distress, up to twice daily, in line with all relevant guidelines and regulations of the governing IACUC. Monitor daily to make sure the animal is fully ambulatory, with the CLNW in place and no signs of edema caused by the CLNW. Wait two days before administering anesthesia for imaging or other experimental procedures.
See TROUBLESHOOTING

Imaging. TIMING 15-90 minutes (beginning 48 hours or more after CLNW implantation)
11 For all imaging procedures, check whether the imaging setup is correctly working. Then, anesthetize the mouse using a 100/10mg ketamine/xylazine mixture per kg body weight or isoflurane.

12 Position the mouse on an imaging stage (Figures 5 and 6). For fluorescence based angiography, inject 2,000,000 MW Tetramethylrhodamine-dextran (or similar) intravenously.
See TROUBLESHOOTING

13 For multi-photon imaging, there are many commercially available upright microscopes. We use a custom-built multiphoton laser-scanning microscope (adapted from Olympus 300; Optical Analysis Corp.) and a broadband femtosecond laser source (High Performance MaiTai, Spectra-Physics) as described previously [25][13] . Before imaging, we set the laser to ~60mW on sample laser power at 820nm wavelength for Tetramethylrhodamine detection.

14 Use the slowest acquisition to get best quality images and do not digitally alter gain or offset. Perform XYZ or XYZT (for video) imaging, with z (depth) ~20-100 µm. Images from Figure 3 were obtained using Olympus FluoView software with a 25x 1.05NA water-immersion objective at 1x zoom, stack z ~50 µm, 512x512 pixels, 16-bit. For signal detection, use a 610DF75 emission filter for Tetramethylrhodamine (blood vessels), a 535DF43 filter for green (GFP cancer cells), and a 450DF100 filter for SHG imaging in front of the photomultiplier tubes. We use a motorized stage (H101, Prior Scientific, Inc.) to obtain mosaic images combined with customized automation software (LabView, National Instruments). Settings were similar for the Supplementary Videos; small differences are listed in their respective legends. ImageJ (NIH), or similar image analysis software, can be used to combine data acquired from different photomultiplier tubes.

Timing:
Preparation (Procedure step 1), 5-60 minutes
Pre-operative (Procedure steps 2-3), 10 minutes
Surgery (Procedure steps 4-9), 15 minutes
Post-operative (Procedure step 10), 5 minutes
Imaging (Procedure steps11-14), 15-90 minutes

Troubleshooting:

Step	Problem	Possible reason	Possible solution
5	Skin around screw too loose, causing the CLNW to change location over time.	Hole in skin too large	Try using a scalpel instead of using scissors. Make an incision smaller than the screw width. Gently stretch the skin over the screw to get a perfect fit.
8	Surgical damage to lymph node	Trauma by surgical tools	We suggest starting blunt dissection of subcutaneous fat at a side of the lymph node where there is no major blood vessel visible, to prevent bleeding. Gently pull this fat aside to

			find the correct tissue layer. Then, gently pull the fat away covering the lymph node. Do not place your Dumont forceps directly on top of the lymph node to prevent pinching and damaging the lymph node. This will allow for safer removal of the subcutaneous fat located on the top (ventral) of the lymph node.
10	Lymph node position changes over time	Sutures are lost	Animals should be monitored daily postoperatively and if any sutures are lost, the sutures should be replaced to keep the lymph node in place.
IMAGING	Z drift during imaging when using a water immersion objective	Water evaporating from in between cover slip and objective	Water can be carefully added in between z-stack acquisition if z drift is bothersome. Alternatively, acquire a larger z stack to later adjust for the drift using image analysis software, or change the imaging modality to one not dependent on water immersion objectives.

Anticipated results

The first 14 days after surgery, clear, high-quality images are expected using the CLNW. The CLNW will also prevent movement artifacts during imaging and will not impede blood and lymph flow if implanted properly. For this purpose, the surface of the glass coverslip can be easily cleaned with ethanol before imaging or the coverslip can be removed and replaced. As noted earlier, minimal morphological, cellular and biochemical changes are expected (see Supplementary Figure 4, and Supplementary Figure 1d in Jeong H. *et al*. [1]) and the CLNW does not need successive surgeries to expose the imaging window.

Examples of imaging results after CLNW implantation are shown in Figure 3. The lymph node and surrounding vasculature can be imaged by optical coherence tomography (Figure 3a). Metastatic Dendra2-expressing 4T1 breast cancer (green) in the inguinal lymph node (Figure 3b, 3c) can be monitored longitudinally. Blood vessels were used to repeatedly find the region of interest in the lymph node, allowing the imaging to be centered on the growing metastatic lesion. Blood vessels can be identified by intravenous injection of fluorescently labeled dextran.

To generate metastatic lymph nodes, squamous cell carcinomas or melanomas can be injected in the thigh subcutis or breast tumor cells can be injected in the 4th mammary fat pad of the mouse, which subsequently metastasize to the inguinal lymph node. Lymphangiography can be used to confirm whether tumors drain to the inguinal lymph node [1, 26]. At early stages of lymph node metastasis—approximately 7 days post-tumor implantation of the 4T1 breast cancer cell line—tumor cells can be visualized in the subcapsular sinus of the lymph node. At later time points, these cells invade the parenchyma, moving toward blood vessels [1]. The timing of CLNW implantation

can be tailored to the research question and the metastatic behavior of the tumor cell line. Tumor chunk implantation of the primary tumor can be considered to avoid direct spread of tumor cells into the inguinal lymph node from the initial injection. To study immune cell behavior in metastatic lymph nodes, fluorescently labeled immune cells can be adoptively transferred to a tumor-bearing mouse and subsequently imaged in the tumor-draining lymph node using the CLNW.

In addition to monitoring the progression of tumor growth in the lymph node over days, it is possible to perform short-term time-lapse intravital imaging using the CLNW to analyze tumor cell interaction with immune cells and other lymph node stromal cells as has also been accomplished using prior models [3, 7, 8]. Supplementary Video 1 shows a maximum intensity project of a three-dimensional lymph node tissue acquired by time-lapse multiphoton microscopy in LysM-GFP transgenic mice. Lymph node neutrophil and monocyte movement (green) in blood vessels (red) and lymph node tissue can be observed. In Supplementary Video 2, time-lapse microscopy was performed at a higher resolution for a high-endothelial vessel in the lymph node that shows GFP positive cells flowing, rolling and extravasating.

Author contributions

E.F.J.M and H-S.J. developed the protocol. E.F.J.M. and T.P.P. wrote the manuscript. E.F.J.M. and E.R.P. performed the experiments, including supplementary video acquisition. C.B. and B.J.V. performed intravital imaging and processing of optical coherence tomography. E.F.J.M., E.R.P. and C.B. prepared in-text figures and supplementary videos. T.A.R. designed, developed and prepared the schematics presented in the supplement. T.P.P. supervised all authors in this project. All authors contributed intellectually to and reviewed the manuscript.

Acknowledgements

This work was supported by the National Institutes of Health under award numbers R00CA137167 (T.P.P.), DP2OD008780 (T.P.P.), R01CA163528 (B.J.V.), and R01HL128168 (T.P.P.). Research reported in this publication was supported in part by the Center for Biomedical OCT Research and Translation through Grant Number P41EB015903 (B.J.V.), awarded by the National Institute of Biomedical Imaging and Bioengineering of the National Institutes of Health. The National Cancer Institute Federal Share of Proton Income CA059267 (T.P.P., B.J.V.) and the Massachusetts General Hospital Executive Committee on Research ISF (T.P.P.) also supported this work. We would like to thank Julia Kahn, Elizabeth Beech and Cheryl Cui for outstanding technical support.

Financial interests

The authors declare that they have no competing financial interests.

References

1. Jeong, H.S., et al., Investigation of the Lack of Angiogenesis in the Formation of Lymph Node Metastases. J Natl Cancer Inst, 2015. 107(9).
2. Van den Broeck, W., A. Derore, and P. Simoens, Anatomy and nomenclature of murine lymph nodes: Descriptive study and nomenclatory standardization in BALB/cAnNCrl mice. J Immunol Methods, 2006. 312(1-2): p. 12-9.
3. von Andrian, U.H., Intravital microscopy of the peripheral lymph node microcirculation in mice. Microcirculation, 1996. 3(3): p. 287-300.

4. Miller, M.J., et al., Two-photon imaging of lymphocyte motility and antigen response in intact lymph node. Science, 2002. 296(5574): p. 1869-73.
5. Stoll, S., et al., Dynamic imaging of T cell-dendritic cell interactions in lymph nodes. Science, 2002. 296(5574): p. 1873-6.
6. Mora, J.R., et al., Selective imprinting of gut-homing T cells by Peyer's patch dendritic cells. Nature, 2003. 424(6944): p. 88-93.
7. Mempel, T.R., S.E. Henrickson, and U.H. Von Andrian, T-cell priming by dendritic cells in lymph nodes occurs in three distinct phases. Nature, 2004. 427(6970): p. 154-9.
8. Schramm, R., et al., The cervical lymph node preparation: a novel approach to study lymphocyte homing by intravital microscopy. Inflamm Res, 2006. 55(4): p. 160-7.
9. Ito, K., et al., Unexpected dissemination patterns in lymphoma progression revealed by serial imaging within a murine lymph node. Cancer Res, 2012. 72(23): p. 6111-8.
10. Jafarnejad, M., et al., Modeling Lymph Flow and Fluid Exchange with Blood Vessels in Lymph Nodes. Lymphat Res Biol, 2015. 13(4): p. 234-47.
11. Gonzalez, S.F., et al., The role of innate immunity in B cell acquisition of antigen within LNs. Adv Immunol, 2010. 106: p. 1-19.
12. Brown, E., et al., In vivo imaging of tumors. Cold Spring Harb Protoc, 2010. 2010(7): p. pdb.prot5452.
13. Padera, T.P., et al., Conventional and high-speed intravital multiphoton laser scanning microscopy of microvasculature, lymphatics, and leukocyte-endothelial interactions. Mol Imaging, 2002. 1(1): p. 9-15.
14. Vakoc, B.J., et al., Three-dimensional microscopy of the tumor microenvironment in vivo using optical frequency domain imaging. Nat Med, 2009. 15(10): p. 1219-23.
15. Luo, W., et al., Optical biopsy of lymph node morphology using optical coherence tomography. Technol Cancer Res Treat, 2005. 4(5): p. 539-48.
16. Nolan, R.M., et al., Intraoperative optical coherence tomography for assessing human lymph nodes for metastatic cancer. BMC Cancer, 2016. 16: p. 144.
17. Kedrin, D., et al., Intravital imaging of metastatic behavior through a mammary imaging window. Nat Methods, 2008. 5(12): p. 1019-21.
18. Shan, S., B. Sorg, and M.W. Dewhirst, A novel rodent mammary window of orthotopic breast cancer for intravital microscopy. Microvasc Res, 2003. 65(2): p. 109-17.
19. Leunig, M., et al., Angiogenesis, microvascular architecture, microhemodynamics, and interstitial fluid pressure during early growth of human adenocarcinoma LS174T in SCID mice. Cancer Res, 1992. 52(23): p. 6553-60.
20. Endrich, B., et al., Technical report--a new chamber technique for microvascular studies in unanesthetized hamsters. Res Exp Med (Berl), 1980. 177(2): p. 125-34.
21. Yuan, F., et al., Vascular permeability and microcirculation of gliomas and mammary carcinomas transplanted in rat and mouse cranial windows. Cancer Res, 1994. 54(17): p. 4564-8.
22. Farrar, M.J., et al., Chronic in vivo imaging in the mouse spinal cord using an implanted chamber. Nat Methods, 2012. 9(3): p. 297-302.
23. Brodnick, S.K., et al., A chronic window imaging device for the investigation of in vivo peripheral nerves. Conf Proc IEEE Eng Med Biol Soc, 2014. 2014: p. 1985-8.
24. Ritsma, L., et al., Surgical implantation of an abdominal imaging window for intravital microscopy. Nat Protoc, 2013. 8(3): p. 583-94.

25. Brown, E.B., et al., In vivo measurement of gene expression, angiogenesis and physiological function in tumors using multiphoton laser scanning microscopy. Nat Med, 2001. 7(7): p. 864-8.
26. Hoshida, T., et al., Imaging steps of lymphatic metastasis reveals that vascular endothelial growth factor-C increases metastasis by increasing delivery of cancer cells to lymph nodes: therapeutic implications. Cancer Res, 2006. 66(16): p. 8065-75.

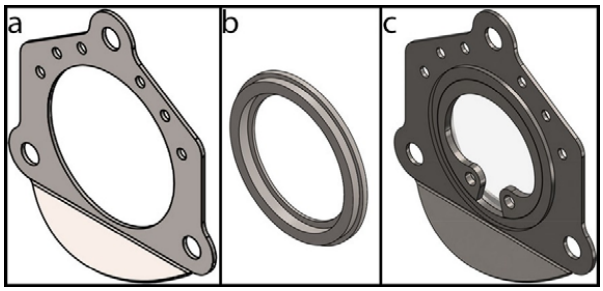

Figure 1. CLNW parts and assembly. A) Titanium frame. B) Titanium ring designed to fit perfectly into the center of the titanium frame. C) The complete CLNW, including the titanium frame, ring, and the tension C-ring insert. CAD schematics for each individual part is available in the supplement (Supplementary Figure 1-3).

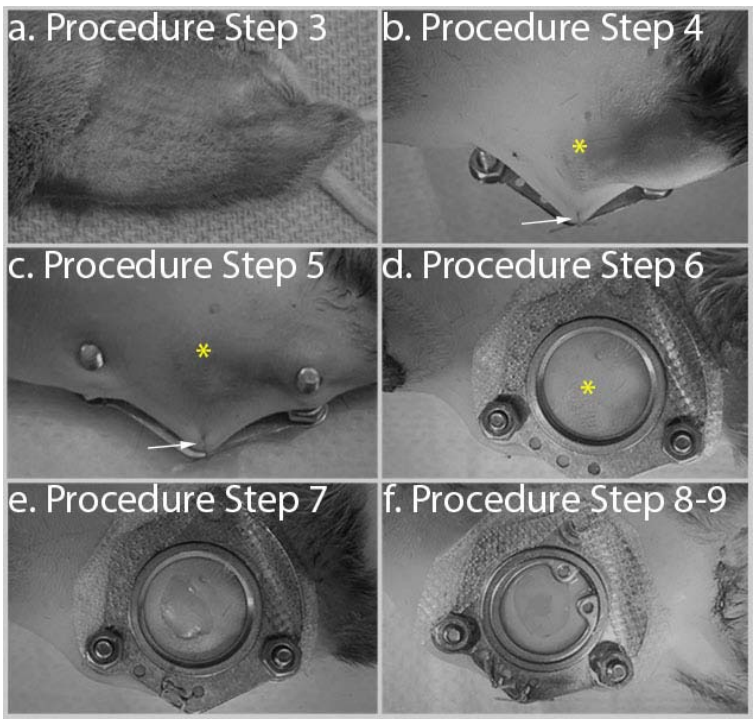

Figure 2. Surgical procedure. A) Shave the mouse between regio femoris, regio hypochondriaca, and both ventral and dorsal midline (Procedure step 3). B) Pull a suture (white arrowhead) through the left-most of the smaller holes of the CLNW and place the suture above the subiliac lymph node (asterisk)(Procedure step 4). C) Pierce the skin directly above the screws using a scalpel or scissors and place the screw through the hole (Procedure step 5). D) Place the second CLNW on top of the other and secure with two nuts (Procedure step 6). E) Remove the suture placed previously and place sutures through the holes on the ventral CLNW (Procedure step 7), then open the skin. F) Expose the lymph node using blunt dissection of perinodal fat (Procedure step 8), position the glass cover slip and secure with the tension C-ring. Lastly, use a small drop of glue to secure each nut (Procedure step 9). The yellow asterisk in B-D shows the position of the lymph node. These experiments were approved by the IACUC at MGH.

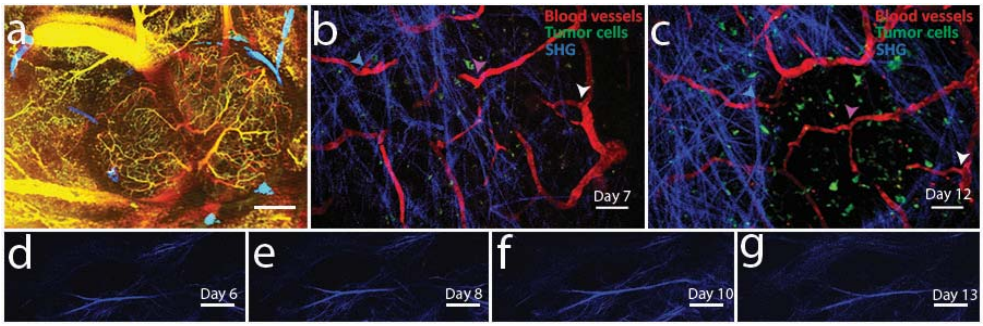

Figure 3. Lymph node imaging using CLNW. A) Optical coherence tomography image of entire lymph node and surrounding vasculature two days post CLNW implantation. Gradient yellow (superficial) to red is blood vessel depth; blue are lymphatic vessels. Scale bar 500 µm. B, C) Lymph node MPM images acquired 7 and 12 days post CLNW implantation, monitoring the growth of cancer cells in a tumor draining lymph node. Arrows indicate identical blood vessel locations, while the tumor area remains centered in the imaging region of interest. The blood is labeled with tetramethylrhodamine-dextran (red). The 4T1 tumor cells express Dendra2 (green) and collagen (blue) is visualized by SHG. D–G) Lymph node harboring metastasized 4T1 tumor cells. At day 4 after tumor cell injection in the mammary fatpad the CLNW was implanted. SHG imaging of the changes in fibrillary collagen in a single location over time at day 6, 8, 10 and 13 by MPM is shown in D-G, respectively. Scale bar B-G 50 µm. Images obtained with a 25x 1.05NA water-immersion objective at 1x zoom, 512x512 pixels, 16-bit. These experiments were approved by the IACUC at MGH.

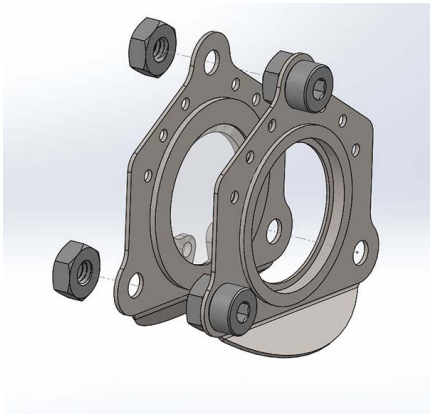

Figure 4. Combining CLNW frames. Representation of how two CLNW frames connect. The ventral CLNW frame has both tension C-ring and cover slip inserted.

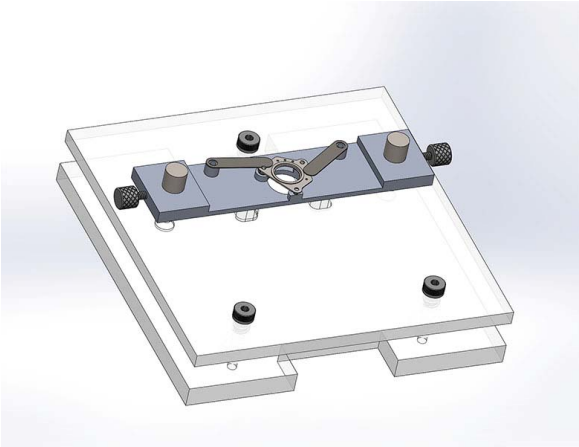

Figure 5. CLNW imaging stage assembled. The CLNW imaging stage consists of an acrylic base, with springs made from spring steel which can be adjusted. The CLNW screws are positioned into the predrilled holes in the imaging plate, preventing movement during imaging. The CLNW is gently secured with two spring clamps. Supplementary Figures 5-10 show the schematics for the separate parts.

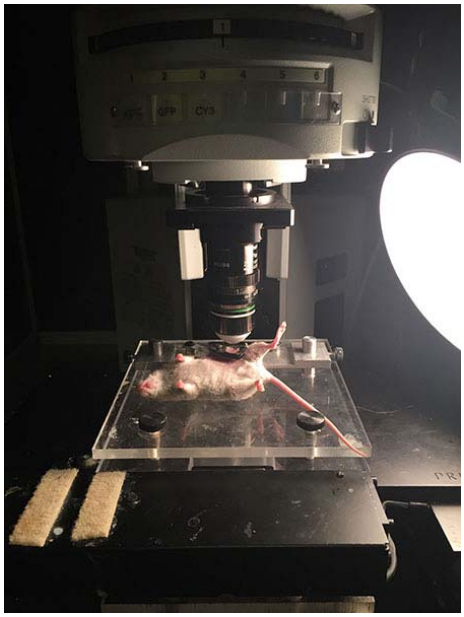

Figure 6. Imaging setup. For demonstration purposes, the objective is slightly elevated and water is not added in between cover slip and objective. The tape wrapped around the side of the ventral titanium window and heating pad below the mouse are removed to be able to clearly show how the CLNW is mounted. This experiment was approved by the IACUC at MGH.

3. Measuring Vascular Permeability In Vivo

Eelco F.J. Meijer, James W. Baish*, Timothy P. Padera, and Dai Fukumura

Edwin L. Steele Laboratories, Department of Radiation Oncology, Massachusetts General Hospital, Harvard Medical School, Boston, MA 02114. *Current affiliation: Departments of Mechanical and Biomedical Engineering, Bucknell University, Lewisburg, PA 17837.

Book chapter in: Methods in Molecular Biology, 2016. 1458: p. 71-85.

Abstract

Over the past decades, in vivo vascular permeability measurements have provided significant insight into vascular functions in physiological and pathophysiological conditions such as the response to pro- and anti-angiogenic signaling, abnormality of tumor vasculature and its normalization, and delivery and efficacy of therapeutic agents. Different approaches for vascular permeability measurements have been established. Here, we describe and discuss a conventional *2D* imaging method to measure vascular permeability, which was originally documented by Gerlowski and Jain in 1986 (Microvasc Res 31:288–305, 1986) and further developed by Yuan et al. in the early 1990s (Microvasc Res 45:269–289, 1993; Cancer Res 54:352–3356, 1994), and our recently developed *3D* imaging method, which advances the approach originally described by Brown et al. in 2001 (Nat Med 7:864–868, 2001).

1. Introduction

Measurements of transvascular transport have been proven invaluable in studying numerous *in vivo* processes and their regulation, including pro- and anti-angiogenic signaling, as well as vascular abnormalities and their putative normalization in disease states like cancer and inflammation [1]. It has been shown that abnormal tumor vasculature can be remodeled towards more normal phenotype ("normalization") by restoring proper balance of pro- and anti-angiogenic signaling improving its function [2] and delivery of therapeutics [3]. There are 2 different types of transport for molecules to extravagate across blood vessel wall – convection and diffusion [1]. Convection is an active transport defined by a driving force–pressure gradient and a resistance–hydraulic conductivity: $\mathbf{Convection} = \boldsymbol{Lp\ S}\ [(\boldsymbol{Pv} - \boldsymbol{Pi}) - \boldsymbol{s}\ (\boldsymbol{pv} - \boldsymbol{pi})]$; where L_p = hydraulic conductivity of vessel (cm^4/sec-mmHg), S = surface area per unit volume (cm^2/cm^3), P_v, P_i = vascular and interstitial pressures, s = osmotic reflection coefficient, p_v, p_i = vascular & interstitial osmotic pressures (mmHg). On the other hand, diffusion is a passive transport defined by concentration gradients and permeability: $\mathbf{Diffusion} = \boldsymbol{PS}\ (\boldsymbol{Cv} - \boldsymbol{Ci})$; where P = vascular permeability (cm/sec), S = surface area per unit volume (cm^2/cm^3), C_v, C_i = concentrations in vascular & interstitial space (mole/cm^3). Tumor vessels are leaky which elevates tumor interstitial fluid pressure. While the extravagated fluid can escape (ooze out) from tumor periphery, it builds up inside the tumor mass. Therefore, the pressure gradient across a vessel wall is diminished in tumors making convective transport less important and diffusion the dominant transport mechanism in solid tumors [4]. In this chapter we discuss tumor transvascular transport measurements, which is referred to as the effective permeability. It includes the dominant diffusive component (intrinsic permeability) as well as the less important convective component [1]. Effective permeability is a principal parameter to understand functionality of blood vessels and especially in tumors, one of the most important parameters [1, 2].

Early methods for estimating vascular permeability using *2D*-imaging data were formulated by Gerlowski and Jain in 1986 [5] and further developed in the early 1990's by Yuan *et al*. [6, 7]. This approach relies on the estimates derived from temporal alteration in total fluorescence intensity as well as vascular morphologies obtained from superficial aspects of tissue using intravital fluorescence microscopy. Around a decade later, a *3D* approach was developed by Brown *et al*. [8] using multiphoton microscopy [9]. This advanced optical technique allows determining fluorescence intensity gradients surrounding *individual* vessels to calculate local permeability with high spatial resolution.

Both the *2D*- and *3D*-vascular permeability measurement methods are based on the same general principles. If pressure-driven transport can be neglected in a region of interest (ROI), as often the case in disease states such as tumors, the apparent vascular permeability P may be calculated from $P = J/S\Delta C$ where J is the rate at which a solute material is transported across a membrane of area S due to the concentration difference across the membrane ΔC. The most common approaches to measuring J, S and ΔC involve three related, but distinct steps. The first is establishment of a known concentration difference between the inside and outside of one or more blood vessels (ΔC). Image-based methods are used to observe the concentrations inside and outside of the vessel wall where the concentration is taken to be proportional to the observed fluorescence level. Right after injecting fluorescent material, the concentration outside the vessel wall should be zero. Secondly, the surface area of the blood vessel must be estimated (S). Estimates of the surface area are derived from the analysis of the vascular architecture in the image. If the vessel can be assumed to be

cylindrical, the surface can be estimated from the length and diameter of the vessel. Alternatively, a pixel or voxel counting technique can be employed to estimate the surface area if the vascular architecture is identified in *3D*. Thirdly, the transport rate is determined from changes in the fluorescence intensity of the tissue over time. Typically, the intravascular and extravascular spaces are taken to be different control volumes separated by the membrane. If we assume that all of the fluorescent material leaving the blood vessel through the vessel wall can be observed in extravascular space of the ROI we can represent flux as $J = \frac{d}{dt}\int_{V_{ex}} C_{ex} dV$. However, for this equation to be strictly valid the boundary of the ROI must not offer an alternative route in or out. Such conditions might be well approximated if the blood vessels are relatively distant from the ROI boundary, or the boundary is sufficiently typical of adjacent ROI's that material loss at the boundary is balanced by material gain. Accurately determining the flux has proven the biggest challenge.

The *2D* approach from Yuan *et al*. has proven valuable for measuring vascular permeability using the principles described above (see **Table 1** for examples of *2D*-permeability measurements). This technique however has several limitations because of its many assumptions. Because this method is in *2D*, the surface area-to-volume ratio of vessels collected from a single defocused plane on the surface is used to approximate the ratio of vessels in the entire ROI that is being imaged. Also, in a fluorescence image the vessel diameter will appear larger than its true value because of light scattering, which needs to be corrected for. The actual *in vivo* tissue depth of the ROI being measured may also vary per tissue and tumor, depending on cellular content and fluorescent material used. In addition, the vessels are assumed to be of cylindrical shape to be able to estimate the surface area of the blood vessels. Lastly, any fluorescent material leaking out from tissue surrounding the ROI and residing on top of the tissue will incorrectly increase calculated vascular permeability value, leading to measurement error in some samples.

The *3D* method using multiphoton microscopy —which can achieve greater imaging depths when compared to single photon intravital imaging techniques —described in Brown *et al*. addressed many of the issues described above, but has some disadvantages on its own (see **Table 1** for examples of *3D*-permeability measurements). This method requires an accurate vessel mask and the quality of the multiphoton microscopy images dominates how accurate the vessel masking is at greater tissue depths. However, the actual tissue depth where light is collected is known using this method and the surface area-to-volume ratio is more realistic than the *2D* method. In addition, light scattering adjustments as well as hematocrit value and cylindrical vessel shape assumptions are not needed. Fluorescent material residing on top of the tissue can also be selectively avoided. The formula used by Brown *et al.* calculates vascular permeability (*P*) in cm/s as $\boldsymbol{P = \lim_{t\to 0} \frac{\delta}{\delta t} \frac{\int_{r=R}^{\infty} F(r) r dr}{(Fv - Fi) R}}$. This formula however is not strictly correct except under fairly restrictive conditions that may not be generally met. Correct use of this method requires that a roughly cylindrical region exists around a vessel that is influenced only by the vessel of interest during the time that is used for permeability calculation. *In vivo* however, this cylindrical region is generally not present because the ROI may include multiple -tortuous- vessels in close vicinity. Vessels may also be present near the edges of the ROI. Altogether, this *3D* method yields a more realistic measurement of vascular permeability.

A recommended alternative approach would be to use a box-shaped ROI, using $\boldsymbol{P = \frac{\frac{\delta}{\delta t}\int_{Vext} F(\vec{r})dV}{S(Fv-Fi)}}$ as used in Kesler *et al.* [10]. In this approach the voxels are segmented into three categories, namely those inside the vessel, those on the vessel wall and those outside the vessel. For calculating vascular permeability, all vessels are mathematically considered as a single vessel. A downside of this approach is that permeability differences among single vessels cannot be estimated. However, the mean over all vessels should be very well estimated if the vessel masking is adequate. The experimental setup of the *2D* method developed by Yuan *et al*. and our recommended alternative *3D* approach to measure vascular permeability *in vivo* are discussed in detail below.

2. Materials

General materials: heating pad or similar device; Ketamine/Xylazine mixture 90 mg/9 mg per Kg body weight.; fluorescent molecules; $30^{1/2}$ gauge needles; PE10 Polyethylene Tubing; ½ cc U-100 $28^{1/2}$ gauge Insulin Syringes.

Microscope setup measuring vascular permeability in mice using *2D* method

The tracer molecules used in this method are 100 µl per 25 g body weight 1% 2,000,000 mol wt FITC-dextran and 1% tetramethylrhodamine-bovine serum albumin (BSA). A fluorescence intravital microscope (see **Fig 1)** is used with a long working distance 20X 0.40 NA objective and a fluorescence filter set suitable for FITC and Rhodamine, connected to an intensified CCD (charge-coupled device) video camera and photomultiplier tube. A computer is used to capture the output. The microcirculation is epi-illuminated by a 100-W mercury lamp. A 50% neutral density filter and a heat absorption filter were put in the epi-illumination pathway to prevent overheating of tissue.

Microscope setup measuring vascular permeability in mice using 3D method

The tracer molecule used in this method is 100 µl per 25 g body weight 1% FITC-BSA. The multiphoton microscope (see **Fig 1)** *consists of a mode-locked Ti:sapphire laser and an x-y laser scanner purchased as described previously [8].* A Pockels cell is used to allow for rapid modulation of laser intensity. *The system also requires non-descanned photomultiplier tubes (PMT), a dichroic beam splitter, a digital image and analysis station and a computer with image acquisition software. We use a 20X 0.95 NA or* 25X 1.05 NA water-immersion objective (Olympus) and a 525DF100 filter (Chroma) suitable for FITC.

3. Methods

3.1. Measuring vascular permeability in mice using 2D method

General comment: make sure the microscope is in complete darkness when imaging.

1. Anaesthetize the mouse with a Ketamine/Xylazine mixture 90mg/9mg per Kg body weight. Maintain the animal's core body temperature using a heating pad or similar device.

2. Insert a $30^{1/2}$ gauge needle into a tail vein, connected to PE10 Polyethylene Tubing and a ½ cc U-100 $28^{1/2}$ gauge Insulin Syringe filled with 100 µl per 25 g body weight 1% 2,000,000 mol wt FITC-dextran. Also prepare an Insulin Syringe filled with 100 µl per 25g body weight 1% tetramethylrhodamine-BSA.

3. Inject the FITC-dextran. Flush the Polyethylene Tubing with a small amount of physiologic saline for intravenous infusion and leave the needle in the tail vein (*see* **Note 1**).

4. Place the mouse and the area to be studied under the intravital fluorescence microscope, equipped with the fluorescence filter set for Rhodamine and FITC and a 100-W Mercury Lamp (*see* **Note 2**).

5. Acquire an image of the vessels in the area to be studied using the CCD camera. Do this by using the fluorescence filter for FITC (*see* **Note 3**).

6. Set the fluorescence filter to Rhodamine. Use the photomultiplier tube to acquire background signal for several seconds and make sure the system is fully operational.

7. Attach the Insulin Syringe containing tetramethylrhodamine-BSA. Start measuring the tissue fluorescence using the PMT and subsequently inject the tetramethylrhodamine-BSA. Flush the Polyethylene Tubing with a small amount of physiologic saline for intravenous infusion. Do not exceed 10 seconds of measuring to avoid photodamage of the tissue and photobleaching of the fluorescent molecules (*see* **Note 4**).

8. Repeat 10 seconds of signal acquisition every 2 minutes for up to 20 minutes.

9. After the last signal acquisition, acquire a second image of the vessels in the area studied using the fluorescence filter for FITC and the CCD camera. Compare with the image taken at *step 5* and confirm the tissue had no x, y or z shift.

10. Using the images and measurements gathered, vascular permeability (*P*) can be calculated in cm/s as $P = (1 - HT)\, V/S(1/(I_0 - I_b) \cdot dI/dt + 1/K))$, where *HT* is tissue hematocrit estimated to be 0.19 in tumors [7, 11] and 0.46 in the systemic circulation [12], *I* is the average fluorescence intensity of the whole image, I_0 is the value of *I* immediately after the filling of all vessels by fluorescent tracer, I_b is the background fluorescence intensity, and K is the time constant of plasma clearance estimated to be $9.1*10^3$ seconds for BSA [7]. The slope of the measurements plotted over time should be normalized, where *dI/dt* becomes $(dI/dt)/(I_0\text{-}I_b)$. *V* and *S* are the total volume and surface area of vessels within the tissue volume covered by the surface image, respectively. The volume to surface ratio is calculated as $\frac{V}{S} = \sum_{n=1}^{M} L_n d_n^2 / \sum_{n=1}^{M} 4 d_n L_n$ where d_n is diameter of the n^{th} vessel and L_n is length of the n^{th} vessel corrected by a factor of 0.79 for light scattering in the tissue [7]. These vessel diameters and lengths can be manually calculated from the acquired image of the vessels in the area to be studied after injecting FITC-dextran (*see* **Note 5**).

3.2. Measuring vascular permeability in mice using *3D* method

General comment: make sure the microscope is in complete darkness when imaging.

1. Make sure your multiphoton setup is working correctly before you anaesthetize your mouse. Use fluorescence filters adequate for the material you will be using, in this case FITC-BSA. We use a 525DF100 filter. Set Ti-Sapphire laser wavelength to 780 nm. Set laser power to 130-mW.

2. Anaesthetize the mouse with a Ketamine/Xylazine mixture 90 mg/9 mg per Kg body weight. Maintain the animal's core body temperature using a heating pad or similar device.

3. Insert a $30^{1/2}$ gauge needle into a tail vein, connected to PE10 Polyethylene Tubing and a ½ cc U-100 $28^{1/2}$ gauge Insulin Syringe filled with 100 µl per 25 g body weight 1% FITC-BSA.

4. Place the mouse and the area to be studied under the multiphoton microscope objective. We use a 20X 0.95 NA or 25x 1.05 NA water-immersion objective. Set the focus on the most superficial vasculature you can find in the area of interest and make sure the water between tissue and objective is not leaking.

5. Inject the FITC-BSA. Flush the Polyethylene Tubing with a small amount of physiologic saline for intravenous infusion (*see* **Note 6**).

6. Start imaging 30 seconds after injecting FITC-bsa. Arteries show fluorescence within seconds after injection, veins can take somewhat longer. We use slowest acquisition to get best quality images, 256 x 256 voxels, 74 z slices and steps of 1.84 µm obtained with a 25X water-immersion objective. For a 20X objective, use z steps of 2.76 µm (*see* **Note 7**).

7. Acquire z stacks for up to 20 minutes (*see* **Note 8**).

8. For image analysis, we recommend a box-shaped ROI approach containing multiple vessels. Use software to segment voxels into three categories: those inside the vessel, those on the vessel wall and those outside the vessel (see **Fig 2)**. Calculate vascular permeability (*P*) as $P = \frac{(voxel\ size)*Slope\ of\ Fe\ over\ time}{(n_{wall})*Mean\ of\ (Fv-Fi)}$ where n_{wall} is the number of voxels making up the vessel walls, *Fe* is total fluorescence from all exterior points including those on the wall, *Fv* mean fluorescence from the interior voxels and *Fi* the mean fluorescence from the vessel wall voxels (*see* **Note 9**).

4. Notes

1. Insulin syringes are precise and have little syringe dead space.

2. We prefer using a chronic window to keep the area to be studied in place and allow for chronic imaging without serial laparotomies and breathing artifacts [13].

3. Take an image with maximum gain that the camera can handle without damaging it or before switching off. Do not adjust offset or other settings; you can do this later with image processing software.

4. Leave the needle in the tail vein attached to the tubing and syringe to prevent blood loss.

5. Use a graticule slide to know the actual size of the area and vessels you are measuring. Use µm for *V/S* and *K* in seconds.

6. Make sure the area you are imaging is clean. If you are using imaging windows with a coverslip, replace the glass coverslip before imaging if needed. If there is water leakage, check if the coverslip

is intact and well secured or replace the coverslip. Also, be particularly careful to prevent collision between your objective and anything that can damage it.

7. Do not adjust the gain, offset, etc. Similar modifications can be done after imaging with offline processing, while keeping the best quality raw data. We would recommend gathering more z slices than you need to be able to correct for any z shift you might experience over time. Moreover, check your data for pixel saturation. If you are seeing saturation in the fluorescence intensity in your data lower the photomultiplier tube power or alternatively lower laser power, your data will be incorrect and hence (partly) useless otherwise.

8. Stay alert for xy shifts during imaging, you can manually adjust these in between data acquisition or use offline processing to correct for this later. If you are seeing intensity loss of the vessels in the field of view, make sure there is enough water between the tissue and the objective. We recommend leaving a syringe with water in the vicinity of your objective.

9. We use ImageJ (1.47v, *NIH*) for vessel masking and MATLAB (R2015b, *MathWorks*) for further data analysis. Use earliest data stacks acquired for vessel masking to obtain most accurate mask. Data stacks are converted to binary (ImageJ > Process > Binary > Make Binary > Method "Li") and a median filter (Process > Filter > Median > Radius 1 pixel) is subsequently used to remove noise and smoothen blood vessel lumen but not the vessel wall. The *MATLAB* script is not added here due to page limitations but is available upon request.

5. Discussion

If it is executed properly, our recommended *3D* approach should yield more accurate and reliable *in vivo* vascular permeability measurements than the other methods discussed. The *3D* permeability measurements however rely heavily on an accurate vessel masking and while our vessel masking is fairly accurate in a range of tissues with high signal-to-noise ratio and low auto-fluorescence, images obtained with lower signal-to-noise ratio. If there is high auto-fluorescence a different approach may be more practically robust. Comparison between permeability measurements obtained with the same method can be safely made. However, the comparison of permeability measurements between different methods should be made with caution. There should be a common denominator such as the measurements performed in the same tumor model with the same condition (i.e., size, control treatment etc.) in order to interpret the data properly. As discussed above, the difference in surface area-to-volume ratio estimation of multiple vessels in a similar ROI between the *2D*- and *3D*-methods will tend to result in lower calculated permeability values in the *2D*-method as compared to that in the *3D*-method. Hence for comparison, the *3D* measurements raw data should be converted to *2D* data before the analysis. Finally, examples of vascular permeability measurements from the E.L. Steele laboratories using *2D*- and *3D*-methods described by Yuan *et al.* and Brown *et al.,* respectively, are summarized in **Table 1**.

Acknowledgement

We would like to thank Echoe Bouta, Cheryl Cui, Nir Maimon, Lance L. Munn and Rakesh K. Jain from the E.L. Steele Laboratories and Cedric Blatter and Benjamin Vakoc from the Wellman Center for Photomedicine (Massachusetts General Hospital, USA) for insightful discussions and intellectual input. We would like to thank Lance L. Munn for his help with illustrations and Cedric Blatter for his tremendous help with vessel masking and MATLAB coding for the *3D* method.

References

1. Jain, R.K., Transport of molecules across tumor vasculature. Cancer Metastasis Rev, 1987. 6(4): p. 559-93.
2. Jain, R.K., L.L. Munn, and D. Fukumura, Dissecting tumour pathophysiology using intravital microscopy. Nat Rev Cancer, 2002. 2(4): p. 266-76.
3. Chauhan, V.P. and R.K. Jain, Strategies for advancing cancer nanomedicine. Nat Mater, 2013. 12(11): p. 958-62.
4. Baxter, L.T. and R.K. Jain, Transport of fluid and macromolecules in tumors. I. Role of interstitial pressure and convection. Microvasc Res, 1989. 37(1): p. 77-104.
5. Gerlowski, L.E. and R.K. Jain, Microvascular permeability of normal and neoplastic tissues. Microvasc Res, 1986. 31(3): p. 288-305.
6. Yuan, F., et al., Microvascular permeability of albumin, vascular surface area, and vascular volume measured in human adenocarcinoma LS174T using dorsal chamber in SCID mice. Microvasc Res, 1993. 45(3): p. 269-89.
7. Yuan, F., et al., Microvascular permeability and interstitial penetration of sterically stabilized (stealth) liposomes in a human tumor xenograft. Cancer Res, 1994. 54(13): p. 3352-6.
8. Brown, E.B., et al., In vivo measurement of gene expression, angiogenesis and physiological function in tumors using multiphoton laser scanning microscopy. Nat Med, 2001. 7(7): p. 864-8.
9. Denk, W., J.H. Strickler, and W.W. Webb, Two-photon laser scanning fluorescence microscopy. Science, 1990. 248(4951): p. 73-6.
10. Kesler, C.T., et al., Angiopoietin-4 increases permeability of blood vessels and promotes lymphatic dilation. Faseb j, 2015. 29(9): p. 3668-77.
11. Brizel, D.M., et al., A comparison of tumor and normal tissue microvascular hematocrits and red cell fluxes in a rat window chamber model. Int J Radiat Oncol Biol Phys, 1993. 25(2): p. 269-76.
12. Schuler, B., et al., Optimal hematocrit for maximal exercise performance in acute and chronic erythropoietin-treated mice. Proceedings of the National Academy of Sciences of the United States of America, 2010. 107(1): p. 419-423.
13. Brown, E., et al., In vivo imaging of tumors. Cold Spring Harb Protoc, 2010. 2010(7): p. pdb.prot5452.
14. Yuan, F., et al., Vascular permeability and microcirculation of gliomas and mammary carcinomas transplanted in rat and mouse cranial windows. Cancer Res, 1994. 54(17): p. 4564-8.
15. Yuan, F., et al., Time-dependent vascular regression and permeability changes in established human tumor xenografts induced by an anti-vascular endothelial growth factor/vascular permeability factor antibody. Proc Natl Acad Sci U S A, 1996. 93(25): p. 14765-70.
16. Winkler, F., et al., Kinetics of vascular normalization by VEGFR2 blockade governs brain tumor response to radiation: role of oxygenation, angiopoietin-1, and matrix metalloproteinases. Cancer Cell, 2004. 6(6): p. 553-63.
17. Xu, L., et al., Placenta growth factor overexpression inhibits tumor growth, angiogenesis, and metastasis by depleting vascular endothelial growth factor homodimers in orthotopic mouse models. Cancer Res, 2006. 66(8): p. 3971-7.

18. Kamoun, W.S., et al., Edema control by cediranib, a vascular endothelial growth factor receptor-targeted kinase inhibitor, prolongs survival despite persistent brain tumor growth in mice. J Clin Oncol, 2009. 27(15): p. 2542-52.
19. Chae, S.S., et al., Angiopoietin-2 interferes with anti-VEGFR2-induced vessel normalization and survival benefit in mice bearing gliomas. Clin Cancer Res, 2010. 16(14): p. 3618-27.
20. Stroh, M., et al., Quantum dots spectrally distinguish multiple species within the tumor milieu in vivo. Nat Med, 2005. 11(6): p. 678-82.
21. Kashiwagi, S., et al., Perivascular nitric oxide gradients normalize tumor vasculature. Nat Med, 2008. 14(3): p. 255-7.
22. Monsky, W.L., et al., Augmentation of transvascular transport of macromolecules and nanoparticles in tumors using vascular endothelial growth factor. Cancer Res, 1999. 59(16): p. 4129-35.
23. Hobbs, S.K., et al., Regulation of transport pathways in tumor vessels: role of tumor type and microenvironment. Proc Natl Acad Sci U S A, 1998. 95(8): p. 4607-12.
24. Izumi, Y., et al., Tumour biology: herceptin acts as an anti-angiogenic cocktail. Nature, 2002. 416(6878): p. 279-80.
25. Monsky, W.L., et al., Role of host microenvironment in angiogenesis and microvascular functions in human breast cancer xenografts: mammary fat pad versus cranial tumors. Clin Cancer Res, 2002. 8(4): p. 1008-13.
26. Fukumura, D., et al., Predominant role of endothelial nitric oxide synthase in vascular endothelial growth factor-induced angiogenesis and vascular permeability. Proc Natl Acad Sci U S A, 2001. 98(5): p. 2604-9.
27. Koike, N., et al., Tissue engineering: creation of long-lasting blood vessels. Nature, 2004. 428(6979): p. 138-9.
28. Au, P., et al., Differential in vivo potential of endothelial progenitor cells from human umbilical cord blood and adult peripheral blood to form functional long-lasting vessels. Blood, 2008. 111(3): p. 1302-5.
29. Samuel, R., et al., Generation of functionally competent and durable engineered blood vessels from human induced pluripotent stem cells. Proc Natl Acad Sci U S A, 2013. 110(31): p. 12774-9.
30. Snuderl, M., et al., Targeting placental growth factor/neuropilin 1 pathway inhibits growth and spread of medulloblastoma. Cell, 2013. 152(5): p. 1065-76.
31. Chauhan, V.P., et al., Normalization of tumour blood vessels improves the delivery of nanomedicines in a size-dependent manner. Nat Nanotechnol, 2012. 7(6): p. 383-8.
32. Chauhan, V.P., et al., Angiotensin inhibition enhances drug delivery and potentiates chemotherapy by decompressing tumour blood vessels. Nat Commun, 2013. 4: p. 2516.
33. Chauhan, V.P., et al., Fluorescent nanorods and nanospheres for real-time in vivo probing of nanoparticle shape-dependent tumor penetration. Angew Chem Int Ed Engl, 2011. 50(48): p. 11417-20.
34. Han, H.S., et al., Spatial charge configuration regulates nanoparticle transport and binding behavior in vivo. Angew Chem Int Ed Engl, 2013. 52(5): p. 1414-9.
35. Goel, S., et al., Effects of vascular-endothelial protein tyrosine phosphatase inhibition on breast cancer vasculature and metastatic progression. J Natl Cancer Inst, 2013. 105(16): p. 1188-201.

36. Fukumura, D., et al., Effect of host microenvironment on the microcirculation of human colon adenocarcinoma. Am J Pathol, 1997. 151(3): p. 679-88.
37. Tsuzuki, Y., et al., Pancreas microenvironment promotes VEGF expression and tumor growth: novel window models for pancreatic tumor angiogenesis and microcirculation. Lab Invest, 2001. 81(10): p. 1439-51.
38. Fukumura, D., et al., Role of nitric oxide in tumor microcirculation. Blood flow, vascular permeability, and leukocyte-endothelial interactions. Am J Pathol, 1997. 150(2): p. 713-25.
39. Yuan, F., et al., Vascular permeability in a human tumor xenograft: molecular size dependence and cutoff size. Cancer Res, 1995. 55(17): p. 3752-6.
40. Lichtenbeld, H.C., et al., Perfusion of single tumor microvessels: application to vascular permeability measurement. Microcirculation, 1996. 3(4): p. 349-57.
41. Dolmans, D.E., et al., Vascular accumulation of a novel photosensitizer, MV6401, causes selective thrombosis in tumor vessels after photodynamic therapy. Cancer Res, 2002. 62(7): p. 2151-6.
42. Tong, R.T., et al., Vascular normalization by vascular endothelial growth factor receptor 2 blockade induces a pressure gradient across the vasculature and improves drug penetration in tumors. Cancer Res, 2004. 64(11): p. 3731-6.
43. Jain, R.K., et al., Endothelial cell death, angiogenesis, and microvascular function after castration in an androgen-dependent tumor: role of vascular endothelial growth factor. Proc Natl Acad Sci U S A, 1998. 95(18): p. 10820-5.
44. Popovic, Z., et al., A nanoparticle size series for in vivo fluorescence imaging. Angew Chem Int Ed Engl, 2010. 49(46): p. 8649-52.
45. Kadambi, A., et al., Vascular endothelial growth factor (VEGF)-C differentially affects tumor vascular function and leukocyte recruitment: role of VEGF-receptor 2 and host VEGF-A. Cancer Res, 2001. 61(6): p. 2404-8.
46. Tsuzuki, Y., et al., Vascular endothelial growth factor (VEGF) modulation by targeting hypoxia-inducible factor-1alpha--> hypoxia response element--> VEGF cascade differentially regulates vascular response and growth rate in tumors. Cancer Res, 2000. 60(22): p. 6248-52.
47. Hagendoorn, J., et al., Onset of abnormal blood and lymphatic vessel function and interstitial hypertension in early stages of carcinogenesis. Cancer Res, 2006. 66(7): p. 3360-4.

Table 1
Examples of *2D* and *3D* method permeability measurements in the E.L. Steele Laboratories

Site	Tumor/model	Animal	Treatment/manipulation	Probes	*2D* methods	*3D* method	References
Brain (cranial window)	U87	Nude/SCID	Anti-VEGF/R2/Ang2/PlGF	BSA	$0.7–3.8\times10^{-7}$ cm/s	$0.4–2.5\times10^{-7}$ cm/s	[14–19]
	U87/MCaIV	SCID	VEGF-GFP imaging	100 and 500 nm QD-NP	NP and VEGF co-localize		[20]
	U87/GL261	*Rag-1−/−*/SCID	nNOS KD/nNOS inhibitor	BSA	$0.3–7.8\times10^{-7}$ cm/s		[21]
	HGL21	SCID	VEGF		$0.11–4.3\times10^{-7}$ cm/s		[14, 22]
	HCaI/Shionogi/MCaIV	SCID		100–550 nm NP	HCaI 210-380, Shionogi 100–380, MCaIV 380–550 nm		[23]
	MCaIV	C3H/SCID		BSA	$1.9–2.9\times10^{-7}$ cm/s		[14]
	R3230AC	Fisher Rat			1.7×10^{-7} cm/s		[14]
	MDA-MB-361HK	SCID	Anti-HER2		$2.7–8.0\times10^{-7}$ cm/s		[24]
	ZR75-1	SCID			1.2×10^{-7} cm/s		[25]
	Tissue-engineered vessels	SCID	HUVEC, CB-EPC + 10T1/2		$0.5–4.4\times10^{-7}$ cm/s		[26–28]
			hiPSC-EC + 10T1/2			$0.2–15\times10^{-7}$ cm/s	[29]
	Normal cranium				$0.2–0.8\times10^{-7}$ cm/s		[22, 26]
Cerebellum window	D283-MED	SCID	Anti-PlGF	BSA		$1.2–3.1\times10^{-7}$ cm/s	[30]
Breast (mammary fat pad window)	E0771/4T1	SCID	Low dose anti-VEGFR2	12, 60, 125 nm Qd NP		0.01–0.45 μm/s Transvascular flux	[31, 32]
	E0771	SCID		Rod, sphere-shape Qd NP		0.04–0.17 μm/s Transvascular flux	[33]
	E0771/MCaIV	SCID		Neutral and negative charge Qd NPs		$0.3–5.0\times10^{-4}$ μm/s Transvascular flux	[34]
	4T1	Nude	VE-PTP inhibitor	BSA		0.1–1.8-fold	[35]
	ZR75-1	SCID		BSA	3.2×10^{-7} cm/s		[25]

Liver (acute)	LS174T	SCID		BSA	4.8×10^{-7} cm/s		[36]
	Normal liver				0.27×10^{-7} cm/s		
Pancreas (abdominal wall window)	Panc-1	SCID		BSA	3.1×10^{-7} cm/s		[37]
	Normal pancreas				0.5×10^{-7} cm/s		
Skin (dorsal skin chamber)	LS174T	SCID	Anti-VEGF, NOS inhibitor	BSA	$1.2–6.0\times10^{-7}$ cm/s		[2, 3, 15, 36, 38]
				90 nm NP	0.2×10^{-7} cm/s		[3]
				Mr. 24,000 (Fc) to 160,000 (IgG)	$1.5–5.7\times10^{-7}$ cm/s		[39]
				BSA	Single vessel permeability		[40]
	MCaIV	C3H/SCID	NOS inhibitor, anti-VEGFR2, PDT		$1.3–2.6\times10^{-7}$ cm/s	3.5×10^{-7} cm/s	[4, 38, 41, 42]
	Shionogi	SCID	Castration		$0.6–3.4\times10^{-7}$ cm/s		[43]
	HCaI/Shionogi/MCaIV			100–2000 nm NP	HCaI 380-550, Shionogi 200–380, MCaIV 1200–2000 nm		[23]
	Mu89 melanoma			12, 60, 125 nm QD-NP		10–250 μm penetration	[44]
	T241		VEGF-C, anti-VEGFR2, VFGF-null	BSA	$0.5–4.4\times10^{-7}$ cm/s		[45]
	hES-teratoma		VEGF KO/HIF-1 KO		$1.3–3.1\times10^{-7}$ cm/s		[46]
	Normal skin				$0.3–0.7\times10^{-7}$ cm/s		[22]
Ear (*in situ*)	Spontaneous SCC	*Pol η−/−*		BSA	$1.2–9.4\times10^{-7}$ cm/s		[47]

4T1 murine breast cancer, *Ang2* angiopoietin 2, *BSA* bovine serum albumin, *CB-EPC* cord blood endothelial progenitor cell, *D283-MED* human medulloblastoma, *E0771* murine breast cancer, *GL261* murine glioma, *HCaI* murine hepatoma, *HER2* human epidermal growth factor receptor 2, *hES* human embryonic stem ells, *hiPSC* human induced pluripotent stem cell, *HUVEC* human umbilical vein endothelial cell, *LS174T* human coon cancer, *Mu89* human melanoma, *nNOS* neuronal nitric oxide synthase, *Panc-1* human pancreatic cancer, *PDT* photodynamic therapy, *PlGF* placenta growth factor, *QD-NP* quantum dot-nanoparticle, *R3230AC* rat breast cancer (rat mammary), *SCC* squamous cell carcinoma, *SCID* severe combined immunodeficient mice, *Shionogi* murine androgen-dependent cancer, *T241* murine fibrosarcoma, *U87* human glioma, *VEGF* vascular endothelial growth factor, *VEGFR2* VEGF receptor 2, *VE-PTP* vascular endothelial protein tyrosine phosphatase, *ZR75-1* human breast cancer

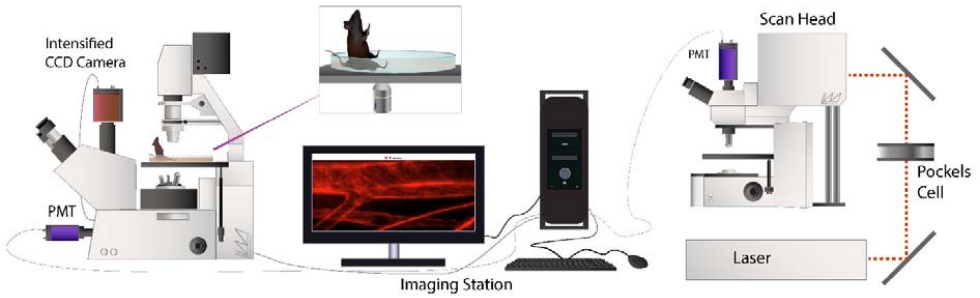

Figure 1. Schematic representation of the fluorescence intravital microscope (left) and multiphoton microscope (right) setups. Fluorescence intravital microscopy and multiphoton microscopy are used for *2D*- and *3D*-method permeability measurements, respectively. Inverted microscope (left) with popliteal lymph node/lymphatics imaging set up is shown. Both inverted and upright (right) microscope with appropriate animal models can be used for the permeability measurements. CCD, cooled coupled device; PMT, photomultiplier tube. This figure was generously drawn by Dr. Lance L. Munn, E.L. Steele Laboratories, Boston, MA.

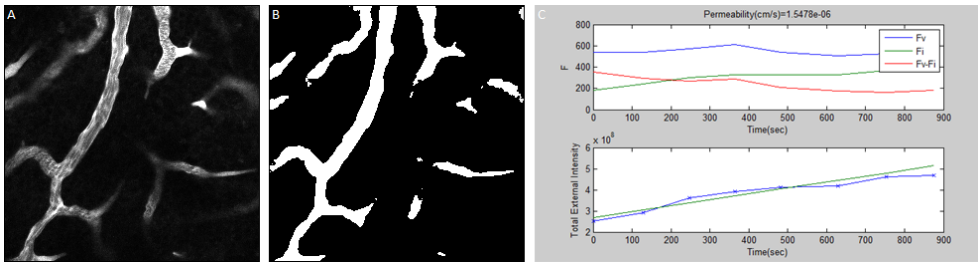

Figure 2. Example of *3D*-method data analysis. A. Single slice from a multiphoton image z stack of tumor vasculature. B. Vessel masking from slice presented at A using method "*Li*" thresholding in ImageJ. C. Right-top graph shows MATLAB results from the same z stack (44 out of 74 slices, z≈81µm, 8 time points over 15 minutes, images not shown) showing a vascular permeability of 1.55 x 10^{-6} cm/s. Right-bottom graph depicts the Total External Intensity (Fe, blue line) being the total fluorescence from all exterior points including those on the wall and the straight line (green line) being the slope estimated from the first 6 time points to which the blue line theoretically should closely adhere to. F, fluorescence intensity; Fv, mean fluorescence from the interior voxels; Fi, mean fluorescence from the vessel wall voxels.

4. In vivo label-free measurement of lymph flow velocity and volumetric flow rates using Doppler optical coherence tomography

Cedric Blatter[1,2], Eelco F. J. Meijer[2,3], Ahhyun S. Nam[1,2,4], Dennis Jones[2,3], Brett E. Bouma[1,2], Timothy P. Padera[2,3,*] & Benjamin J. Vakoc[1,2,*]

[1]Wellman Center for Photomedicine, Massachusetts General Hospital, Boston, Massachusetts 02114, USA. [2]Harvard Medical School, Boston, Massachusetts 02115, USA. [3]Edwin L. Steele Laboratories for Tumor Biology, Department of Radiation Oncology, Massachusetts General Hospital Cancer Center, Boston, Massachusetts 02114, USA. [4]Department of Mechanical Engineering, Massachusetts Institute of Technology, 77 Massachusetts Avenue, Cambridge, Massachusetts 02139, USA. [*]These authors contributed equally to this work. Correspondence and requests for materials should be addressed to B.J.V. (email: bvakoc@mgh.harvard.edu)

Scientific Reports, 2016. 6: p. 29035.
Supporting information available online.

Abstract
Direct *in vivo* imaging of lymph flow is key to understanding lymphatic system function in normal and disease states. Optical microscopy techniques provide the resolution required for these measurements, but existing optical techniques for measuring lymph flow require complex protocols and provide limited temporal resolution. Here, we describe a Doppler optical coherence tomography platform that allows direct, label-free quantification of lymph velocity and volumetric flow rates. We overcome the challenge of very low scattering by employing a Doppler algorithm that operates on low signal-to-noise measurements. We show that this technique can measure lymph velocity at sufficiently high temporal resolution to resolve the dynamic pulsatile flow in collecting lymphatic vessels

Introduction

The lymphatic system drains fluid and metabolic waste from tissues and provides a route for antigen and antigen presenting cells to move from tissue to lymph nodes[1]. When the lymphatic system becomes dysfunctional, whether as a result of trauma, surgery, infection, or other causes, the body's ability to maintain fluid balance and tissue homeostasis is compromised and immune function is impaired. This manifests clinically as lymphedema[2]. Current treatments for lymphedema are limited to palliative measures, such as massage or compression garments, rather than direct repair of the damaged lymphatic system, which would likely be more effective and longer lasting. To this end, preclinical investigations are focused on identifying the biological and molecular regulators of lymph transport in normal and disease settings[3]. In these studies, accurate *in vivo* measurements of lymph flow velocity and lymph volumetric flow will be critical.

Unfortunately, *in vivo* assessment of lymph transport has proven extremely challenging. Because the lymphatic network is filled from the periphery, it is difficult to globally label lymph. Instead, regional labeling is performed by injecting a radioactive, fluorescent or chromatic dye into the tissue and imaging the draining lymphatic vessels[4-8]. While these methods are effective for lymphangiography, i.e., for imaging the morphology of the lymphatic network, their utility for measuring flow and function is limited by several factors. First, the injection of the label alters the interstitial fluid pressure in the tissue, which in turn perturbs the physiological state of the lymphatic system. Thus the method intrinsically changes the parameters to be measured. Second, label-based techniques offer imperfect measurements of flow and are often complex to implement. For example, it is possible to estimate the lymphatic transport by tracking the movement of the fluorescent label front after injection[9]. However, this approach cannot reveal pulsatile flow dynamics and is valid only during the brief initial filling of the targeted vessel. Continuous measurements can be performed by tracking photobleached spots induced by a high-intensity beam. However, these methods are limited by label diffusion and generally yield low-fidelity signals with limited temporal resolution[10]. To avoid the perturbation induced by label-based approaches, methods based on cell tracking within lymphatic vessels have been demonstrated[11]. However, the flow measurements provided by these approaches are intermittent (occurring only when a cell is located within the field of view) and are confounded by the interaction of the cells with the lymphatic endothelium[12]. Finally, lymph "packet" velocity can be measured with near infrared fluorescence techniques. These measurements have been shown to be useful, but are able to only characterize one intermittent aspect of lymph flow dynamics[5,7,13-15]. Because of these technical limitations, the nature and regulation of lymph flow *in vivo* is poorly understood.

Here, we demonstrate direct label-free measurement of lymph flow *in vivo* by Doppler optical coherence tomography (OCT). OCT systems provide spatially localized measurements of optical scattering within tissue[16]. Doppler OCT (DOCT) systems additionally measure the motion of the scatterers and can be used to quantify fluid flow velocity[17-20]. For example, quantitative blood flow imaging by DOCT has been demonstrated in preclinical[21] and clinical[22] applications. However, there are no reports showing DOCT-based measurement of lymph flow. The challenge is not the slower speed of lymph flow relative to blood flow, but rather the profoundly different optical properties of the fluids. Blood is highly scattering and thus produces a significant OCT signal. Lymph is nearly transparent[23-26]; its OCT signal is approximately 20 dB lower than that of blood (Supplementary Fig. 1). Even in optimal imaging conditions, this causes lymph signals to be near the noise floor of the instrument. In this work, we demonstrate that a Doppler shift can be detected

from these extremely small lymph signals. Using the Doppler OCT method, we demonstrate the first continuous *in vivo* measurement of lymph flow with temporal resolutions sufficient to quantify complex pulsatile dynamics. In addition, we demonstrate that the method can also be used to simultaneously measure lymph volumetric flow rates, e.g., measured in μL/h, and lymphatic vessel contraction. The accuracy of the measured flow velocity is confirmed by comparing DOCT and fluorescence photobleaching measurements acquired simultaneously in phantoms and *in vivo* using a multimodal microscope.

Results

Doppler OCT Algorithm Design. Our algorithm operates on a set of repeated OCT measurements acquired from a fixed location within a lymphatic vessel. A three-dimensional OCT image is used to identify the vessel and select the location for flow imaging (Fig. 1a). After acquisition of the repeated measurements, the magnitude of the scattering as a function of depth and time (Fig. 1b) is used to identify the upper and lower boundaries of the lymphatic vessel (methods). The scattering signals at each depth within the lymphatic vessel are then independently analyzed to extract the lymph Doppler signal. Here, it is important that the algorithm used to extract this Doppler signal be tailored to the unique properties of *in vivo* lymph signals. We found that most lymph measurements contain a significant time-invariant signal, likely resulting from nearby highly scattering tissue structures. The magnitude of these static signals is often comparable or higher than that of lymph signals, and cause traditional Doppler methods to fail (Supplementary Fig. 2).

To separate the lymph-specific and static Doppler signals, we employed a modified joint spectral and time domain method[27]. The spectrogram of the complex scattering signal is calculated using a short-time Fourier transform (STFT) (methods, Fig. 1c). In the frequency domain, it is possible to separate the static and lymph signals. The static signal is narrowband and centered at DC (i.e., 0 Hz) while the lymph induces a spectrally broad signal that shifts in proportion to flow velocity. A white noise background is additionally present. To quantify the Doppler properties of the lymph signal separately from the static and noise signals, we fit each spectrum within the spectrogram to a parametric model comprising two Gaussians and a white noise background (methods, Fig. 1d). The center position of the Gaussian describing the spectrally broad signal estimates the Doppler shift induced by lymph flow. To calculate the flow velocity from a measured Doppler shift, it is necessary to know the angle of the velocity vector relative to the imaging beam. This is calculated using the three-dimensional scan data used to initially identify the lymphatic vessel and the flow measurement location (methods, Supplementary Fig. 3).

Validation of DOCT Lymph Flow Velocity Measurements. To validate the accuracy of DOCT for measuring lymph flow velocity, we performed simultaneous measurements with DOCT and a previously described fluorescence photobleaching method[10]. A multimodal microscope was constructed that allowed imaging of a thin sample. Epifluorescence was detected from above and DOCT from below (methods, Fig. 2a). The fluorescence system combined wide-field illumination from an LED source and fixed-point photobleaching using a high-power focused laser. The photobleaching beam was modulated to create short duration (<500 ms) pulses at 3 second intervals. Wide-field fluorescence imaging was performed continuously while the photobleaching beam was off. From these images, the translational speed of the photobleached spot was calculated (methods, Fig. 2b). The DOCT beam was aligned to intersect the photobleaching beam in the

fluorescence image focal plane. The angle of the DOCT beam relative to the imaging plane was 75 degrees. DOCT measurements were recorded simultaneously with fluorescence imaging. Flow velocities were calculated from the DOCT measurements as previously described in this manuscript. To create a fluorescent lymph proxy, we diluted Intralipid® (20%, diluted 1:100 with water) to provide scattering and added Rhodamine-BSA for fluorescence. The scattering signal from the lymph proxy yielded a 7 dB SNR, which matched that of lymph measured from collecting lymphatic vessels *in vivo* (Supplementary Fig. 1).

We confirmed flow accuracy by imaging in microfluidic channels (320 μm width by 100 μm depth) using a pump to vary flow velocity (Fig. 2c,d). The microfluidic channel was larger than a lymph vessel and the channel walls were not as highly scattering as tissue. Thus, many of the challenges of *in vivo* lymph imaging are not recapitulated by the microfluidic phantom. To confirm flow accuracy in an *in vivo* environment, we measured flow in the lymphatic vessels of the mouse ear. The ear was selected because it was thin and compatible with our multimodal microscope that required optical access from both sides. A network of initial lymphatic vessels is present in the ear but these vessels lack the ability to pump and intrinsic flow is limited. To generate flow, a syringe needle was used to inject the lymph proxy at a site distal to a targeted lymphatic vessel. The injection pressure was adjusted to modulate the induced flow velocity. As with the microfluidic measurements, the *in vivo* flow measurements from the two modalities show high correlation (Fig. 2c,d). Additional *in vivo* measurements for validation are shown in Supplementary Fig. 4. We note that the range of induced flow velocities in both the microfluidic and *in vivo* settings (0-400 μm/s) are well matched to physiological flow speeds reported in literature[28]. These measurements provide confirmation that the DOCT method, which has been extensively validated for blood flow imaging[27,29-31], also allows accurate measurement of lymph flow velocity.

M-Mode DOCT Imaging of Pulsatile Lymph Flow Velocity. We prepared the afferent lymphatic vessel of the popliteal lymph node for imaging using established methods[32,33]. Each measurement spanned five minutes. Doppler analysis used a 0.25 sec STFT window (providing 0.25 seconds temporal resolution). A total of 67 measurements were made in 11 animals (Supplementary Table 1). Due to animal motion or pronounced fixed pattern noise that overlapped the lymphatic vessel, no flow measurements were possible in 20 of these 67 measurements. All depths within the lymphatic vessel were analyzed in the remaining 47 measurements to yield the depth and time resolved lymph flow velocity.

In most measurements (37 of 47), we observed a distinct pulsatile flow. The flow pulses were always proximally toward the popliteal lymph node. While most of these measurements (32 of 37) showed no measureable backflow (Fig. 3a), a small subset (5 of 37) exhibited transient backflow after or between pulses (Fig. 3b). In four measurements, oscillatory flow at a higher frequency was observed, but these measurements showed limited net transport (Fig. 3c). As expected, no animals showed a net lymph flow distally—independent of the elevation of the leg relative to the body (Supplementary Fig. 5). The technique showed consistent lymph flow parameters across 45 minutes in a single animal (Supplementary Fig. 6). To our knowledge, these measurements are the first direct and label-free depth-resolved measurements of pulsatile lymph flow velocities *in vivo*. We compared the observed pulsatile lymph flow dynamics to reported values. The pulse interval (time between pulses) was extracted across the 37 measurements (10 animals) that showed strong pulsatile flow (methods, Fig. 3d). The average interval between pulses was 19.8 seconds ± 2.7

seconds (methods). Using fluorescence imaging in the axillary lymphatic vessel, Kwon *et al*. reported a flow pulse interval from 5 to 85 seconds in five animals[6]. Proulx *et al*. observed average pulse intervals of 6.3 seconds, dropping to 4.7 seconds after application of external compression to stimulate the initial lymphatic uptake of tracer[13]. Liao *et al*. also reported an interval between contractions of lymphangions of 1 to 2 seconds in young animals[32]. However, how the contraction of a single lymphangion relates to lymph flow is the subject of active research, and thus contraction and flow intervals may not agree. Transient flow velocity reversals similar to that observed by DOCT (Fig. 3b) were also reported using a cell tracking method[34]. The range of lymph flow velocities in the mouse afferent lymphatic vessel of the popliteal lymph node is not well established. However, the flow velocities measured at this site by DOCT (53 μm/s ± 16 μm/s, methods, Fig. 3e) are in reasonable agreement with relevant reports. Using fluorescence recovery after photobleaching, Bouta *et al.* reported a mean velocity value of 100 μm/s in the hindlimb[28]. In the axillary lymphatic, Kwon *et al.* measured a lymph flow velocity ranging from 280 to 1,350 μm/s, which included larger collecting lymphatic vessels as well. The faster velocities previously reported may have been affected by contrast injections to highlight the lymphatic vessels. Dixon *et al*. reported velocities of 350 to 1,500 μm/s in larger rat mesenteric lymphatic vessels using cell tracking[35].

DOCT-Based Measurement of Lymph Volumetric Flow Rate and Vessel Contraction. The M-Mode Doppler method described above allows flow velocity quantification at a single transverse location with high temporal resolution (0.25 seconds). However, because measurements are limited to this location, it is not possible to calculate the average lymph flow velocity within the vessel (i.e., spatial average across the vessel cross-section). In addition, the dynamic changes in the cross-sectional area of the lymphatic vessel cannot be accurately measured from M-Mode acquisitions. Without each of these parameters, it is not possible to calculate the volumetric lymph flow rates (measured for example in μL/h). To address this, we implemented a second measurement protocol based on B-Mode (frame) Doppler acquisition and analysis. In B-Mode Doppler, temporal resolution is slightly sacrificed to enable two-dimensional imaging of lymph flow in a plane approximately orthogonal to the flow direction. From these B-Mode images, both the cross-sectional area and average flow can be derived.

In a B-Mode Doppler acquisition, the beam was rapidly scanned across the lymphatic vessel (Fig. 4a). We used a sinusoidal scan pattern at 1.04 kHz. With our 50 kHz A-line system, this provided 48 total A-lines per frame (24 in the forward scan and 24 in the backward scan). The scanned field was constrained to ~100 μm, a value chosen to be larger than the lymphatic vessel diameter. We then constructed 48 separate M-Mode measurements associated with each of the 48 A-lines in each frame. In these datasets, the sampling frequency was set by the frame rate (1.04 kHz), whereas the sampling rate in the direct M-Mode method was set by the A-line rate (50 kHz).

The 48 M-Mode datasets were analyzed separately in a manner similar to that described above. The temporal analysis window was expanded to 0.96 seconds (1000 frames). First, the average scattering magnitude was calculated to generate a time-varying anatomical image revealing the lymphatic vessel cross-section (Fig. 4b). The luminal surface of the vessel was segmented from these images (methods, Fig. 4c). Next, Doppler analysis was performed to generate two-dimensional images of flow velocity (Fig. 4d, Supplementary Video 1). From the transverse flow velocity profile and the luminal segmentation, it is straightforward to calculate the average lymph

flow velocity within the vessel (Fig. 4e), the cross-sectional area of the vessel (Fig. 4f), and the volumetric lymph flow (methods, Fig. 4g). We note that the measurement of lymphatic vessel cross-sectional area can also be used to directly monitor lymphatic vessel contraction – a key parameter in the functional assessment of the lymphatic pumping system. To our knowledge, these data represent the first direct and temporally resolved measurement of lymph velocity profiles. The ability of DOCT to simultaneously measure each of these parameters (flow velocity, contraction, and volumetric flow rate) is extremely powerful in studies of lymphatic function[35].
The B-Mode Doppler analysis algorithm was slightly modified from that used for M-Mode analysis because of the longer time separation between measurements (960 µs in B-Mode Doppler vs 20 µs in M-Mode Doppler), and the corresponding reduction in the Nyquist limit (521 Hz vs 25 kHz). Because measured Doppler shifts approach and even exceed this 521 Hz limit, the analysis approach must account for the wrapping effects in the calculated spectrum. We modified the model-fitting algorithm to operate on circular data, i.e., to wrap across the Nyquist boundary (Fig. 4h). After fitting, the detected Doppler shift must be unwrapped to remove jumps by twice the Nyquist frequency. In our studies, the detected Doppler shift only slightly exceeded the Nyquist boundary. This allowed a relatively straightforward unwrapping approach based on remapping the lower quadrant of detected Doppler frequency shifts (methods, Supplementary Fig. 7c).

Discussion

We have demonstrated an imaging technique that allows direct measurement of lymph flow velocity *in vivo*. The method operates without need for injected labels that can alter the physiology to be measured. In addition, the high temporal resolution of the approach reveals pulsatile lymph flow dynamics. Finally, using B-Mode (frame) Doppler methods, the lymph volumetric flow rate can be measured at high temporal resolution. These capabilities address a long-standing need within the lymphatic research field, and the deployment of DOCT could catalyze studies into the regulation and dysregulation of lymph flow in health and disease. As with any new technology, the availability of instrumentation will influence the pace of adoption. The algorithms and methods for lymph flow imaging are not specific to a single OCT implementation, and thus can be adopted to operate in most existing and future systems. This combined with the growing use of OCT in preclinical and biological research may accelerate adoption of DOCT in the lymphatic research community.

OCT technologies can span a large range of spatial resolutions and imaging speeds. The system used here featured moderate resolutions of 6 µm axial and 11 µm transverse and moderate speeds of 50 kHz. Extending these methods to operate with higher resolution OCT systems offering isotropic resolution below 4 µm and speeds above 100 kHz is a promising research direction. Higher resolution will allow a more detailed visualization of lymph flow profiles, and higher speeds can be used to increase the temporal resolution of the frame method, or to simultaneously measure flow at multiple sites within a lymphatic vessel. The latter may allow studies into the coupling of neighboring lymphangions, and the role of this coupling in the generation of lymph flow. Until now, such studies rely solely on modeling[36,37].

A drawback of the approach is the limited imaging depth, which required resection of the skin in the hindlimb lymphatic model. OCT has an imaging penetration of approximately 2 mm, but even within this range signals attenuate rapidly with depth. The lymphatic vessels imaged in these studies were superficial and it is not clear if the technique can translate to vessels that are more

than several hundred microns below the tissue surface. This limitation is not unique to OCT as high-resolution fluorescence-based techniques also require the removal of skin[32,33]. Methods using near-infrared fluorescence can increase imaging depth, but are not able to image wall motion to measure lymphatic contraction without skin removal due to skin scattering[13,33,38]. Though DOCT currently requires skin removal, it advances the field of lymphatic research by enabling label-free, high-speed, and simultaneous measurements of lymphatic contraction, lymph flow velocity, and lymph volumetric flow in this experimental setting.

Methods

DOCT instrumentation. Hindlimb and ear/microfluidic imaging was performed with two separate but similarly designed custom-built DOCT systems. The design of the instrument used for hindlimb imaging is summarized in Supplementary Fig. 8 and described in more detail in Ref. 39. The system used a polygon mirror swept-wavelength laser source. The axial scan rate was 50 kHz, with a full optical bandwidth of 100 nm, centered at ~1300 nm, giving a 5.3 μm axial resolution in tissue. With 10 mW on the sample, this system provides a sensitivity of ~105 dB. The beam is collimated to 2.8 mm and focused with a scan lens (LSM02, Thorlabs), giving a theoretical scanning beam spot size on the tissue in the center of the field of view of ~11 μm. Background subtraction, dispersion compensation, k-space interpolation, Fourier transformation and image generation are performed as previously described[39]. Three fix delay reflections were added to each system as reference for phase instability correction[40-43]. Phase instability occurs in wavelength-swept source based OCT systems because of imperfect synchronization of the acquisition system with the laser sweep. It has been shown that this results in trigger jitter which induces timing fluctuations of the interference signal and corresponding depth-dependent phase errors between A-scans. The first reflection was obtained by using a 4% beam sampler (partial reflection mirror) and a mirror in the free-space sample arm. It was placed at zero-delay to correct for depth-invariant phase shifts by subtracting the phase evolution at that depth from the entire M-scan[40]. The second reflection is obtained by sampling a portion of the sample light with a fiber coupler. This light is directed to a separate free-space path containing a microscope glassplate. The front and back surfaces of this glassplate provide the second and third calibrating signals. These signals are placed at the edge of the imaging range and used to correct for depth-dependent phase jitter. More specifically, the position of these signals relative to the zero-delay position and associated phase signals are used to calculate a linear phase term in depth in each A-scan, which is subtracted from that A-scan[40].

The system used for validation studies was similar to that described above but had the following differences. It operated at an A-line rate of 80 kHz with a 140 nm bandwidth centered at 1285 nm, giving a ~5 μm axial resolution in tissue. The power on the sample was ~10 mW and the sensitivity around 105 dB. The microscope for this system is illustrated in Supplementary Fig. 9. This system did not include a beam scanner; the signal was measured at a single location with a spot size of ~23 μm.

Animal preparation. For fluorescence photobleaching/DOCT experiments using the multimodal microscope (Fig. 2), 8-12 week old nude female mice (28-32g) were used. Nude mice were selected to eliminate hair from the imaging field. The mice were anesthetized using a Ketamine/Xylazine 90mg/9mg per kg body weight. After confirmation of anesthetic plane, mice were placed in prone position with the ventral side of the right ear on a 1 cm elevated translucent

glass cover slip. The edge of the ear was circumferentially held in position using ½ inch wide tape. A small drop of water under the ventral side of the ear adhered the ear to the cover glass. A 30 ½ gauge needle connected to PE10 Polyethylene Tubing and a ½ cc U-100 28 ½ gauge insulin syringe was carefully inserted between skin layers in the tip of the ear. The insulin syringe was attached to a syringe pump (Pump11 Elite, Harvard Apparatus) to control injection speed. A Rhodamine-BSA (Invitrogen Catalog #A23016)/0.2% Intralipid® (Fresenius Kabi, 20% diluted 1:100 with water) 1:1 mixture was injected at 5μL/min for 2 seconds to generate flow in the lymphatic vessels.

For DOCT experiments in the hindlimb (Fig. 3, 4), 8-16 week old C3H male mice (26-36g) were used. Again, mice were anesthetized using a Ketamine/Xylazine 90mg/9mg per Kg body weight. The surgical procedure was performed as described in Liao *et al.*, *PNAS*[32] and Liao *et al*., *Journal of Biological Methods*[33]. Exposed tissue was kept hydrated using physiological saline. Mice were euthanized at the conclusion of the imaging experiment. The animal experiment protocol was reviewed and approved by Institutional Animal Care and Use Committee of the Massachusetts General Hospital. The procedures were performed in accordance with the approved guidelines.

Data analysis. The interval between pulses was measured from the depth averaged velocity vs time profiles. Peaks were located by the Matlab findpeaks function with a minimum peak height larger than one third of the mean of the five largest peak amplitudes. The boxplots were calculated with the Matlab function of this name. The central red line indicates the median, while the lower and upper edges of the box are the 25th and 75th percentiles respectively. When shown, the whiskers extend to the lowest and highest datum still within 1.5 the interquartile range of respectively the lower and the upper quartile. Outliers are plotted as individual red crosses if they are not included between the whiskers.

The average interval and average mean velocity were calculated by first averaging the measurements taken in each single animal and then averaging over the group by animal. The error reported is the standard error of the mean (S.E.M.) calculated based on the animal to animal variability.

DOCT hindlimb imaging procedure. The mouse was placed on a tilted stage (15 degrees) to generate a Doppler angle (Supplementary Fig. 3a). A primary artery/vein pair was visible by eye and was used to locate the likely position of the lymphatic vessel (runs approximately parallel to the blood vessels). The animal was positioned such that these vessels align to the direction of maximum slope. The stage was then mechanically attached to the optical table, oriented such as having the maximum slope perpendicular to the fast axis scanning direction (Supplementary Fig. 3a). Real-time OCT cross-sectional structural images (fast axis scanning, slow axis amplitude set to zero) were used to locate the lymphatic vessels on either side of the blood vessel. The image reconstruction was performed to generate isotropic images (same transverse and depth scale factors). This simplified discrimination of approximately round lymphatic vessels from other low-scattering structures such as fat cells. By moving the imaged frame along the slow-axis direction, the continuity of the presumed lymphatic vessel was confirmed. This also allowed confirmation that the lymphatic vessel runs along the direction of maximal slope. If not, another location can be chosen or the stage can be rotated. Next, the lymphatic vessel of interest was laterally centered in the field of view by motion of a translation stage. Finally, a three-dimensional volume spanning a

1.4 x 1.4 mm scanning area (464 A-Scans per B-Scans, 464 B-Scans) was acquired (Supplementary Video 2). This volume was then analyzed in ImageJ (NIH) to confirm the position and orientation of the lymphatic vessel. This three-dimensional dataset was also used to later measure the Doppler angle (see section Calculation of Doppler angle).

DOCT/fluorescence imaging procedure. The fluorescence system is a slightly modified version of a previous experimental system[10]. The schematic representation of the experimental setup is shown in Supplementary Fig. 9. Fluorescence images were obtained with a 20X 0.40 NA objective (LD Achroplan, Zeiss) mounted in an epifluorescence microscope (Axioskop, Zeiss). Wide-field illumination was performed through the epi-illumination port of the microscope by a green collimated LED (M530L3-C4, Thorlabs). The filter-set was a standard combination for TRITC/CY3.5. The images were acquired with an intensified charge-coupled device videocamera (C2400-68, Hamamatsu Photonics) and digitized with a USB frame grabber (USB-AVCPT, Sabrent) at 30 frames/s. A CW 532nm laser (Verdi, Coherent) combined with a fast electronic shutter (LS6Z2, Uniblitz) were used to induce photobleaching. The laser path was overlapped on the LED illumination by using a beam-splitter, and aligned to appear in the center of the field of view. A second shutter was placed before the camera to prevent over exposure during photobleaching. The operation of the shutters was controlled with a USB interface card (NI USB 6259, National Instruments) driven by Labview (National Instruments). The laser power on the sample was ~50 mW. The shutter was open to the laser for durations of ~100 ms and ~500 ms every ~3 seconds for the *in vivo* and *in vitro* experiment respectively. The DOCT sample beam illuminated the sample from the bottom side of the microscope. The light was collimated, focused and reflected on the hypotenuse of a right angle prism to introduce a 75 degree Doppler angle. For alignment purposes, red light was coupled into the system to center the DOCT spot on the field of view to overlap with the photobleaching spot. The DOCT beam and the direction of motion define the z-x plane. The x direction corresponds to horizontal lines on the camera image. M-Scan acquisition and frame video recording were started manually approximately at the same time. Each sequence of frames following a laser illumination was processed individually to obtain a single velocity value. The first five frames after the shutter opening were used to estimate the velocity. After these frames, the photobleached spot had either translated out of the field of view, or had faded due to diffusion. Background fluorescence frames were calculated using 30 frames acquired during the time-period after the photobleached spot had disappeared. This background frame was subtracted from each of the five analyzed fluorescence images to enhance contrast for the photobleached spot. Each image was later vertically averaged along the direction perpendicular to the flow velocity to obtain an intensity profile. The minimum of that profile, which corresponds approximately to the photobleached spot centroid, was located fitting the measured profile to a 11^{th} order polynomial curve and finding the minimum of that curve. The location of the minimum over the five frames was fit to a linear curve. The velocity was extracted as the slope of this fitted line.

M-Mode and B-Mode Doppler processing. Detailed steps involved in the Doppler analysis of M-Mode (Fig. 3) and B-Mode (Fig. 4) datasets are presented in Supplementary Notes 1 and 2, respectively.

Calculation of Doppler angle. The Doppler angle was measured using the three-dimensional dataset acquired prior to each flow velocity measurement (see DOCT hindlimb imaging

procedure). A single cross-sectional image aligned to the longitudinal axis of the lymphatic vessel was generated (Supplementary Fig. 3a,b). Because the lymphatic vessel does not necessarily align parallel to the tissue surface, it was necessary to measure the vessel angle directly including the influence of refraction at the air/tissue boundary. Within this image, we draw two right angle triangles aligned to the tissue and vessel boundaries (Supplementary Fig. 3b). Each triangle is drawn with the same transverse extent Δ. Next, the physical distances (e.g., measured in μm by multiplying the number of pixels by the scale factor) for the transverse and depth sides (Δz_a and Δz_t) of these two triangles are measured. We note that the depth distance must take into account the different scale factor (e.g., μm/pixel) in the depth dimension for air (n = 1) and tissue (n_t = 1.38) spaces. These distances are illustrated on Supplementary Fig. 3b. The Doppler angle can then be calculated from these parameters and the index of refraction of tissue, n_t, as:

$$\tan(90-\alpha) = \frac{\Delta z_t n_t}{\sqrt{\Delta z_a{}^2 (n_t{}^2 - 1) + (\Delta \cdot n_t)^2}}. \quad (1)$$

The derivation of this expression is presented in Supplementary Note 3.

Acknowledgements
Research reported in this publication was supported in part by the Center for Biomedical OCT Research and Translation through Grant Number P41EB015903, awarded by the National Institute of Biomedical Imaging and Bioengineering of the National Institutes of Health, by the National Institutes of Health under award numbers R01CA163528 (B.J.V.), DP2OD008780 (T.P.P.), R21AI097745 (T.P.P.), R01HL128168 (T.P.P.) and F32CA183465 (D.J.). The National Cancer Institute Federal Share of Proton Income also supported this work (T.P.P., B.J.V.). Cedric Blatter was supported by a Swiss National Science Foundation early post-doctoral mobility fellowship (P2SKP2_158640). Dennis Jones was supported by a Burroughs Wellcome Fund postdoctoral award and UNCF-Merck postdoctoral fellowship. The authors acknowledge Matthias Geissbuehler for a modified StackReg ImageJ plugin.

Author contributions
T.P.P., and B.J.V. initiated the project. C.B. and E.FJ.M. collected the data. C.B. processed the data. C.B., E.FJ.M., T.P.P., and B.J.V. conceived the method and analyzed data; A.S.N., D.J. and B.B. contributed to the system development. C.B., E.FJ.M., T.P.P., and B.J.V. wrote the manuscript. All authors contributed to the final version of the manuscript.

References
1. Pereira, E. R., Jones, D., Jung, K. & Padera, T. P. The lymph node microenvironment and its role in the progression of metastatic cancer. Semin. Cell. Dev. Biol. 38, 98-105 (2015).
2. Mortimer, P. S. & Rockson, S. G. New developments in clinical aspects of lymphatic disease. J. Clin. Invest. 124, 915-921 (2014).
3. Kesler, C. T., Liao, S., Munn, L. L. & Padera, T. P. Lymphatic vessels in health and disease. WIREs Syst. Biol. Med. 5, 111-124 (2013).
4. Padera et al., "Lymphatic Metastasis in the Absence of Functional Intratumor Lymphatics," Science 296, 1883-1886 (2002).
5. Sharma, R. et al. Quantitative imaging of lymph function. Am. J. Physiol. Heart Circ. Physiol. 292, 3109–3118 (2007).
6. Kwon, S. & Sevick-Muraca, E. M. Noninvasive Quantitative Imaging of Lymph Function in Mice. Lymphat. Res. Biol. 5, 219-232 (2007).

7. Rasmussen, J. C., Tan, I.-C., Marshall, M. V., Fife, C. E. & Sevick-Muraca, E. M. Lymphatic imaging in humans with near-infrared fluorescence. Curr. Opin. Biotechnol. 20, 74-82 (2009).
8. Zhou, Q., Wood, R., Schwarz, E. M., Wang, Y.-J. & Xing, L. Near-infrared lymphatic imaging demonstrates the dynamics of lymph flow and lymphangiogenesis during the acute versus chronic phases of arthritis in mice. Arthritis Rheum. 62, 1881-1889 (2010).
9. Swartz, M. A., Berk, D. A. & Jain, R. K. Transport in lymphatic capillaries. I. Macroscopic measurements using residence time distribution theory. Am. J. Physiol. 270, 324-329 (1996).
10. Berk, D. A., Swartz, M. A., Leu, A. J. & Jain, R. K. Transport in lymphatic capillaries. II. Microscopic velocity measurement with fluorescence photobleaching. Am. J. Physiol. Heart Circ. Physiol. 270, 330-337 (1996).
11. Dixon, J. B., Zawieja, D. C., Gashev, A. A. & Cote, G. L. Measuring microlymphatic flow using fast video microscopy. J. Biomed. Opt. 10, 064016-1-7 (2005).
12. Nitschke, M. et al. Differential requirement for ROCK in dendritic cell migration within lymphatic capillaries in steady-state and inflammation. Blood 120, 2249-2258 (2012).
13. Proulx, S. T. et al. Use of a PEG-conjugated bright near-infrared dye for functional imaging of rerouting of tumor lymphatic drainage after sentinel lymph node metastasis. Biomaterials 34, 5128–5137 (2013).
14. Nelson, T. S. et al. Minimally invasive method for determining the effective lymphatic pumping pressure in rats using near-infrared imaging. Am. J. Physiol. Regul. Integr. Comp. Physiol. 306, 281-290 (2014).
15. Sevick-Muraca, E. M. et al. Imaging of Lymph Flow in Breast Cancer Patients after Microdose Administration of a Near-Infrared Fluorophore: Feasibility Study. Radiology 246, 734–741 (2008).
16. Huang, D. et al. Optical coherence tomography. Science 254, 1178–1181 (1991).
17. Chen, Z. et al. Noninvasive imaging of in vivo blood flow velocity using optical Doppler tomography. Opt. Lett. 22, 1119-1121 (1997).
18. Izatt, J. A., Kulkarni, M. D., Yazdanfar, S., Barton, J. K. & Welch, A. J. In vivo bidirectional color Doppler flow imaging of picoliter blood volumes using optical coherence tomography. Opt. Lett. 22, 1439-1441 (1997).
19. Leitgeb, R. A. et al. Real-time assessment of retinal blood flow with ultrafast acquisition by color Doppler Fourier domain optical coherence tomography. Opt. Express 11, 3116–3121 (2003).
20. White, B. et al. In vivo dynamic human retinal blood flow imaging using ultra-high-speed spectral domain optical coherence tomography. Opt. Express 11, 3490-3497 (2003).
21. Srinivasan, V. J. et al. Quantitative cerebral blood flow with optical coherence tomography. Opt. Express 18, 2477-2494 (2010).
22. Wang, Y. et al. Pilot study of optical coherence tomography measurement of retinal blood flow in retinal and optic nerve diseases. Invest. Ophthalmol. Vis. Sci. 52, 840-845 (2011).
23. Luo, W. et al. Optical biopsy of lymph node morphology using optical coherence tomography. Technol. Cancer Res. T. 4, 539–548 (2005).
24. Vakoc, B. J. et al. Three-dimensional microscopy of the tumor microenvironment in vivo using optical frequency domain imaging. Nat. Med. 15, 1219–1223 (2009).
25. McLaughlin, R. A. et al. Imaging of human lymph nodes using optical coherence tomography: potential for staging cancer. Cancer Res. 70, 2579–2584 (2010).

26. Zhi, Z., Jung, Y. & Wang, R. K. Label-free 3D imaging of microstructure, blood and lymphatic vessels within tissue beds in vivo. Opt. Lett. 37, 812–814 (2012).
27. Szkulmowski, M., Szkulmowska, A., Bajraszewski, T., Kowalczyk, A. & Wojtkowski, M. Flow velocity estimation using joint Spectral and Time domain Optical Coherence Tomography. Opt. Express 16, 6008-6025 (2008).
28. Bouta, E. M. et al. In vivo quantification of lymph viscosity and pressure in lymphatic vessels and draining lymph nodes of arthritic joints in mice. J. Physiol. 592, 1213-1223 (2014).
29. Szkulmowska, A., Szkulmowski, M., Kowalczyk, A. & Wojtkowski, M. Phase-resolved Doppler optical coherence tomography-limitations and improvements. Opt. Lett. 33, 1425–1427 (2008).
30. Kagemann, L., Wollstein, G., Ishikawa, H., Townsend, K. A. & Schuman, J. S. Validation of Spectral Domain Optical Coherence Tomographic Doppler Shifts Using an In Vitro Flow Model. Invest. Ophthalmol. Vis. Sci. 50, 702-706 (2009).
31. Walther, J., Mueller, G., Morawietz, H. & Koch, E. Analysis of in vitro and in vivo bidirectional flow velocities by phase-resolved Doppler Fourier-domain OCT. Sensor Actuat. A-Phys. 156, 14-21 (2009).
32. Liao, S. et al. Impaired lymphatic contraction associated with immunosuppression. Proc. Natl. Acad. Sci. USA 108, 18784-18789 (2011).
33. Liao, S., Jones, D., Cheng, G. & Padera, T. P. Method for the quantitative measurement of collecting lymphatic vessel contraction in mice. J. Biol. Methods 1, e6 (2014).
34. Dixon, J. B., Gashev, A. A., Zawieja, D. C., Moore, J. E. Jr. & Cote, G. L. Image correlation algorithm for measuring lymphocyte velocity and diameter changes in contracting microlymphatics. Ann. Biomed. Eng. 35, 387-396 (2007).
35. Dixon, J. B. et al. Lymph flow, shear stress, and lymphocyte velocity in rat mesenteric prenodal lymphatics. Microcirculation 13, 597-610 (2006).
36. Jamalian S., Bertram, C. D., Richardson, W. J. & Moore, J. E. Jr. Parameter sensitivity analysis of a lumped-parameter model of a chain of lymphangions in series. Am. J. Physiol. Heart Circ. Physiol. 305, 1709-17 (2013).
37. Bertram, C. D., Macaskill, C., Davis, M. J & Moore, J. E. Jr. Development of a model of a multi-lymphangion lymphatic vessel incorporating realistic and measured parameter values. Biomech. Model. Mechan. 13, 401-416 (2014).
38. Weiler, M., Kassis, T. & Dixon, J. B. Sensitivity analysis of near-infrared functional lymphatic imaging. J. Biomed. Optics 17, 066019-1-10 (2012).
39. Bouma, B. E., Yun, S. H., Vakoc, B. J., Suter, M. S. & Tearney, G. J. Fourier-domain optical coherence tomography: recent advances toward clinical utility. Curr. Opin. Biotechnol. 20, 111-118 (2009).
40. Vakoc, B., Yun, S., de Boer, J., Tearney, G. & Bouma, B. Phase-resolved optical frequency domain imaging. Opt. Express 13, 5483-5493 (2005).
41. Braaf, B. et al. Phase-stabilized optical frequency domain imaging at 1-µm for the measurement of blood flow in the human choroid. Opt. Express 19, 20886-20903 (2011).
42. Baumann B. et al. Total retinal blood flow measurement with ultrahigh speed swept source/Fourier domain OCT. Biomed. Opt. Express 2, 1539-1552 (2011).
43. Hong Y.-J. et al. High-penetration swept source Doppler optical coherence angiography by fully numerical phase stabilization. Opt. Express 20, 2740-2760 (2012).

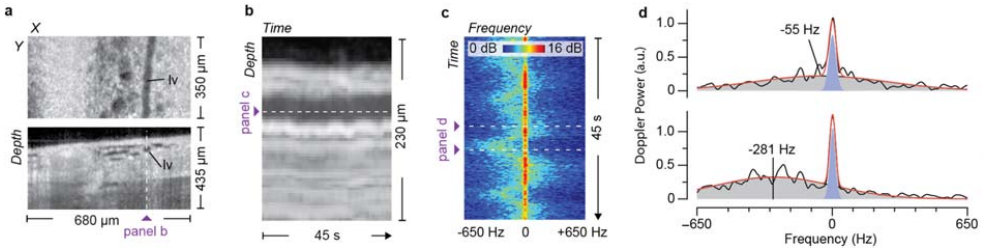

Figure 1. Illustration of the method to measure lymphatic flow velocity with DOCT under low SNR settings and in the presence of artifacts from neighboring static tissue signals. (**a**) Three-dimensional OCT datasets viewed in *en face* (upper panel) and cross sectional (lower panel) presentations are used to identify lymphatic vessels and select the location for flow measurement. (**b**) The depth-resolved OCT signal at a fixed transverse (x,y) location is recorded for five minutes and used to generate an M-Mode intensity image to identify the lymphatic vessel upper and lower boundaries. Depths within the lymphatic vessel are analyzed using Doppler methods. (**c**) A spectrogram is obtained for each depth, here shown for the depth indicated by the dashed line in (**b**). (**d**) Spectra showing the static and lymph signals at times of small (upper panel, -55Hz) and moderate (lower panel, -281Hz) Doppler shifts. Each spectral curve (black trace) within the spectrogram (panel **c**) is fit to a parametric model comprising two Gaussians and a white noise background (red trace). One Gaussian represents the static component and is centered at 0 Hz (blue peak). The second Gaussian represents the component due to lymph flow and is a broad distribution centered on the Doppler frequency (grey peak). The sign of the Doppler frequency shift denotes the direction of flow relative to the imaging beam.

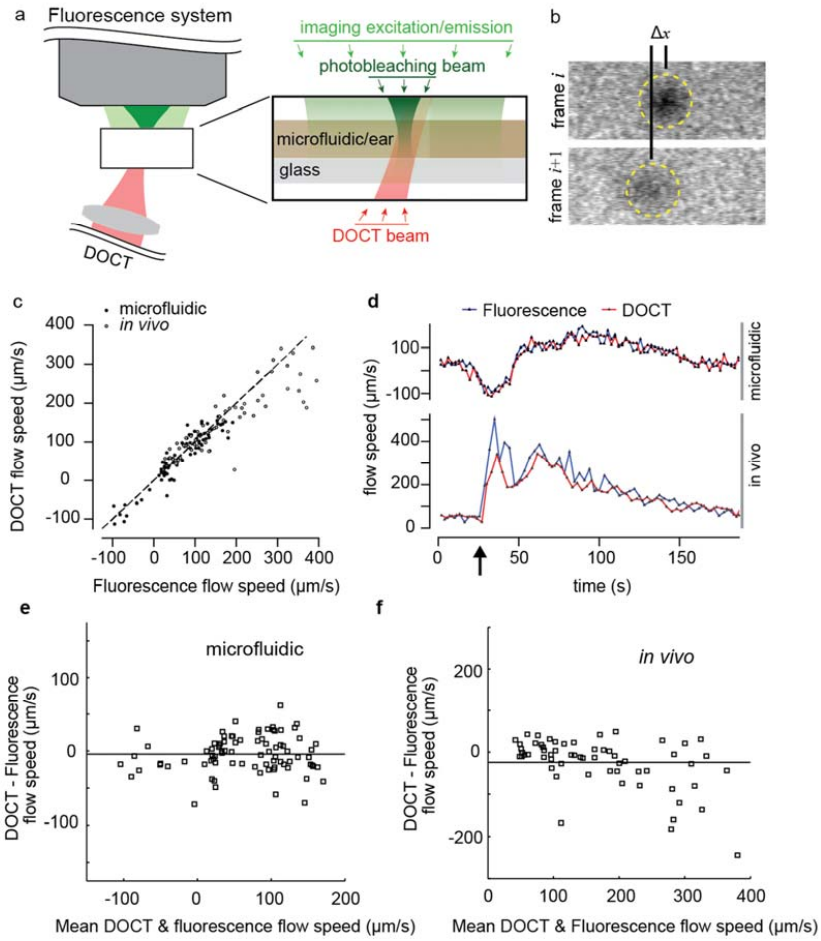

Figure 2. Comparison of DOCT and fluorescence photobleaching measurements of lymph proxy flow in microfluidic phantoms and *in vivo*. (**a**) Schematic of the experimental setup showing fluorescence widefield illumination (light green), focused and pulsed illumination for photobleaching (dark green) and DOCT (red). (**b**) Two cropped fluorescence frames taken from the video sequence acquired immediately after creation of a photobleached spot (in a microfluidic phantom). The translation of the spot is used to calculate flow velocity. (**c**) Comparison of simultaneous DOCT and fluorescence based flow velocity measurements in the microfluidic phantom and mouse ear. (**d**) The time-resolved velocity measurements from DOCT and fluorescence modalities in the microfluidic and *in vivo* experiments. Note that the larger discrepancies between the modalities in the *in vivo* measurements occur from 25 seconds to 65 seconds, immediately after creation of the flow bolus (arrow) when flow velocity is changing rapidly. (**e**) & (**f**) Bland-Altman plots, displaying the difference between DOCT and fluorescence flow measurements compared to the mean flow speed, show agreement between the two modalities in the microfluidic and *in vivo* experiments respectively.

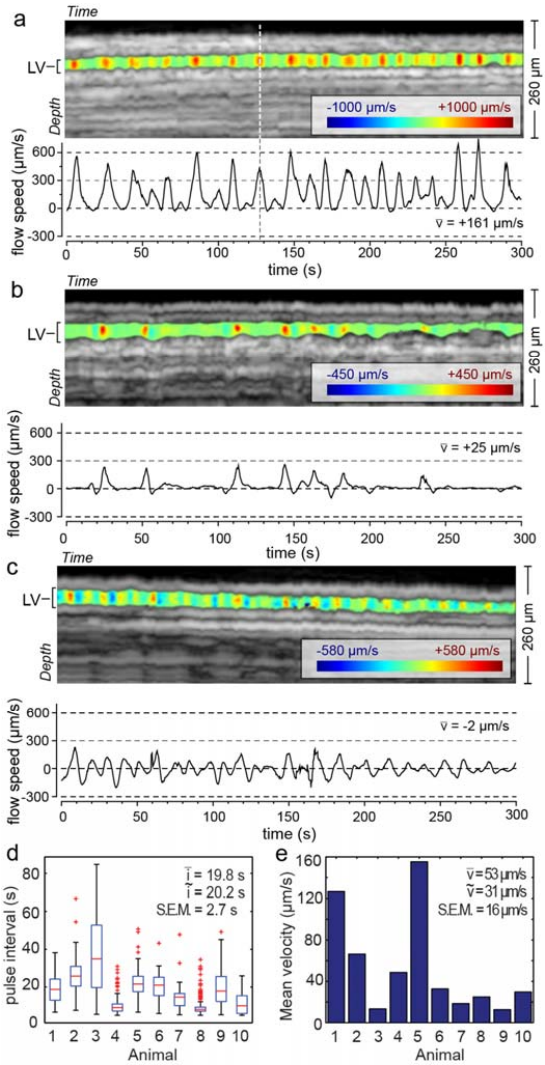

Figure 3. M-Mode DOCT measurement of pulsatile lymph flow velocity. (**a**) Depth and time-resolved flow velocity in the lymphatic vessel lumen overlaid on the M-Mode intensity image. The measurement location is highlighted in Fig. 1(**a**). The positive velocity indicates flow proximally toward the body. The animal leg was lying lower than the abdomen. The flow direction was therefore against gravity. A velocity time trace was calculated by averaging the flow velocity in the vessel over the lymphatic vessel (LV) depth. The maximum amplitude of this velocity is smaller than in the image above because of this depth averaging. (**b**) An M-Mode measurement showing periods of backflow. (**c**) A measurement in another animal showing an oscillatory flow velocity at relatively higher frequency than pulsatile flow exemplified by panel (**a**). (**d**) The average pulse interval for 10 animals showing pronounced pulsatile flow dynamics. The box plot for each animal includes data obtained over multiple five minute duration measurements. The mean pulse interval is 19.8 seconds and is much longer than respiratory or cardiac cycles. (**e**) The mean flow velocity in the same animals as in (**d**) calculated as the average over individual five minute measurements. $\bar{x}$, $\tilde{x}$ and S.E.M. denote mean, median and standard error of the mean respectively.

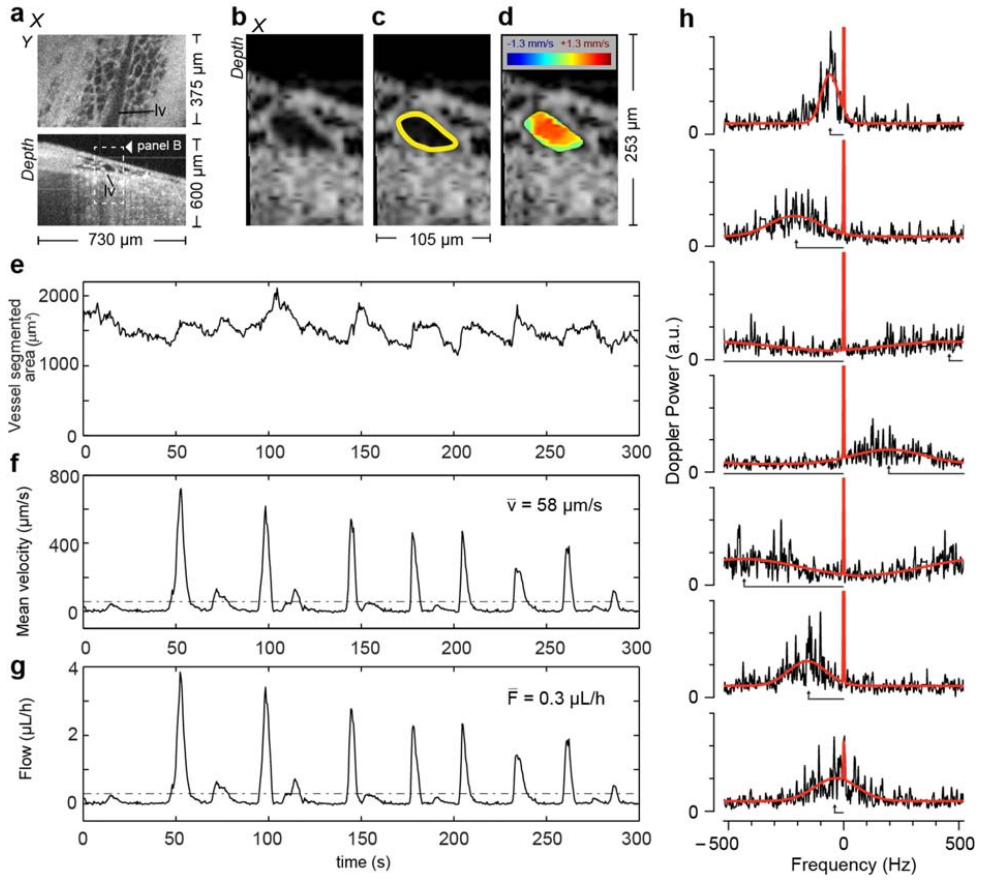

Figure 4. B-Mode DOCT measurement of spatially and temporally resolved lymph flow velocity, vessel cross-sectional area and volumetric flow rates. (**a**) Three-dimensional OCT datasets viewed in *en face* (upper panel, lv: lymphatic vessel) and cross-sectional (lower panel) presentations are used to identify lymphatic vessels and select the flow measurement cross-section. Representative image of the time series (Supplementary Video 1) showing the vessel cross-section (**b**), its segmentation result (**c**, yellow curve) and the calculated flow velocity spatial distribution (**d**). The velocity image was filtered with a two dimensional median filter and unwrapped. (**e**) The segmented cross-sectional area of the lymphatic vessel is reported over the five minutes measurement. (**f**) The mean velocity calculated over the vessel cross-sectional area is reported with its mean value indicated by the dashed line. (**g**) The lymphatic volumetric flow is calculated as the product of the cross-sectional area and the mean velocity (methods). The velocity measurement resolves the pulsatile flow, similar to previous measurements. Interestingly, the vessel cross-section profile shows changes in accordance with the flow pulses. (**h**) Seven spectra (black line) at a particular spatial location in the vessel during a flow pulse show high velocity frequency components being wrapped, i.e. appearing on the right side of the frequency scale. The fitting model in red operates on a circular coordinate system. The length of the black arrow pointing to the center of the broad Gaussian indicates the value of the frequency/velocity estimator after unwrapping.

5. Simultaneous measurements of lymphatic vessel contraction, flow and valve dynamics in multiple lymphangions using optical coherence tomography

Cedric Blatter[1,3,§], Eelco F.J. Meijer[2,3,§], Timothy P. Padera[2,3,‡], Benjamin J. Vakoc[1,3,‡,*]

[1]Wellman Center for Photomedicine, Massachusetts General Hospital, Boston, Massachusetts 02114, USA; [2]Edwin L. Steele Laboratories for Tumor Biology, Department of Radiation Oncology, Massachusetts General Hospital Cancer Center, Boston, Massachusetts 02114, USA; [3]Harvard Medical School, Boston, Massachusetts 02115, USA. [§, ‡] Authors contributed equally. *Correspondence and requests for materials should be addressed to (email: bvakoc@mgh.harvard.edu)

Journal of Biophotonics, 2017. 0:e201700017.
Supporting information available online.

Abstract
Lymphatic dysfunction is involved in many diseases including lymphedema, hypertension, autoimmune responses, graft rejection, atherosclerosis, microbial infections, cancer and cancer metastasis. Expanding our knowledge of lymphatic system function can lead to a better understanding of these disease processes and improve treatment options. Here, optical coherence tomography (OCT) methods were used to reveal intraluminal valve dynamics in 3 dimensions, and measure lymph flow and vessel contraction simultaneously in 3 neighboring lymphangions of the afferent collecting lymphatic vessels to the popliteal lymph node in mice. Flow measurements were based on Doppler OCT techniques in combination with exogenous lymph labeling by Intralipid. Through these imaging methods, it is possible to study lymphatic function and pumping more comprehensively. These capabilities can lead to a better understanding of the regulation and dysregulation of lymphatic vessels in health and disease. The image depicts the dynamic measurements of lymphatic valves, lymphatic vessels cross-sectional area and lymph velocity simultaneously measured in vivo with optical coherence tomography.

Introduction

The lymphatic system is critical for maintaining tissue fluid balance, generating adaptive immune responses and carrying lipids absorbed in the gut to the blood circulation. Consequently, lymphatic impairment can lead to tissue swelling, immune dysfunction and gut malabsorption. Moreover, a large array of diseases is related to lymphatic dysfunction including lymphedema, hypertension, autoimmune responses, graft rejection, atherosclerosis, microbial infections, cancer and cancer metastasis [1]. Therefore, expanding our knowledge of normal lymphatic function, as well as lymphatic dysfunction in disease settings, is of paramount importance to understanding these pathologies and exploring new treatment options.

The lymphatic system consists of lymph nodes, an extensive network of lymphatic vessels and circulating lymph. Lymph enters the system through a network of initial lymphatic vessels embedded in tissue (Fig. 1a). These initial lymphatics feed into a network of larger pre-collecting and collecting vessels that drain to lymph nodes, where systemic immune responses are initiated. After exiting lymph nodes, lymph is transported to the venous angles in the neck where it returns to the systemic circulation [2]. The lymphatic collecting vessels primarily serve to actively transport lymph along this route, often against external forces. This active pumping of lymph is achieved by a combination of lymphatic contractions—both active and passive—that force lymph forward, and intraluminal valves that prevent net backflow. This action is distributed along a collecting lymphatic vessel, which comprises a series of lymphangions—the segments between two valves. Each lymphangion is invested by lymphatic muscle cells [3] to provide contraction forces. Through the coordinated contraction of multiple lymphangions, lymph flow is driven forward [4]. However, the nature and mechanisms for lymphangion coordination and valve action in normal states, or the disruption of this coordination in disease states are not well understood.

To deepen the understanding of lymphatic function, lymphatic imaging technologies have been developed and deployed in preclinical and clinical settings. In the clinic, lymphoscintigraphy [5, 6] and near infrared (NIR) fluorescence imaging [7] have been used to assess the severity of lymphatic dysfunction. MRI [8] and CT [9] provide more information regarding anatomical status for treatment planning, for example in treating advanced lymphedema. In preclinical settings, *ex vivo* experiments [10, 11] and computational modelling [4, 12] have given great insight into the behavior of lymphatic valves and lymphangions and their possible functioning *in vivo*. Lymphatic pumping frequency has been assessed non-invasively with NIR fluorescence imaging [13-15]. To provide higher-resolution imaging of lymphatic vessels, fluorescence microscopy (FM) can be used after surgical removal of overlying skin. This method has been used to resolve the diameter change of the lymphatic vessel with each contraction and visualizing valve action [13, 16]. Optical coherence tomography (OCT) provides label-free three-dimensional (3D) imaging of tissue scattering at micron-scale resolutions. The optical biopsy capability of OCT has been successfully demonstrated for imaging lymph nodes [17-20]. The scattering difference between the relatively acellular lymph and the surrounding tissue has been used as a contrast mechanism to image the lymphatic network [21-27]. While these techniques provide insight into specific aspects of lymphatic function, they are unable to directly assess lymph flow.

Doppler OCT (DOCT) analyzes scattering signals over time to measure motion along the optical beam [28]. Recently, we developed an *in vivo* label-free method to measure lymph flow velocity and volumetric flow rates using DOCT [29]. Using this method, we are able to resolve (pulsatile)

lymph flow at a single location within afferent popliteal collecting lymphatic vessels in the mouse hindlimb. We demonstrated two different imaging modes over time: single spatial depth-resolved measurement (M-scan) and cross-sectional imaging (B-scan). The latter has the advantage of providing intraluminal flow velocity profiles, vessel contractile activity by segmentation of the vessel in a series of repeated measurement, and volumetric flow rate by multiplication of the mean velocity with the segmented lumen.

To date, no *in vivo* method has been demonstrated that allows investigation of how lymphangion contractions and lymphatic valves cooperate to drive lymph flow with direct measurements of each of these three parameters. Here, we extend the OCT/DOCT technique to support the simultaneous measurement of flow and contraction in neighboring lymphangions and the status (i.e., open vs closed) of the adjoining valves. In addition, we show that injection of Intralipid can be used to increase the OCT signal within the vessel to improve temporal sampling of the flow velocity. We use this system to measure these parameters in three adjacent lymphangions in a normal mouse and in a model of sterile inflammation. This method will allow the study of the synchrony between lymph flow, valve dynamics and lymphatic contraction to better understand the regulation and dysregulation of lymphatic vessels in health and disease.

Materials & methods

Animal preparation

We used 8 to 16-week-old C3H male mice (26–36 g) for all experiments. Before surgery, mice were anaesthetized using a ketamine/xylazine mixture at 100mg/10mg per kg body weight. The surgical procedure was performed as described previously [30, 31]. Briefly, after hair removal, the skin on the dorsal side of the mouse hindlimb was surgically removed to expose the primary artery/vein pair. The lymphatic vessels run approximately parallel to these blood vessels. Exposed tissue was kept hydrated using physiological saline. After surgery, mice were positioned on a stage tilted 15 degrees with the blood vessel along the maximum slope direction and the body at a higher elevation than the hindlimb. Surgical tape was then used to secure the hindlimb. The 15-degree angle provides a gravity induced opposing pressure as would normally be felt in the hindlimb of an ambulating mouse. The footpad was then injected with 10 μL of Intralipid (Sigma-Aldrich) diluted at either 1:5 or 1:10 with water. We adjusted the dilution to be 1:5 in the normal mouse and 1:10 in the inflammation model experiment to better preserve the contrast between fluid and intraluminal valves. The diluted Intralipid was used to increase the OCT signal within the vessel and improve lymph velocity measurement quality. As described in Liao et al. [30], skin contact sensitization using oxazolone induces sterile cutaneous inflammation which peaks on day 4 and resolves spontaneously by day 7. Therefore, for the oxazolone experiments, four days before imaging, 50 μL of 4% oxazolone (Sigma-Aldrich) in acetone was applied topically to the skin area on the dorsal side of each leg after hair removal. Care was taken to avoid application of oxazalone to skin over the paw. Mice were euthanized at the end of the imaging session. The animal experiment protocol was reviewed and approved by Institutional Animal Care and Use Committee of the Massachusetts General Hospital. The procedures were performed in accordance with the approved guidelines.

DOCT system

The OCT system is similar to that described in prior work [29]. The system uses a swept-wavelength laser source centered at ~1300 nm with an A-scan rate of 50 kHz. The full optical

bandwidth of 100 nm provides an axial resolution of 5.3 μm in tissue. The sensitivity is ~105 dB with 10 mW on the sample. Phase instability, typically present with kinetic swept sources and phase unlocked electronics, is corrected in post-processing by using reference signals from fixed delay reflections [29]. A pair of galvanometer-based optical scanners (Cambridge Technology) steer the beam and define the coordinate system (x,y) together with the optical axis (z).

The beam path through the objective differs in the approach reported here from that described previously [29]. In that prior work, a Doppler angle (between the lymphatic vessel and the imaging beam) was generated by tilting the stage that supported the mouse. Creating the Doppler angle in this manner was adequate for measuring a single spatial point (M-scan) within a vessel or a cross-section (B-scan) orthogonal to its flow direction. However, because of the short depth of focus, this approach fails when measuring at several locations along the vessel. To circumvent this issue, a Doppler angle α is obtained by a shift (Δy) of the beam from the optical axis in the back aperture of the objective (Fig. 1b). The beam was collimated to 2.8 mm, which underfills the pupil plane of the objective lens (LSM02, Thorlabs). A shift of 2.3 mm produces a focused beam departing from the optical axis at 7.3 degrees resulting in a Doppler angle of 82.7 degrees for a vessel lying in the focus plane.

The selection of the imaging Doppler angle is a design trade-off. Smaller values, further from 90 degrees, yield increased accuracy in velocity measurements but require operating further from the objective center axis, which increases aberrations and reduces transverse resolution. The design chosen shows reasonable optical performance over a distance of ±2 mm along the y axis — sufficient to cover the typical length of more than two complete lymphangions at the region of interest— as simulated by a ray tracing program (Zemax). In addition, although a smaller Doppler angle might provide potentially lower velocity accuracy, the current value still allows a correct measurement of event timing (zero crossings, maxima, minima) and therefore the study of the synchronicity between measurement locations.

Imaging procedure

The stage was rotated to align the hindlimb primary artery/vein pair to the y-direction of the galvanometer pair. The lymphatic vessel was identified from real-time OCT B-scan images, with the fast axis scanning direction along x-axis and the slow axis amplitude set to zero along the y-axis. The vessel was centered in the field of view by translation of the stage. Alternating fast and slow axis scanning between y and x allows imaging along the vessel (Fig. 1c), which enables low scattering structures such as fat cells to be distinguished from the lymphatic vessel, as well as identification of intraluminal valves. The rotation of the stage is then adjusted to maximize the length of the lymphatic vessel visible in the field of view. Finally, the stage is translated in the y-direction to a chosen position. During the imaging session, tissue was kept hydrated by topical application of physiological saline.

At the end of each measurement, a volume spanning a 1.4 x 2.1 mm scanning area (464 A-scans per B-scans, 464 B-scans) was acquired. These volumes were analyzed to display the tissue surrounding the measurement locations and to extract the vessel, tissue and air boundaries (Fig. 1c) in order to calculate the vessel Doppler angle at each flow measurement location as previously described [29]. The measured vessel Doppler angle can be different from the set value because of the anatomical position of the vessel within the leg.

DOCT Processing

Standard processing algorithms were used to obtain complex depth-resolved scattering profiles, or A-scans, from raw interferometric fringes as previously described [29, 33]. The data was corrected for tissue bulk motion by manually selecting a region of tissue whose temporal phase evolution was later subtracted from the rest of the dataset. The temporal power spectral density was calculated over every group of 32 repeated B-scans for each spatial pixel. It was then fitted by two constrained circular Gaussians and a white noise background, the first one centered at 0 Hz representing tissue and the second Gaussian shifted from 0 Hz estimating the Doppler frequency shift by its center. Wrapping artifacts, showing pixels of backward velocities within forward flow pulses or vice versa, sometimes appeared during high flow pulses because of the limited frame rate. We have improved our unwrapping methods from our previous approach by examining the temporal evolution of the averaged velocity at each depth within the vessel. Points of forward velocity during backward pulses and vice versa were unwrapped to the corresponding direction. The unwrapped frequency was finally converted to the flow velocity with knowledge of the vessel Doppler angle.

The lymphatic vessel was automatically segmented based on the intensity contrast between lymph and surrounding tissue using a 2D snake algorithm [34] that operates by using the mean of the 32 B-scans. The vessel segmented area was obtained from the surface of the polygon defined by the contour points. The surface measured in the imaging plane is finally rescaled by the cosine of the Doppler angle to obtain the vessel area. All the processing was performed automatically except for the Doppler angle measurement which was manually retrieved from the imaging volume.

Results

4D OCT reveals lymphatic valve dynamics

OCT imaging can resolve intraluminal valves in collecting lymphatic vessels. A valve was measured over five minutes, which corresponds to 1084 volumes, each of 144 A-scans by 96 B-scans, to image its dynamics (Fig. 2, Supplementary Movie 1). Figure 2a-f show cross-sections of the lymphatic vessel at an intraluminal valve. The images on the left in each panel show cross-sections perpendicular to the vessel that clearly show the angular orientation of the valve. On the right, the view along the vessel shows the valve flaps. Valve closing took less than 0.56 seconds and the valve remained closed for about 6 seconds. The valve reopened in less than 0.28 seconds, which is the temporal resolution of this scanning protocol. 3D rendering views extracted from the 4D dataset show the valve in open and closed positions (Fig. 2g-h). 4D datasets of valve closings allow simultaneous lymphatic vessel contractions and valve closings to be observed (Supplementary movie 2).

Intralipid injection increases lymph scattering and allows more rapid measurement of lymph flow

Scattering from lymph is very low, but its OCT signal can still be detected [29]. To enable the measurement of lymph flow using the native lymph signal, long acquisition times are necessary, making it challenging to simultaneously measure lymph flow at multiple locations. We show here that the injection of diluted Intralipid increases the OCT signal strength of the fluid within the lymphatic vessel lumen and enables simultaneous flow measurements using DOCT. Figure 3 shows the scattering intensity of lymph before and after injection of Intralipid. Signal-to-noise ratio (SNR) values were measured as the ratio between the average value of pixels within the vessel

and the average value of noise pixels. Both regions were manually selected. The comparison between pre- and post-injection of Intralipid in 5 mice shows an increase of 7 dB. This contrast enhancement allows an increased precision of the velocity measurement (Fig. 3d) and is sufficient to measure flow at several locations while maintaining enough temporal resolution to resolve flow dynamics at each of these locations. The standard deviation was evaluated at times between flow peaks, when the velocity is almost constant. The standard deviation of 31 μm/s with Intralipid is typical of the precision obtained on the mean velocity at each time point for the results presented in the rest of manuscript. The addition of Intralipid improves the flow velocity peak discrimination. Although the time-average velocity might change after Intralipid injection, the coordination between contractions, valve status and pulsatile flow can still be studied. Importantly, Intralipid at the dilutions used in these experiments preserves the contrast between lymph and valves that is necessary to resolve closing events.

Lymph flow, lymphatic vessel contraction and lymph valve dynamics can be imaged simultaneously across multiple lymphangions

We next performed experiments to demonstrate the feasibility of measuring lymphatic vessel contraction, flow velocity and volumetric flow rate simultaneously within three contiguous lymphangions, from distal to proximal, along with the motion of the two intervening valves (Fig. 4). The stage was moved to a position approximately equidistant to two intraluminal valves, with the lymphatic vessel parallel to the *y*-axis. Repeated B-scans in three successive lymphangions for flow and contraction measurements, as well as 4D data for the two intervening valves are acquired sequentially using their *y* coordinates (Fig. 4a). A smaller Doppler angle reduces the range of the Doppler frequency shifts for a given flow velocity range. As a result, the frame rate could be reduced (compared to our previous work [29]) to capture this smaller frequency shift. This allows for a better lateral spatial sampling at a fixed A-scan rate. In addition, the amount of repetition at each location is a trade-off between sufficient B-scans—for precise measurement of the Doppler frequency shift and the spatial sampling for valve imaging—and sufficient temporal resolution to measure the dynamics of velocity pulses, which typically last for few seconds and occur every 15-20 seconds in healthy mice [29]. We designed the scanning protocol for a five-minute measurement composed of 697 temporal points in total. Each temporal point consists of 32 B-scans at each flow measurement location (constant slow axis signal) and a volume consisting of 64 B-scans spread over a constant length of ~150 μm at each valve location (ramp slow axis signal). The duration of a single time point comprising all of these measurements is 430 ms, which is short compared to the lymphatic flow and contractile dynamics. The measurement over locations is therefore considered to be effectively simultaneous. A ramp waveform with a period of 96 A-scans (~520Hz with the system A-scan frequency) was used to drive the fast axis galvo-scanner.

Figure 4b shows the locations of measurements in an *en face* plane through the lymphatic vessel. The vessel area and the mean cross-sectional velocity within the lymphangions, respectively at the top and bottom of each panel, and the status of the intervening valves are reported in Fig. 4c-g. The vessel area plots show clearly resolved contractions, which are identified by a slow increase of the vessel cross-section followed by a rapid decrease (*e.g.* black arrowhead in Fig. 4c). The curves of mean velocity, calculated as the average velocity over the vessel cross-section, show pulsatile activity. Positive mean flow velocities indicate flow in the proximal direction, while negative mean flow velocities indicate flow in the retrograde direction. The comparison between velocity and cross-sectional area shows that some velocity pulses occur during the contraction

phase while others do not (Fig. 4, continuous and dashed vertical lines, respectively). The volumetric flow rate is calculated by multiplying the instantaneous mean cross-sectional velocity by the vessel cross-section. As expected, the average volumetric flow over the 300 s measurement is similar at the three locations. This is visible by comparing Fig. 4c and Fig. 4g, in which a smaller vessel area corresponds to higher velocity. The comparison of the three locations shows that the velocity pulses are synchronous (Fig. 4, continuous and dashed vertical lines). The velocity curves correlate well and have the same number of pulses (3.2 peaks per minute). The curves plotting cross-sectional area show simultaneous contractions. The number of contractions, quantified manually and defined in a moving averaged curve as an area change from peak to valley larger than 10%, are 1.8, 1.6 and 1.4 contractions per minute for Fig.4 c, e and g respectively.

Valve activity was manually measured from the 4D datasets. In the example in Fig. 4, the more distal valve closed once during the measurement (Fig. 4d, ellipse), when the vessel area was the smallest at all locations, while the proximal valve stayed open during the entire five-minute measurement (Fig. 4f). The closing occurs at the end of a vessel contraction in the distal lymphangion and when the velocity transitions from positive to negative at all locations. During the closing, the velocity maintains its retrograde direction at all locations. The cross-section remains minimum at the distal and proximal location, while it increases in the intermediate lymphangion. When the valve re-opens, the cross-sectional area at the distal and proximal locations increases, and continues to increase at the intermediate location. At the same time, the velocity becomes positive. The increase of the cross-section of the intermediate lymphangion agrees with the negative flow in front of the closed valve. There are multiple other time points in the five-minute dataset when the velocities show a similar profile but the valve did not close.

In our measurements, we observed an initial period of low contractile amplitude and a slow trend of decreasing vessel cross-sectional area. This could be attributable to a combination of the surgery, the between-measurement addition of saline, the transient increase in intraluminal pressure due to the injection of Intralipid or the presence of Intralipid itself.

Lymph flow, contraction and valve dynamics in sterile inflammation

We performed simultaneous measurements of lymph flow and valve dynamics in a mouse after exposure to oxazolone (Fig. 5). The accuracy and precision of the mean velocity and average flow are limited at the distal and intermediate locations in this measurement because of a vessel Doppler angle close to 90 degrees at those locations. To improve the visualization of the data, the velocity measurement (black points) were smoothed with a moving average of four points (solid line). In this example, the lymphatic vessel cross-section shows about 5.8, 6 and 3.4 contractions per minute for Fig. 5 a, c and e respectively, quantified manually and defined in a moving average curve as an area change from peak to valley larger than 10%. The velocity shows an oscillation pattern with forward and back flow, but with a net positive forward average. The mean velocity at the intermediate and proximal locations is similar although the velocity amplitudes at the latter location is larger. The velocity curves are synchronous at the intermediate and proximal locations, but the typical contraction waveform is absent. However, the velocity curves are synchronous with the distal location only after about 130 seconds. The apparent absence of synchronicity during the first 130 seconds could be caused by animal motion which changed the measurement location and thereby the flow direction seen by the optical beam. This could also explain the changes in velocity at the beginning of the measurement. Nonetheless, this measurement shows interesting valve

activity. All seven valve closing events correspond to the crossing from forward to backward velocity, but not all directional flow changes correspond to a closing event. Because of the limited velocity accuracy and precision due to the large Doppler angle, we limit our description to the more proximal valve. When this valve is closing, the magnitude of the backward velocity at the proximal location decreases and becomes zero, with a form similar to a negative exponential (Fig. 5, ellipse). When the valve opens, the flow velocity increases in the proximal direction as fluid moves forward. Valve closings occur at the end of a distal vessel contraction.

Previous work has reported attenuated lymphatic pumping and significantly increased vessel diameters after oxazolone treatment in mice [12, 30]. Using fluorescence microscopy, two phenotypes of lymphatic contraction in the collecting lymphatic vessel leading to the popliteal lymph node were reported four days after oxazolone skin painting. One phenotype showed absent or low contraction frequency. The other showed a higher frequency with a very small amplitude. In the study from Liao *et al.*, the lymphatic contraction frequency after oxazolone skin painting increased from approximately 21 per min in controls to 32 per min on average in young C3H mice in which contractions were detected. We also measured a higher contraction frequency than normal in some oxazolone treated mice (e.g. Figure 5). Interestingly, a small forward flow is still maintained. Figure 6 shows a measurement in another oxazolone treated mouse, this time showing the other phenotype. In this example, the contraction activity is absent and the mean velocity is close to zero. Over all measurements, we see a clear difference in contraction frequencies, both for contraction and velocity, and mean velocity waveform between normal and oxazolone mice. Because of the different concentration of Intralipid used for control and inflamed mice, we cannot exclude that Intralipid had a differential effect on control and inflammation model mice. However, the higher concentration of Intralipid used in control, suggests that alterations caused by inflammation are greater than any effect of Intralipid on diminishing lymphatic vessel function [32].

Discussion

In this study, we developed a novel *in vivo* technique to simultaneously measure lymph flow and lymphatic vessel cross-sectional changes in three successive lymphangions, while also providing 4D imaging of the intervening lymphatic valves. We also demonstrated how Intralipid can be used to increase the OCT signal within the vessel, allowing for better temporal sampling of the flow velocity across multiple locations. In addition to the use of these methods in physiological settings, we demonstrated our technique in a mouse model of sterile inflammation. The difference between the number of contractions, flow peaks and average flow underscores the importance of measuring lymph flow when evaluating lymphatic function. Lymph flow is critical for fluid transport and antigen presentation to the lymph node.

The Intralipid injection, like dye injections in other methods used to measure lymphatic function, might perturb the physiological state of the lymphatic system. First, the injection itself might change the intraluminal pressure and alter the lymphatic function. With a different contrast agent injection, Weiler *et al.* have shown that there is a transient lymphatic pump function response occurring after a bolus injection that can take 5-10 minutes to reach steady state [35]. Second, acute high lipid loads have been shown to reduce lymphatic pump function in the rat mesentery model [32]. We therefore cannot exclude that there is a biological response to low concentrations of lipid introduced with diluted Intralipid. Nonetheless, in this study we sought to develop a

method that can provide the most relevant information about the synchronicity of lymphatic functional parameters (flow, valve dynamics and contractions) in multiple lymphangions. Therefore, we prioritized a better SNR by injecting a contrast agent and consequently were able to acquire nearly simultaneous B-scans in three lymphangions. Alternatively, it would be possible to use a non-lipid based scattering contrast agent to avoid a possible reaction of lymphatic vessels to lipid. Finally, if the interest lies in the study of physiology, a label-free approach, as previously shown [29], could be adopted at a cost of lower temporal resolution or fewer measurement locations.

There are opportunities to further improve the OCT system for this application. The current system provides moderate resolution and imaging speed. Higher resolution would allow a better definition of the valves. The valve tips can be particularly difficult to discriminate on the cross-sectional images. Isotropic sampling would also be advantageous to obtain similar cross-section quality for any valve angular orientation within the vessel. With current 6 μm axial and 11 μm transverse resolutions, the valves are best visualized in the depth-resolved cross-sections (y-z). This is complementary to microscopy where valves are visualized in the *en face* plane [16, 30, 36]. However, with OCT, we benefit from 3D views. Increasing the acquisition speed of the system would allow for a better sampling of the valve structure and the flow velocity profile, which may provide interesting information where two collecting lymphatic vessels conjoin. Alternatively, the temporal sampling could be increased to measure additional locations and prevent any Doppler frequency wrapping. Unwrapping can be a difficult task, especially with abnormal flow patterns that might occur in disease settings. Within the field of view where the optical quality of the beam is maintained, additional valve locations could be added. Using a larger field of view to assess additional locations would require a more complex optical system, such as adaptive focusing, to maintain the optical quality of the beam and the focusing, but might be ultimately limited by the use of a single objective. Our experience also suggests that it could be difficult to extend measurements to additional lymphangions in the mouse hindlimb because of the anatomical variation of these vessels. With our current approach, the lymphangions need to be well aligned and close to the surface. It would also be possible to add flow locations within the field of view if the SNR of the fluid can be maintained. Increasing the Intralipid concentration is technically easy and can be done in experiments dedicated to DOCT flow measurements alone, but for successful 4D valve measurements, the Intralipid concentration should be limited to preserve contrast between intraluminal fluid and valves.

Computational simulations have reproduced a range of behaviors observed in lymphatic vessels *in vivo* and *ex vivo* [4, 12, 37-42], aiding our comprehension of how lymphangions respond to mechanical cues as well as helping form hypotheses on the mechanisms behind lymphangion and valve coordination. Based on our *in vivo* experiments, we confirm that valves are biased-open and that valves may stay continuously open during pumping and retrograde flow, similar to what has been observed *ex vivo* [36]. In addition, we observe simultaneous contractions and flow peaks in the three successive lymphangions. Using Prox1-GFP mice and surgical exposure of the lymphatic vessel in the mouse flank, Chong *et al.*[16] were able to image vessel contraction and valve closing *in vivo*. Their data also show a relation between valve events and vessel cross-sectional changes. Similar to our observations, not every contraction correlated with a valve closing. Further studies are needed to fully understand the synchronicity of valve function. Under our experimental conditions, valve closure is a rare event. It was seen in 2 of 6 healthy mice, and in only 4 out of

about 55 five-minute valve measurements. In oxazolone treated mice, we observed valve closings in 1 of 6 mice and only in 2 out of 48 five-minute valve measurements.

Previous in vivo studies have reported changes to lymphatic vessel contraction frequency and amplitude after oxazolone induced inflammation, as well as a less common phenotype with highly dilated vessels and little vasomotion [12, 30]. While NO and Ca2+ influences on lymphatic vessel contraction have been extensively described in both physiology and pathophysiology, the complete mechanisms have not yet been unraveled. For example, little is known about endothelial mechanobiology and how shear stress signals are transduced [1].

The observation of open biased valves *in vivo* is an important element for numerical simulations as it narrows down possible scenarios. Valves stay open, possibly as a mechanism to minimize any impediment to flow in a chain of lymphangions [4]. The measurement of contractions could be performed on a larger number of animals to investigate the synchronization of contractions in detail. The current data suggest that they are synchronous to the eye or quasi-synchronous but do not exclude an occasional phase shift between successive lymphangions. This would be an important *in vivo* observation as it would help rule out possible explanations of local regulatory mechanisms [4]. Our method allows the *in vivo* study of physiology and pathology, including changes to lymphatic collecting vessels in the cancer (pre-)metastatic settings, after radiation therapy, after surgical interventions, and after *in vivo* gene knockdown (i.e. primary lymphedema and ion channel studies) as well as during therapeutic interventions.

Acknowledgements
Research reported in this publication was supported in part by the Center for Biomedical OCT Research and Translation through Grant Number P41EB015903, awarded by the National Institute of Biomedical Imaging and Bioengineering of the National Institutes of Health, by the National Institutes of Health under award numbers R01CA163528 (B.J.V.), DP2OD008780 (T.P.P.), R21AI097745 (T.P.P.) and R01HL128168 (T.P.P.). The National Cancer Institute Federal Share of Proton Income also supported this work (T.P.P., B.J.V.). Cedric Blatter was supported by a Swiss National Science Foundation early post-doctoral mobility fellowship (P2SKP2_158640). The authors acknowledge Lance L. Munn for the drawing of Figure 1a.

References

1. Padera, T.P., E.F. Meijer, and L.L. Munn, The Lymphatic System in Disease Processes and Cancer Progression. Annu Rev Biomed Eng, 2016.
2. Schmid-Schonbein, G.W., Microlymphatics and lymph flow. Physiol Rev, 1990. 70(4): p. 987-1028.
3. Zawieja, D.C., Contractile physiology of lymphatics. Lymphat Res Biol, 2009. 7(2): p. 87-96.
4. Bertram, C.D., et al., Consequences of intravascular lymphatic valve properties: a study of contraction timing in a multi-lymphangion model. Am J Physiol Heart Circ Physiol, 2016. 310(7): p. H847-60.
5. Mortimer, P.S. and S.G. Rockson, New developments in clinical aspects of lymphatic disease. J Clin Invest, 2014. 124(3): p. 915-21.
6. Brandon Dixon, J. and M.J. Weiler, Bridging the divide between pathogenesis and detection in lymphedema. Semin Cell Dev Biol, 2015. 38: p. 75-82.

7. Rasmussen, J.C., et al., The role of lymphatics in cancer as assessed by near-infrared fluorescence imaging. Ann Biomed Eng, 2012. 40(2): p. 408-21.
8. Liu, N. and Y. Zhang, Magnetic Resonance Lymphangiography for the Study of Lymphatic System in Lymphedema. J Reconstr Microsurg, 2014.
9. Iimura, T., et al., Estimating Lymphodynamic Conditions and Lymphovenous Anastomosis Efficacy Using (99m)Tc-phytate Lymphoscintigraphy with SPECT-CT in Patients with Lower-limb Lymphedema. Plast Reconstr Surg Glob Open, 2015. 3(5): p. e404.
10. Gashev, A.A., et al., Regional variations of contractile activity in isolated rat lymphatics. Microcirculation, 2004. 11(6): p. 477-92.
11. Scallan, J.P. and M.J. Davis, Genetic removal of basal nitric oxide enhances contractile activity in isolated murine collecting lymphatic vessels. J Physiol, 2013. 591(Pt 8): p. 2139-56.
12. Kunert, C., et al., Mechanobiological oscillators control lymph flow. Proc Natl Acad Sci U S A, 2015. 112(35): p. 10938-43.
13. Kwon, S. and E.M. Sevick-Muraca, Effect of lidocaine with and without epinephrine on lymphatic contractile activity in mice in vivo. J Anesth, 2016. 30(6): p. 1091-1094.
14. Proulx, S.T., et al., Quantitative imaging of lymphatic function with liposomal indocyanine green. Cancer Res, 2010. 70(18): p. 7053-62.
15. Guo, R., et al., Inhibition of lymphangiogenesis and lymphatic drainage via vascular endothelial growth factor receptor 3 blockade increases the severity of inflammation in a mouse model of chronic inflammatory arthritis. Arthritis Rheum, 2009. 60(9): p. 2666-76.
16. Chong, C., et al., In vivo visualization and quantification of collecting lymphatic vessel contractility using near-infrared imaging. Sci Rep, 2016. 6: p. 22930.
17. McLaughlin, R.A., et al., Imaging of human lymph nodes using optical coherence tomography: potential for staging cancer. Cancer Res, 2010. 70(7): p. 2579-84.
18. Luo, W., et al., Optical biopsy of lymph node morphology using optical coherence tomography. Technol Cancer Res Treat, 2005. 4(5): p. 539-48.
19. John, R., et al., Three-dimensional optical coherence tomography for optical biopsy of lymph nodes and assessment of metastatic disease. Ann Surg Oncol, 2013. 20(11): p. 3685-93.
20. Nguyen, F.T., et al., Optical coherence tomography: the intraoperative assessment of lymph nodes in breast cancer. IEEE Eng Med Biol Mag, 2010. 29(2): p. 63-70.
21. Qin, W., U. Baran, and R. Wang, Lymphatic response to depilation-induced inflammation in mouse ear assessed with label-free optical lymphangiography. Lasers Surg Med, 2015. 47(8): p. 669-76.
22. Yousefi, S., et al., Label-free optical lymphangiography: development of an automatic segmentation method applied to optical coherence tomography to visualize lymphatic vessels using Hessian filters. Journal of Biomedical Optics, 2013. 18: p. 86004-86004.
23. Zhi, Z., Y. Jung, and R.K. Wang, Label-free 3D imaging of microstructure, blood, and lymphatic vessels within tissue beds in vivo. Opt Lett, 2012. 37(5): p. 812-4.
24. Jung, Y., Z. Zhi, and R.K. Wang, Three-dimensional optical imaging of microvascular networks within intact lymph node in vivo. J Biomed Opt, 2010. 15(5): p. 050501.
25. Vakoc, B.J., et al., Three-dimensional microscopy of the tumor microenvironment in vivo using optical frequency domain imaging. Nat Med, 2009. 15(10): p. 1219-23.

26. Baran, U., et al., OCT-based label-free in vivo lymphangiography within human skin and areola. Sci Rep, 2016. 6: p. 21122.
27. Gong, P., et al., In vivo label-free lymphangiography of cutaneous lymphatic vessels in human burn scars using optical coherence tomography. Biomedical Optics Express, 2016. 7(12): p. 4886-4898.
28. Leitgeb, R.A., et al., Doppler optical coherence tomography. Prog Retin Eye Res, 2014. 41: p. 26-43.
29. Blatter, C., et al., In vivo label-free measurement of lymph flow velocity and volumetric flow rates using Doppler optical coherence tomography. Sci Rep, 2016. 6: p. 29035.
30. Liao, S., et al., Impaired lymphatic contraction associated with immunosuppression. Proc Natl Acad Sci U S A, 2011. 108(46): p. 18784-9.
31. Liao, S., et al., Method for the quantitative measurement of collecting lymphatic vessel contraction in mice. J Biol Methods, 2014. 1(2).
32. Bouma, B.E., et al., Fourier-domain optical coherence tomography: recent advances toward clinical utility. Curr Opin Biotechnol, 2009. 20(1): p. 111-8.
33. Kass, M., A. Witkin, and D. Terzopoulos, Snakes: Active contour models. International Journal of Computer Vision, 1988. 1(4): p. 321-331.
34. Kassis, T., et al., Postprandial lymphatic pump function after a high-fat meal: a characterization of contractility, flow, and viscosity. Am J Physiol Gastrointest Liver Physiol, 2016. 310(10): p. G776-89.
35. Weiler, M. and J.B. Dixon, Differential transport function of lymphatic vessels in the rat tail model and the long-term effects of Indocyanine Green as assessed with near-infrared imaging. Front Physiol, 2013. 4: p. 215.
36. Davis, M.J., et al., Determinants of valve gating in collecting lymphatic vessels from rat mesentery. American Journal of Physiology - Heart and Circulatory Physiology, 2011. 301(1): p. H48-H60.
37. Rahbar, E. and J.E. Moore, Jr., A model of a radially expanding and contracting lymphangion. J Biomech, 2011. 44(6): p. 1001-7.
38. Wilson, J.T., et al., Confocal image-based computational modeling of nitric oxide transport in a rat mesenteric lymphatic vessel. J Biomech Eng, 2013. 135(5): p. 51005.
39. Wilson, J.T., et al., Determining the combined effect of the lymphatic valve leaflets and sinus on resistance to forward flow. J Biomech, 2015. 48(13): p. 3584-90.
40. Jamalian, S., et al., Network Scale Modeling of Lymph Transport and Its Effective Pumping Parameters. PLoS One, 2016. 11(2): p. e0148384.
41. Bertram, C.D., C. Macaskill, and J.E. Moore, Jr., Pump function curve shape for a model lymphatic vessel. Med Eng Phys, 2016. 38(7): p. 656-63.
42. Baish, J.W., et al., Synchronization and Random Triggering of Lymphatic Vessel Contractions. PLoS Comput Biol, 2016. 12(12): p. e1005231.

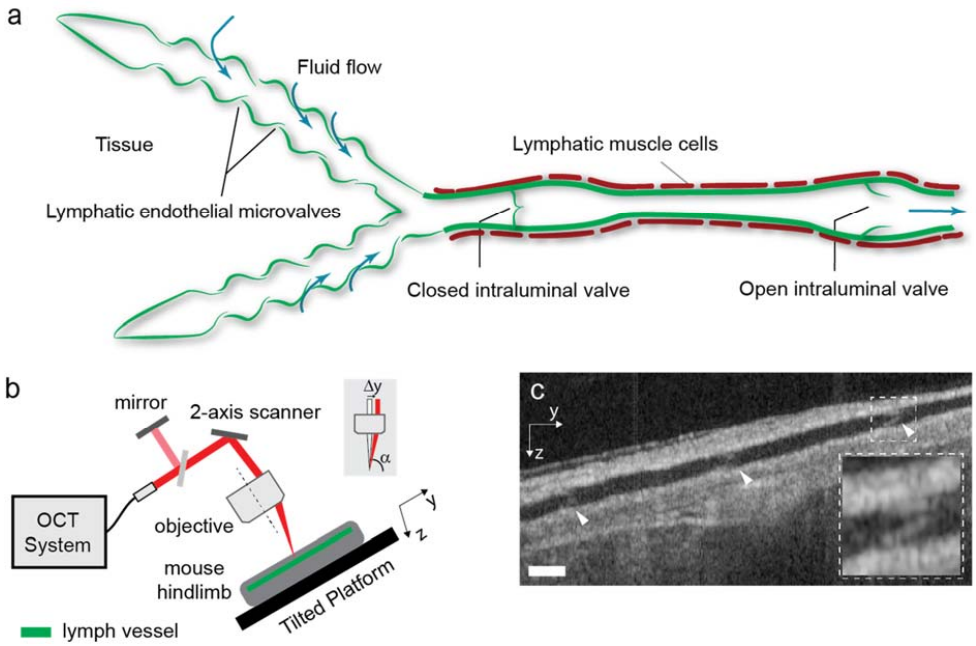

Figure 1. Lymphatic imaging and flow measurement using Doppler OCT. (a) Anatomy of initial and collecting lymphatic vessels and valve function. Initial lymphatic vessels on the left collect interstitial fluid to create lymph, which is carried to a lymph node by a collecting lymphatic vessel. Lymphatic muscle cells can contract to drive flow, while intraluminal valves can close to prevent net backflow. The vessel segment between two valves is called a lymphangion. The figure is adapted with permission from Padera *et al.* [1]. (b) Schematic of the imaging setup. The light path is displayed in red. A portion of the collimated light is reflected to a mirror providing a reference signal for phase instabilities correction. A 2-axis galvanometer-based optical scanner is used to steer the beam. The beam shift (Δy) provides the Doppler angle α. The mouse is positioned with the lymphatic vessel along the y axis on a tilted platform with an angle of 15 degrees to provide a gravity induced opposing pressure gradient to lymph flow. The optical system has similar tilt to the tilted platform. (c) A cross-sectional image along the lymphatic vessel extracted from the volume data and used to calculate the Doppler angle at each flow location. Arrowheads point to intraluminal valves. Dashed region shows a close-up of a valve. Depending on their angular orientation within the vessel, the valves are better visualized in the cross-section or in the *en face* plane (Fig. 4b). Scale bars denote 130 µm.

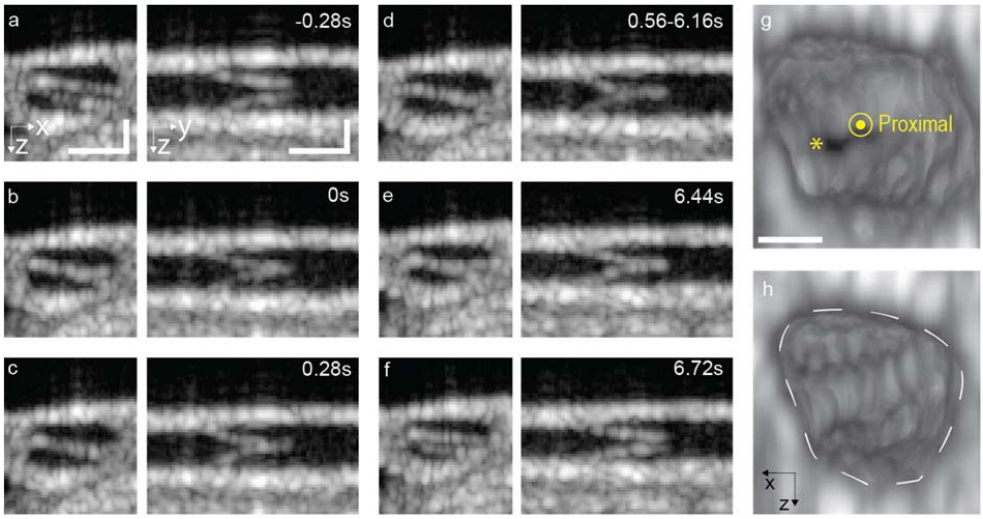

Figure 2 4D imaging of valve dynamics. (a-f) Cross-sectional images perpendicular to and along the lymphatic vessel, on the left and right respectively. (c) An image was extracted from the 4D dataset at a time point when the valve is open. Time points of valve flaps (d) touching, (e) stronger contact, (f) valve closed, (g) valve initiating reopening and (h) opened. Scale bar denote 50 µm. The motion can be appreciated in Supplementary Movie 1. (g) and (h) 3D rendering of views extracted from the 4D dataset at a time when the valve is open (*) and closed, respectively. The proximal side of the valve is shown. The white dashed line highlights the contour of the vessel. Scale bar denotes 25 µm.

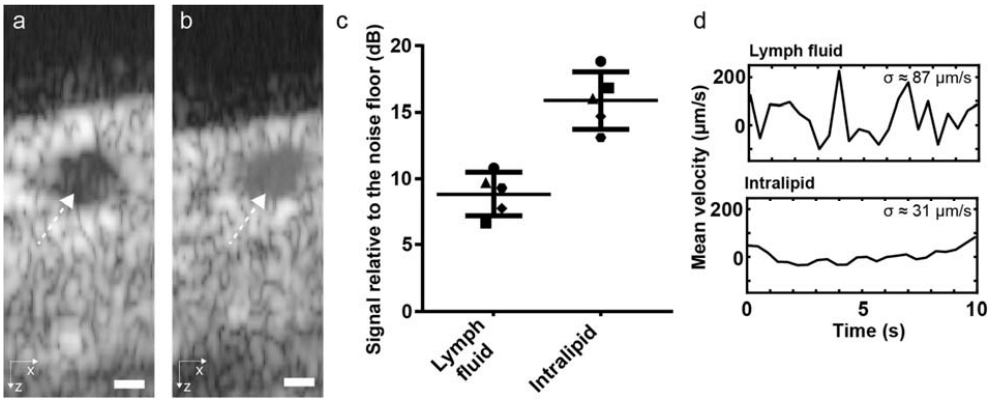

Figure 3 Increase of the OCT signal within a lymphatic vessel after Intralipid injection. Averaged frame from the 32 repeated B-Scans at one location (a) before and (b) after the injection of Intralipid. The white dashed arrows point to the lymphatic vessel lumen. (c) The measured ratio between signal within the vessel and noise floor before and after injection across five animals shows an average SNR increase of 7 dB. (d) Doppler flow velocity curves acquired before and after injection of Intralipid show that the increased SNR improves measurement quality.

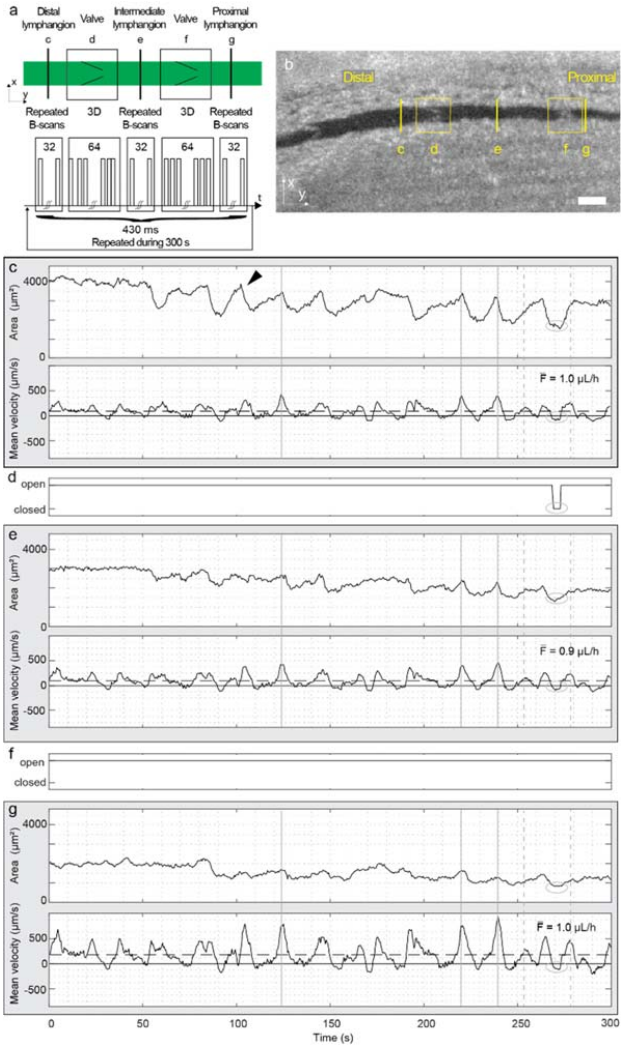

Figure 4 Simultaneous flow measurements in three successive lymphangions and intervening valve dynamics in a normal mouse. (a) Schematic representation of the scanning pattern and timing for the simultaneous imaging at five locations. The five locations are imaged sequentially but considered simultaneous because of the short cycle duration (430 ms) compared to the flow and contractile dynamics at the imaging site. The cycle is repeated 697 times during 300 s. (b) *En face* plane crossing the lymphatic vessel extracted from the structural volume acquired with each dataset. The yellow lines highlight the anatomical locations of measurements c to g. Panels (c), (e) and (g) show measurements of the vessel cross-sectional area (top) and mean velocity (bottom) within three lymphangions: (c) distal, (e) intermediate and (g) proximal. Arrowhead indicates an example of the beginning of a contraction. Continuous and dashed horizontal lines in the velocity plots indicate the zero and the average velocity, respectively. The average volumetric flow $\overline{F}$ over the five-minute duration is displayed. Vertical continuous and dashed gray lines are visual aids for a flow velocity pulse respectively synchronous or asynchronous to a contraction. (d) and (f) Status of the intervening valves are manually extracted from the 4D dataset. The ellipse highlights the period of the closed valve on the velocity and cross-sectional area waveforms.

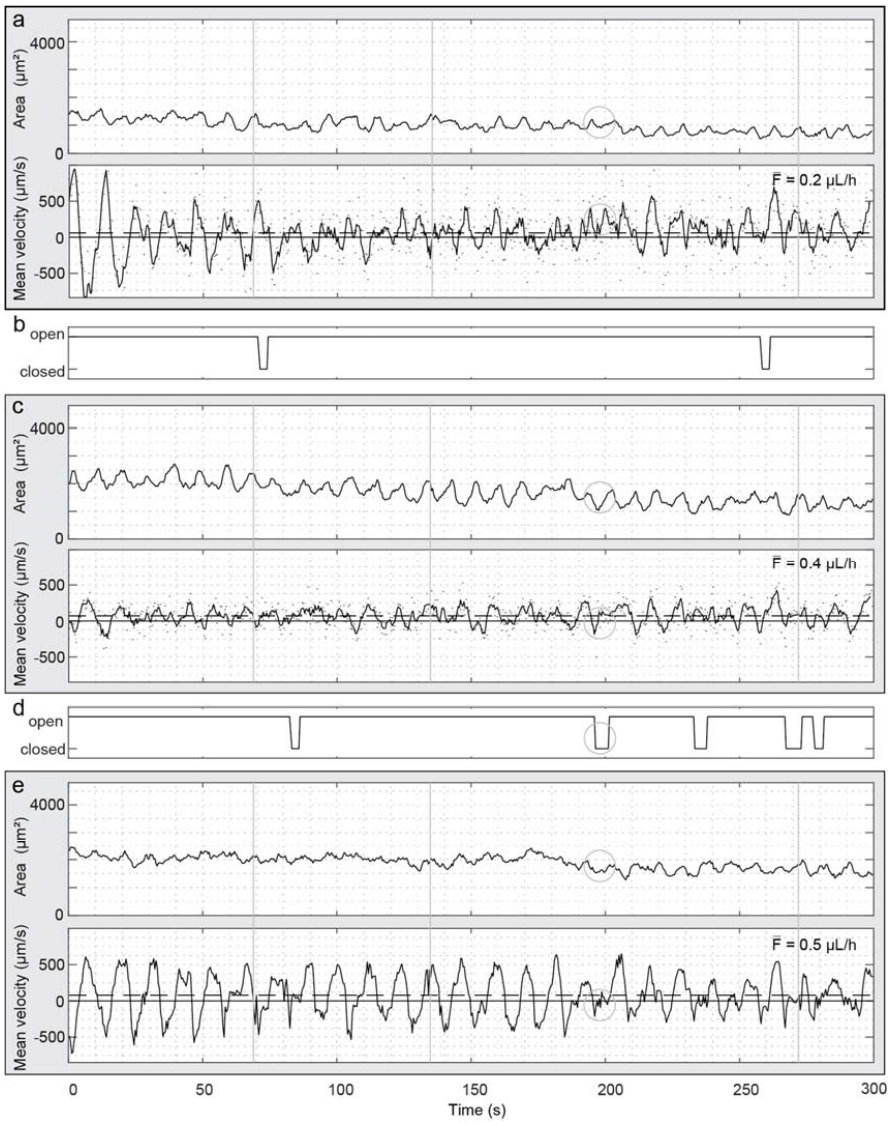

Figure 5 Simultaneous flow measurement in three successive lymphangions and intervening valve dynamics imaging in a sterile inflammation model in a mouse. Panels (a), (c) and (e) show measurements of vessel cross-section area (top) and mean velocity (bottom) within three lymphangions: (a) distal, (c) intermediate and (e) proximal. The velocity measurements (black points) at the distal and intermediate locations were smoothed using a moving average of 4 points (solid line). The lower accuracy and precision of velocity and average flow is the result of a Doppler angle close to 90 degrees at these locations. Continuous and dashed horizontal lines in the velocity plots indicate the zero and the average velocity respectively. The average volumetric flow $\bar{F}$ over the five-minute duration is displayed. Vertical gray lines are visual aids for synchronous contractions. (b) and (d) Status of the intervening valves manually extracted from the 4D dataset. The ellipse highlights the period of the closed valve on the velocity and cross-sectional area waveforms.

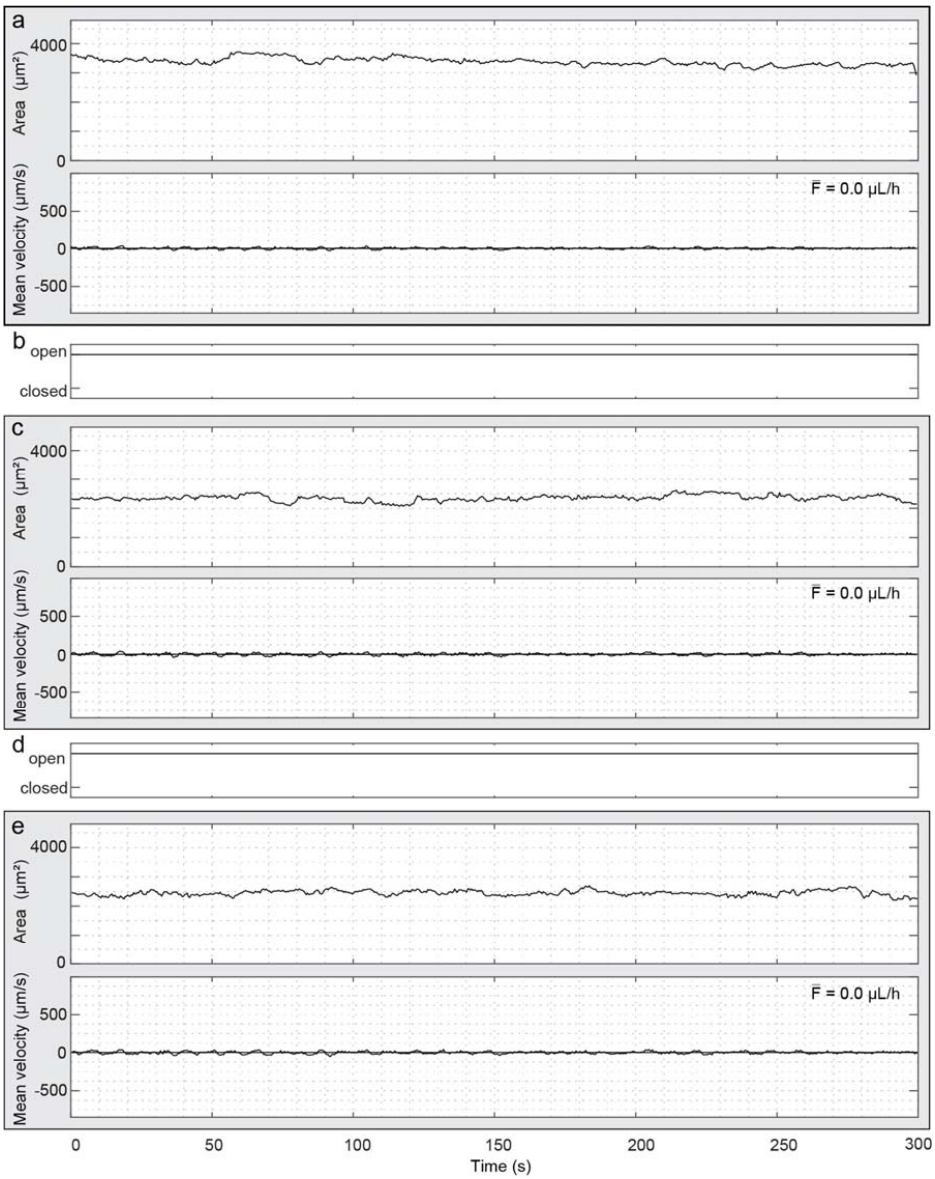

Figure 6 Simultaneous flow measurement in three successive lymphangions and intervening valve dynamics imaging in a mouse model of inflammation. Panels (a), (c) and (e) show measurements of vessel cross-section area at the top and mean velocity at the bottom within three lymphangions: (a) distal, (c) intermediate and (e) proximal. Continuous and dashed horizontal lines in the velocity plots indicate the zero and the average velocity respectively. The average volumetric flow $\bar{F}$ over the five-minute duration is displayed. (b) and (d) Status of the intervening valves manually extracted from the 4D dataset.

Part II: Imaging studies

6. Lymph node effective vascular permeability and chemotherapy uptake

Eelco FJ Meijer[1, 3], Cedric Blatter[2, 3], Ivy X Chen[1, 3], Echoe Bouta[1, 3], Dennis Jones[1, 3], Ethel R Pereira[1, 3], Keehoon Jung[1, 3], Benjamin J. Vakoc[2,3], James W Baish[4], Timothy P Padera[1, 3, *]

[1]Edwin L. Steele Laboratories for Tumor Biology, Department of Radiation Oncology, Massachusetts General Hospital Cancer Center, Boston, Massachusetts 02114, USA. [2]Wellman Center for Photomedicine, Massachusetts General Hospital, Boston, Massachusetts 02114, USA. [3]Harvard Medical School, Boston, Massachusetts 02115, USA. [4]Department of Biomedical Engineering, Bucknell University, Lewisburg, PA 17837, USA. *To whom correspondence should be addressed: Timothy P. Padera (tpadera@steele.mgh.harvard.edu)

Microcirculation. 2017;00:1–8.
Supporting information available online.

Abstract

Objective: Lymph node metastases are a poor prognostic factor. Additionally, responses of lymph node metastasis to therapy can be different from the primary tumor. Investigating the physiologic lymph node blood vasculature might give insight into the ability of systemic drugs to penetrate the lymph node, and thus into the differential effect of therapy between lymph node metastasis and primary tumors. Here, we measured effective vascular permeability of lymph node blood vessels and attempted to increase chemotherapy penetration by increasing effective vascular permeability.

Methods: We developed a novel three-dimensional method to measure effective vascular permeability in murine lymph nodes *in vivo*. VEGF-A was systemically administered to increase effective vascular permeability. Validated high-performance liquid chromatography protocols were used to measure chemotherapeutic drug concentrations in untreated and VEGF-A treated lymph nodes, liver, spleen, brain and blood.

Results: VEGF-A treated lymph node blood vessel effective vascular permeability (mean 3.83×10^{-7} cm/s) was significantly higher than untreated lymph nodes (mean 9.87×10^{-8} cm/s). No difference was found in lymph node drug accumulation in untreated versus VEGF-A treated mice.

Conclusions: Lymph node effective vascular permeability can be increased (~4-fold) by VEGF-A. However, no significant increase in chemotherapy uptake was measured by pre-treatment with VEGF-A.

Abbreviations: 2D, Two-dimensional; 3D, Three-dimensional; 5-FU, 5-fluorouracil; DAPI, 4′,6-diamidino-2-phenylindole; EDTA, Ethylenediamine tetraacetic acid; EVP, Effective vascular permeability; FITC-BSA, Fluorescein isothiocyanate conjugated to bovine serum albumin; HIV, Human immunodeficiency virus; HPLC, High-performance liquid chromatography; HRH1, Histamine H1 receptor; HSA, Human serum albumin; LN, Lymph node; MECA-32, Mouse endothelial cell antigen-32; PBS, Phosphate buffered saline; ROI, region of interest; SCID, severe combined immunodeficiency; SEM, Standard error of mean; SIV, Simian immunodeficiency virus; VEGF-A, Vascular endothelial growth factor A.

Introduction

Solid tumors often metastasize to regional lymph nodes. This metastatic spread is a poor prognostic factor, regardless of the site of the primary tumor [1]. Systemic therapies are usually designed to treat the primary tumor, but it is known that the local tumor microenvironment alters the phenotypic behavior of cancer cells, including response to therapy [2-3]. Thus, therapies designed to treat primary tumors often are less efficacious in treating metastasis in their new microenvironment[4-5]. Because some patients show complete or partial responses in metastatic lymph nodes during chemotherapy [6], it is assumed that these drugs are able to penetrate lymph nodes. However, disease recurrence in the lymph nodes of patients initially diagnosed without nodal metastasis or with nodal micrometastases is also common, suggesting systemic therapy does not eradicate these small pockets of cells. One difference between the macro- and micrometastatic settings is the ability of the tumor to alter the vasculature of the lymph node [7]. Investigation of the physiologic lymph node blood vasculature might therefore explain why systemic (intravenous) therapy fails to eradicate micrometastatic disease, which is when lymph node disease burden is lower and thus thought to be easier to treat. Systematic studies of chemotherapy drug penetration into lymph nodes—both under normal and disease conditions—could offer a better understanding of why there is a differential response of lymph node metastasis and primary tumors to therapy.

Published studies have looked at lymphoid tissue drug penetration in the context of HIV, as spleen, lymph nodes, and gut-associated lymphoid tissues have been identified as pharmacologic sanctuaries from anti-retroviral therapy[8-9]. Also in HIV patients, there is evidence that drug penetration into the lymph node is insufficient [10-12]. This likely contributes to HIV infected T cells finding pharmacologic sanctuary in lymph nodes, which are then able to expand and repopulate the patient with infected cells after treatment is stopped [10, 13]. Based on these data, we hypothesized that micrometastases and isolated metastatic cancer cells might similarly find pharmacologic sanctuary from chemotherapy. Employing validated methods to measure tissue drug concentrations, as well as our novel method to measure EVP in three dimensions [14], we investigated whether low lymph node blood vessel EVP could play a role in the establishment of pharmacologic sanctuary sites for metastatic cancer cells and whether enhancing blood vessel EVP using VEGF-A [15-17] could improve drug delivery. EVP accounts for convective, oncotic and diffusive transport of a molecular solute across the endothelium [14]. Developing a fundamental knowledge of EVP and drug penetration in lymph nodes will greatly contribute to the understanding of lymph node (patho-) physiology and allow for improvement in the treatment of cancer patients with lymph node metastasis.

Materials & methods

Mice

All mice were bred and kept in a gnotobiotic animal facility. Approval by the Massachusetts General Hospital Institutional Animal Care and Use Committee was obtained for all experiments. We used 8 to 14-week-old BALB/c male mice (26g-34g). The immunocompetent BALB/c strain was selected for lacking melanin, which can build up in the lymph node over time and cause auto-fluorescence in pigmented mouse strains (Supporting Figure 1). This auto-fluorescence may interfere with accurate vessel masking for EVP measurements as described below.

Measuring effective vascular permeability using multiphoton microscopy

We performed EVP measurements using multiphoton microscopy [14] on normal lymph node and dorsal skinfold vasculature in twenty-five BALB/c mice. Surgical implantation of the chronic lymph node window and dorsal skinfold chamber was performed under general anesthesia (100/10mg ketamine/xylazine mixture per kg body weight) as previously described [18-20]. These chronic window models allow for nearly motionless intravital imaging. Two days after surgical implantation, the mouse was positioned on an imaging stage and a cannula was inserted into the tail vein for intravenous access. Thirty seconds after intravenous injection in the tail vein of 100µL of a 1% solution of FITC-BSA (Sigma-Aldrich, A9771), imaging was performed using a custom-built multiphoton laser-scanning microscope (adapted from Olympus 300; Optical Analysis Corp.) with a broadband femtosecond laser source (High Performance MaiTai, Spectra-Physics). Slowest acquisition (~0.85 sec per slice) on Olympus FluoView software was employed to get best quality images containing 256 × 256 pixels (~482.65 µm x 482.65 µm). Seventy-four *z*-slices starting ~15-20 µm below tissue surface with steps of 1.84 µm were obtained with a 25× 1.05NA water-immersion objective at 1.5× digital zoom (Figure 1). Image slices were acquired with ~60mW on sample laser power at 780nm wavelength. For signal detection, we used a 535DF43 emission filter in front of the photomultiplier tube. Using these settings, there is no photobleaching or saturation of the FITC-BSA fluorophore. For each EVP measurement, 8 time-lapse image stacks were obtained over a ~16-minute timespan. Vessel masking was performed using ImageJ[21] 1.47v image analysis software (NIH): the image stack was converted to binary using the threshold method "Li" followed by a 3D median filter (radius 1 pixel) to remove background single voxel noise. Custom analysis software written in Matlab version r2013a (available in Supporting Information) is used to calculate the EVP after vessel masking, which is based on the first stack of image slices acquired 30 seconds after FITC-BSA injection. This vessel mask then allows identification of signal intensity changes inside and outside the vessels over time in all stacks of image slices using a 3D box-shaped ROI approach containing multiple vessels as recently described [14]. In short, this box-shaped ROI approach segments the voxels in a data stack into those inside the vessel, those on the vessel wall or those outside the vessel using the vessel masking. For calculating EVP, all vessels combined are mathematically considered as a single vessel. EVP (cm/s) is calculated as $EVP = \frac{(\text{voxel size}) * \text{Slope of Fe over time}}{(n_{wall}) * \text{Mean of } (Fv - Fi)}$ where *voxel size* is the size of a voxel (*i.e.* 1.84×10^{-6} cm^3), *Fe* is total fluorescence from all exterior points including those on the wall, n_{wall} is the number of voxels making up the vessel walls, *Fv* is the mean fluorescence from the voxels inside the vessel and *Fi* is the mean fluorescence of the vessel wall voxels.

For VEGF-A treatment, 8 mg/kg recombinant mouse VEGF-A 164 Protein (R&D Systems, #493-MV-005) in 50 µL of sterile PBS was administered retro-orbitally 2 hours before imaging. For histamine treatment, histamine dihydrochloride 12.5 mg/kg (R&D systems, #3545/50) in 50µL of

sterile PBS was administered intravenously together with FITC-BSA. All mice were euthanized after imaging.

High-performance liquid chromatography

For HPLC, a total of sixty-four 8 to 16-week-old BALB/c male mice (4 mice per drug per time point) were treated with 50 mg/kg 5-FU (Sigma F6627), 20 mg/kg paclitaxel (ChemieTek, CT-0502), 20 mg/kg cisplatin (Selleckchem, S1166) or 10 mg/kg doxorubicin (Selleckchem, S1208). For the timepoint evaluation, an additional 24 BALB/c mice were used (2 mice per drug per time point, available in the supporting information). At 10 minutes, 2 hours, 4 hours, 8 hours and 24 hours, mouse whole blood was collected in an EDTA tube using cardiac puncture and snap-frozen in liquid nitrogen. The liver, spleen, brain and lymph nodes were snap-frozen in cryovials for subsequent analysis. The mandibular, cranial deep cervical, proper axillary, accessory axillary, subiliac, popliteal, jejunal, colic and medial iliac lymph nodes [22] were collected and grouped per animal. Up to 200mg of organ tissues were separately weighed and homogenized in 1 mL CelLytic™ tissue lysis buffer (Sigma-Aldrich C3228) on ice for at least 1 minute until complete decomposition of the bulk tissue. 500 µL of cold methanol was added to 500 µL of the homogenate, vortexed, and then centrifuged at 12,000 rpm for 10 minutes (5415D Microcentrifuge, Eppendorf). The supernatant was collected and the pellet discarded. In addition, 5-FU and doxorubicin were extracted with 5 mL ethyl acetate, vortexed for 1 min, and centrifuged for 10 minutes. The organic layer was collected and evaporated to dryness using Genevac EZ-2 (SP Scientific). The dry pellet was reconstituted with 500 µL of deionized water. To measure the concentration of drugs in the homogenate sample, 500 µL of the supernatant solution (for paclitaxel and cisplatin) or deionized water (for 5-FU and doxorubicin) was filtered through a 0.22 µm centrifuge filter (Sigma-Aldrich, CLS8161). The solution was then transferred into an HPLC vial and analyzed by HPLC (Atlantics dC18 column, 250 mm x 4.6 mm, i.d. 5 µm).

Immunohistochemistry

For visualization of histamine receptor on the vascular endothelium of the lymph node, we used goat anti-mouse HRH1 antibody (Santa Cruz, sc-20633, 1:50) and rat anti-mouse MECA-32 (BD, 553849, 1:100) on paraffin-embedded BALB/c lymph node tissue sections (5µm thickness). Donkey anti-mouse IgM-488 and IgM-cy3 were used as secondary antibodies (1:250) for HRH1 and MECA-32, respectively.

Statistics

Graphpad Prism v7.02 was used for all statistical analyses. For comparisons between two groups, an unpaired nonparametric Mann-Whitney t-test was performed. For analysis of multiple groups, a Kruskal-Wallis ANOVA was performed with Dunn's multiple comparisons test. Results are presented as Mean ± SEM.

Results

Effective vascular permeability in lymph nodes

Using our methods, we measured a mean EVP (Figure 1) in normal lymph node blood vessels of $9.9 \pm 1.5 \times 10^{-8}$ cm/s (n=7) in BALB/c mice. We found that normal lymph node blood vessel EVP was not significantly different compared to untreated subcutaneous blood vessels. Next, we evaluated whether lymph node EVP could be increased by using murine histamine (12.5 mg/kg) and VEGF-A (8 mg/kg), as both have been shown to cause rapid increases in vascular permeability [23-24]. We verified the presence of HRH1 on lymph node blood vessel endothelium (Supporting

Figure 2). Dunn's multiple comparisons test demonstrated that the EVP of lymph nodes treated with histamine (n=5, $4.1 \pm 0.9 \times 10^{-7}$ cm/s) and VEGF-A (n=8, $3.8 \pm 0.7 \times 10^{-7}$ cm/s) was significantly greater than untreated lymph nodes (Figure 1). Using these doses, we showed that blood vessel EVP can be increased ~4-fold in lymph nodes.

Chemotherapy penetration in untreated and VEGF-A treated lymph nodes

Next, we tested whether an increase in lymph node EVP could lead to an increased accumulation of chemotherapeutic drugs. We selected commonly used chemotherapeutic drugs from different classes and with variable drug properties (Table 1) and compared drug accumulation in untreated and VEGF-A treated mice 2 hours and 4 hours (n=4 per group) after a single chemotherapeutic drug injection (Figure 2). HPLC drug calibration curves showed good correlation to drug standards (R^2 >0.99, Supporting Figure 3) and there was no false positive signal in untreated tissue for any of the drugs. Timepoints were chosen based on the maximum lymph node drug concentration of 5-FU and paclitaxel (Supporting Figure 4). The absence of signal for 5-FU and paclitaxel in tissues and blood in uninjected animals are shown in Supporting Figure 4. Cisplatin and doxorubicin levels were also not detectable in uninjected animals (not shown). On average per mouse, 962 µL, 35 mg, 1269 mg, 96 mg and 440 mg of blood, lymph node, liver, spleen and brain tissue was harvested, respectively. Dunn's multiple comparisons test was performed for all comparisons. There were no significant differences in drug concentration in the brains of animals treated with VEGF-A relative to control, and as expected all values were low compared to blood. Mean blood cisplatin concentrations were significantly lower after 2 hours in VEGF-A treated animals compared to control. Spleen and liver showed no significant changes with VEGF-A treatment. In lymph nodes, doxorubicin had the highest drug concentration, despite having the lowest injected dose at 10 mg/kg. For all drugs, no significant difference in lymph node drug concentration was observed after administration of VEGF-A. When comparing untreated lymph node to liver at 2h and 4h using an unpaired t-test, 5-FU and paclitaxel concentrations were significantly lower in lymph node at 4h. Surprisingly, increasing EVP by administering VEGF-A did not increase maximum lymph node drug penetration.

Discussion

The efficacy of chemotherapy on isolated metastatic cancer cells or micrometastases in the lymph node may depend on the ability of chemotherapeutic drugs to reach its target in therapeutic concentrations. Therefore, we tested whether maximum chemotherapeutic drug concentrations could be increased in lymph nodes by increasing blood vessel EVP. We found that blood vessel EVP can be increased in lymph nodes by administering VEGF-A systemically. However, this did not increase maximum drug concentrations in any organ tested.

We first analyzed the EVP in normal, untreated blood vessels in lymph nodes and in the dorsal skinfold chamber in BALB/c mice. The latter was performed to compare blood vessel EVP measurements made using our novel 3D method, to published measurements of FITC-BSA EVP in the same dorsal skinfold chamber surgical preparation using a 2D method[14] (Table 2). Normal subcutaneous blood vessels using this 2D method were found to have an EVP around 5.0×10^{-8} cm/s and 7.5×10^{-8} cm/s in SCID and C57BL/6 mice, respectively[25-26]. EVP measured in SCID mouse normal pancreas[27] and brain[25] were found to be similar to SCID subcutaneous blood vessels (~5.0×10^{-8} cm/s), while normal liver blood vessel EVP was lower (2.7×10^{-8} cm/s) [28]. Our EVP measurements using a 3D approach in immunocompetent BALB/c mice are two-fold higher (n=5,

$1.6 \pm 0.4 \times 10^{-7}$ cm/s) than what was reported in immunocompetent C57BL/6 mice, most likely attributable to the reduced (and less accurate) blood vessel volume estimation resulting from the 2D approach. These measurements in SCID mice also suggest mouse strain as a source of variation.

No significant differences in drug accumulation was measured in the lymph nodes of animals treated VEGF-A relative to untreated controls. There was variability in some measurements, which could not be explained by HPLC inaccuracy since all HPLC drug calibration curves had an R^2 >0.99 and no false positive signal could be detected (Supporting Figure 3). Therefore, the variability was likely due to experimental variability, which could arise from unforeseen variation between animals, including the amount of lymph flow through individual lymph nodes that could lead to drug washout. The brain was harvested to serve as a negative control and, as expected, produced a low signal for doxorubicin [29] and 5-FU [30]. Very little to no signal for paclitaxel [31] and cisplatin [32] was detected in the brain. Interestingly, lymph node paclitaxel penetration was significantly reduced compared to liver at the 2h timepoint, and absent at the 10 minute timepoint (Supporting Figure 4), suggesting a slower drug uptake of paclitaxel in the lymph node. It is unclear from our data whether this is related to the lipophilicity of paclitaxel.

Lymph enters the lymph node via afferent lymphatic vessels to the lymph node subcapsular sinus. It is known that smaller molecules up to an approximate molecular weight of 70 kDa [33-35] from the lymph are found in lymph node conduits, penetrate more deeply and enter the lymph node B- or T-cell zones. Subcapsular macrophages and dendritic cells are known to transfer larger molecules (>70 kDa) from the subcapsular sinus to more superficial B-cells [34, 36-38]. However, molecular delivery to the lymph node from the blood is not well understood and the exact lymph node blood vessel and high-endothelial venule pore cut-off sizes are, to our knowledge, unknown.

Molecules roughly 5 nm or larger are usually impermeable to the blood capillaries within healthy non-lymphoid tissues [39]. HSA is a negatively charged molecule, 3.8 nm in diameter, 15 nm long and ~69 kDa [40] in size. HSA binds paclitaxel and cisplatin (>95%), to a lesser extent doxorubicin (~75%) and some of their degraded products, changing total molecule size and extending plasma half-life [41-44]. HSA binds weakly to 5-FU[45]. Based on our findings that VEGF-A increased lymph node blood vessel EVP to FITC-BSA (~67 kDa in size), we expected that VEGF-A pretreatment would allow more HSA bound paclitaxel, cisplatin and doxorubicin to enter the lymph node and increase maximum drug concentrations. We also hypothesized 5-FU would better penetrate the lymph node than any of the other drugs even without VEGF-A treatment, as it has a much weaker binding to HSA[45]. Doxorubicin, however, exceeded 5-FU drug penetration in all organs, likely as a result of the short plasma half-life of 5-FU[46] which resulted in low blood concentrations at the selected timepoints.

Adair *et al.*[47-49] describe experimental settings in dog popliteal lymph nodes where, under physiologic pressures, 10% of the afferent lymph fluid (not protein) was absorbed by blood vessels in the lymph node. The validity of their findings is strengthened by other data where dog popliteal lymph node blood vessels absorbed up to 50% of fluid in some settings[50]. Protein concentrations under normalized conditions were higher in the efferent lymph vessel than the afferent lymphatic vessels, attributable to protein leaving the blood and net fluid getting absorbed by the blood[49]. Using computational modelling, Jafarnejad *et al.*[51], showed most fluid in the lymph node

subcapsular sinus is hypothesized to travel to the medullary sinuses and leave the node via the efferent lymphatic vessel, following the path of least resistance. This data is supported by Kourtis *et al.*[52], where after peripheral nanoparticle injection, the particles pass the lymph node mostly through the subcapsular sinus. Only approximately 7% of all fluid entering the lymph node reaches the center of the lymph node and is expected to leave through blood vessels under physiological pressures[51]. Fluid flux through the lymph node[51] can also cause washout of drugs, which may dominate vascular permeability as the main determinate of drug accumulation. Any drug in the subcapsular or medullary sinuses is likely to be washed out by lymph flow more easily.

Our measurement method for effective vascular permeability accounts for all processes that move material from the blood vessels to the extravascular space in the center of the lymph node based on FITC-BSA, which pertains to similarly sized HSA-bound chemotherapy. This being said, we are not measuring vascular permeability of fluid, but an effective vascular permeability of FITC-BSA that accounts for net transport effects of diffusive, convective and oncotic forces. While centralized fluid is expected to leave through blood vessels in the lymph node in the physiologic setting[47-49], protein (like albumin) is not expected to[49]. Hence, data in the literature and our effective vascular permeability measurements argue against net protein transport from the lymph node to the blood, but fluid transport can occur in this direction. What happens to other macromolecules and free drug is less clear. Regardless, increasing blood vessel permeability is postulated to decrease or reverse lymph to blood exchange in the lymph node center[51] and promote transport out of the blood. However, drug accumulation did not increase with increased EVP. Thus, a possible explanation for our findings is that VEGF-A increased fluid flow through the lymph node, which carried the drug out of the lymph node towards efferent lymphatic vessels.

Solas *et al.* [11] evaluated protease inhibitor concentrations in lymph nodes of patients infected with HIV. Differential penetration into lymphoid tissue was observed, with average lymph node tissue/plasma concentration ratios 4-8h after drug intake of 2.07, 0.64, 0.58, and 0.21 for the highly lipophilic drugs indinavir, ritonavir, nelfinavir, and lopinavir, respectively. All 41 patients in the study had detectable HIV-1 RNA in lymph node biopsies, while 13 patients had detectable HIV-1 RNA in plasma, indicating that the ratios were at sub-therapeutic levels in these patients. Significantly reduced levels of antiretroviral drug penetration of lymphoid tissue compared to plasma has also been measured in animal models [9, 53-54]. In our study, we calculated average lymph node tissue/plasma concentration ratios at 4 hours for 5-FU, paclitaxel, cisplatin and doxorubicin of 1.5, 0.09, 0.09 and 0.5, respectively. After VEGF-A treatment, the ratio was significantly increased only for paclitaxel (average ratio 0.35 ± 0.07, $p=0.035$). It is unclear however, whether it is low drug concentration in the lymph node that causes therapy failure, or whether certain lymph node regions provide protection for metastatic cancer cells and HIV infected T-cells. B-cell follicles specifically have been shown to constitute sanctuaries for persistent HIV and SIV (HIV nonhuman primate counterpart) infections [13, 55]. More research is needed to evaluate whether what has been learned from HIV studies can be applied to the treatment of lymph node metastasis. However, from our findings we hypothesize that increasing lymph node blood vessel EVP is unlikely to increase therapy effectiveness of the tested chemotherapy drugs without changing their drug properties or reducing drug washout by inhibiting lymph flow.

The present study has limitations. Our goal was to evaluate whether we could increase maximum drug concentration in the lymph node. Therefore, we evaluated the timepoints (10 min, 2 hours, 4

hours, 8 hours and 24 hours) that yielded the highest lymph node drug concentration using 5-FU and paclitaxel (Supporting Figure 4). We moved forward with the 2 hour and 4 hour timepoints, accepting that the area under the curve cannot be calculated from solely these timepoints. Hence, complete evaluation of chemotherapeutic drug penetration during a dosing interval and the pharmacokinetic properties of the respective drugs with or without VEGF-A treatment were not evaluated. In addition, HPLC might not be sensitive enough to detect a small change in drug concentration. Regardless, we could detect drug in all samples, supported by a linear calibration curve even in the low concentration range (Supporting Figure 3). VEGF-A increased effective vascular permeability ~4-fold, and a comparable (or lesser) change in drug accumulation could be easily detected, therefore we believe the technique is capable of detecting major and biologically relevant changes. Moreover, some loss of drug could have occurred in processing, although it was not biased to any particular sample and all relative comparisons are valid. We cannot exclude that the absolute values of drug may underestimate the true tissue concentration. In addition, our study is performed in lymph nodes not harboring metastatic cancer cells. It is known that prior to cancer cell dissemination, tumor draining lymph nodes may undergo many remodeling processes including lymph node lymphangiogenesis, remodeling of high endothelial venules, alterations in immune cell populations, and changes in chemokines and cytokines expression [7]. We hypothesize that these changes might not be as robust in the settings of isolated metastatic cancer cells. However, in the pre- and micro-metastatic setting, changes in conduits and angiogenesis are not reported [20], both of which play a role in molecular transport in lymph nodes. Future evaluation of lymph node blood vessel EVP in the setting of lymph nodes harboring isolated metastatic cancer cells would allow further characterization of chemotherapy penetration in lymph nodes. Lastly, the intravital multiphoton microscopy imaging field of view is limited in x,y and z (~483 × 483 × 136 μm) [14]. Therefore, while the HPLC analysis of lymph nodes was performed on complete lymph nodes, the imaging described for evaluation of blood vessel EVP predominantly included the cortical region of the lymph node.

Globally increasing permeability by using systemic treatments causes drug to accumulate in other organs, arguably even more than in lymph nodes. Specific lymph node targeting would be a promising approach. There are some techniques that target the lymphatic system more specifically by lymphatic drainage. Recent literature[8, 52] describes direct lymph node injection and subcutaneous injections of synthetic materials, biopolymers (e.g. albumin) and nanoparticles. Recent work on endogenous cell-mediated trafficking is also described, employing antigen-presenting cells to target lymphoid organs. Alternatively, therapies to impair lymphatic vessel function can be systemically administered to prevent washout from the lymph nodes by lymph flow, and methods can be developed to measure lymph node drug efflux. Thus, there are multiple approaches which could be employed in future research to help improve drug accumulation in lymph nodes.

In conclusion, here we report measurements of EVP of lymph node blood vessels for the first time as an initial step to understanding the ability of systemic drugs to penetrate and accumulate in lymph nodes. As our basic understanding grows, we hope to exploit our findings to improve the therapeutic efficiency of drugs treating disease in lymph nodes.

Acknowledgements
Research reported in this publication was supported in part by the National Institutes of Health under award numbers DP2OD008780 (T.P.P.), R01HL128168 (J.W.B., T.P.P.), R01CA214913 (T.P.P.), R01CA163528 (B.J.V.), F32CA183465 (D.J.), the UNCF-Merck Science Initiative Postdoctoral Fellowship (D.J.), the Burroughs Wellcome Fund Postdoctoral Enrichment Program Award (D.J.), and the National Cancer Institute Federal Share of Proton Income CA059267 (T.P.P.). The Center for Biomedical OCT Research and Translation also supported this work through Grant Number P41EB015903, awarded by the National Institute of Biomedical Imaging and Bioengineering of the National Institutes of Health. C.B. was supported by a Swiss National Science Foundation early post-doctoral mobility fellowship (P2SKP2_158640).

Conflicts of Interest
The authors declare that they have no competing interests.

Perspectives
We report here the first measurements of effective vascular permeability of lymph node blood vessels. No significant differences in lymph node chemotherapeutic drug concentration were observed after increasing the effective vascular permeability of lymph node blood vessels. We hypothesize that these findings may be explained by fluid flow through the lymph node that causes drug washout. The investigation of alternative drug properties and measuring or altering lymph node drug efflux are promising areas of research to improve drug accumulation in lymph nodes.

References
1. Kawada, K.; Taketo, M. M., Significance and mechanism of lymph node metastasis in cancer progression. Cancer Res 2011, 71 (4), 1214-8.
2. Vakoc, B. J.; Lanning, R. M.; Tyrrell, J. A.; Padera, T. P.; Bartlett, L. A.; Stylianopoulos, T.; Munn, L. L.; Tearney, G. J.; Fukumura, D.; Jain, R. K.; Bouma, B. E., Three-dimensional microscopy of the tumor microenvironment in vivo using optical frequency domain imaging. Nature medicine 2009, 15 (10), 1219-1223.
3. Jain, R. K., Normalizing Tumor Microenvironment to Treat Cancer: Bench to Bedside to Biomarkers. Journal of Clinical Oncology 2013, 31 (17), 2205-2218.
4. Padera, T. P.; Kuo, A. H.; Hoshida, T.; Liao, S.; Lobo, J.; Kozak, K. R.; Fukumura, D.; Jain, R. K., Differential response of primary tumor versus lymphatic metastasis to VEGFR-2 and -3 kinase inhibitors cediranib and vandetanib. Molecular cancer therapeutics 2008, 7 (8), 2272-2279.
5. Eichler, A. F.; Chung, E.; Kodack, D. P.; Loeffler, J. S.; Fukumura, D.; Jain, R. K., The biology of brain metastases—translation to new therapies. Nature Reviews. Clinical Oncology 2011, 8 (6), 344-356.
6. Straver, M. E.; Rutgers, E. J.; Russell, N. S.; Oldenburg, H. S.; Rodenhuis, S.; Wesseling, J.; Vincent, A.; Peeters, M. T., Towards rational axillary treatment in relation to neoadjuvant therapy in breast cancer. European journal of cancer (Oxford, England : 1990) 2009, 45 (13), 2284-92.
7. Pereira, E. R.; Jones, D.; Jung, K.; Padera, T. P., The lymph node microenvironment and its role in the progression of metastatic cancer. Seminars in cell & developmental biology 2015, 38, 98-105.

8. Thomas, S. N.; Schudel, A., Overcoming transport barriers for interstitial-, lymphatic-, and lymph node-targeted drug delivery. Current opinion in chemical engineering 2015, 7, 65-74.
9. Bourry, O.; Mannioui, A.; Sellier, P.; Roucairol, C.; Durand-Gasselin, L.; Dereuddre-Bosquet, N.; Benech, H.; Roques, P.; Le Grand, R., Effect of a short-term HAART on SIV load in macaque tissues is dependent on time of initiation and antiviral diffusion. Retrovirology 2010, 7, 78.
10. Cory, T. J.; Schacker, T. W.; Stevenson, M.; Fletcher, C. V., Overcoming pharmacologic sanctuaries. Current opinion in HIV and AIDS 2013, 8 (3), 190-5.
11. Solas, C.; Lafeuillade, A.; Halfon, P.; Chadapaud, S.; Hittinger, G.; Lacarelle, B., Discrepancies between protease inhibitor concentrations and viral load in reservoirs and sanctuary sites in human immunodeficiency virus-infected patients. Antimicrobial agents and chemotherapy 2003, 47 (1), 238-43.
12. Freeling, J. P.; Ho, R. J., Anti-HIV drug particles may overcome lymphatic drug insufficiency and associated HIV persistence. Proceedings of the National Academy of Sciences of the United States of America 2014, 111 (25), E2512-3.
13. Fukazawa, Y.; Lum, R.; Okoye, A. A.; Park, H.; Matsuda, K.; Bae, J. Y.; Hagen, S. I.; Shoemaker, R.; Deleage, C.; Lucero, C.; Morcock, D.; Swanson, T.; Legasse, A. W.; Axthelm, M. K.; Hesselgesser, J.; Geleziunas, R.; Hirsch, V. M.; Edlefsen, P. T.; Piatak, M., Jr.; Estes, J. D.; Lifson, J. D.; Picker, L. J., B cell follicle sanctuary permits persistent productive simian immunodeficiency virus infection in elite controllers. Nature medicine 2015, 21 (2), 132-9.
14. Meijer, E. F.; Baish, J. W.; Padera, T. P.; Fukumura, D., Measuring Vascular Permeability In Vivo. Methods in molecular biology (Clifton, N.J.) 2016, 1458, 71-85.
15. Carmeliet, P.; Jain, R. K., Molecular mechanisms and clinical applications of angiogenesis. Nature 2011, 473 (7347), 298-307.
16. Senger, D. R.; Galli, S. J.; Dvorak, A. M.; Perruzzi, C. A.; Harvey, V. S.; Dvorak, H. F., Tumor cells secrete a vascular permeability factor that promotes accumulation of ascites fluid. Science (New York, N.Y.) 1983, 219 (4587), 983-5.
17. Azzi, S.; Hebda, J. K.; Gavard, J., Vascular permeability and drug delivery in cancers. Frontiers in oncology 2013, 3, 211.
18. Leunig, M.; Yuan, F.; Menger, M. D.; Boucher, Y.; Goetz, A. E.; Messmer, K.; Jain, R. K., Angiogenesis, microvascular architecture, microhemodynamics, and interstitial fluid pressure during early growth of human adenocarcinoma LS174T in SCID mice. Cancer Res 1992, 52 (23), 6553-60.
19. Brown, E.; Munn, L. L.; Fukumura, D.; Jain, R. K., In vivo imaging of tumors. Cold Spring Harbor protocols 2010, 2010 (7), pdb.prot5452.
20. Jeong, H. S.; Jones, D.; Liao, S.; Wattson, D. A.; Cui, C. H.; Duda, D. G.; Willett, C. G.; Jain, R. K.; Padera, T. P., Investigation of the Lack of Angiogenesis in the Formation of Lymph Node Metastases. Journal of the National Cancer Institute 2015, 107 (9).
21. Rasband, W. S. ImageJ, U. S. National Institutes of Health, Bethesda, Maryland, USA. http://rsb.info.nih.gov/ij/.
22. Van den Broeck, W.; Derore, A.; Simoens, P., Anatomy and nomenclature of murine lymph nodes: Descriptive study and nomenclatory standardization in BALB/cAnNCrl mice. Journal of immunological methods 2006, 312 (1-2), 12-9.

23. Feng, D.; Nagy, J. A.; Hipp, J.; Dvorak, H. F.; Dvorak, A. M., Vesiculo-vacuolar organelles and the regulation of venule permeability to macromolecules by vascular permeability factor, histamine, and serotonin. The Journal of experimental medicine 1996, 183 (5), 1981-6.
24. Dellian, M.; Witwer, B. P.; Salehi, H. A.; Yuan, F.; Jain, R. K., Quantitation and physiological characterization of angiogenic vessels in mice: effect of basic fibroblast growth factor, vascular endothelial growth factor/vascular permeability factor, and host microenvironment. The American journal of pathology 1996, 149 (1), 59-71.
25. Monsky, W. L.; Fukumura, D.; Gohongi, T.; Ancukiewcz, M.; Weich, H. A.; Torchilin, V. P.; Yuan, F.; Jain, R. K., Augmentation of transvascular transport of macromolecules and nanoparticles in tumors using vascular endothelial growth factor. Cancer Res 1999, 59 (16), 4129-35.
26. Fukumura, D.; Gohongi, T.; Kadambi, A.; Izumi, Y.; Ang, J.; Yun, C. O.; Buerk, D. G.; Huang, P. L.; Jain, R. K., Predominant role of endothelial nitric oxide synthase in vascular endothelial growth factor-induced angiogenesis and vascular permeability. Proceedings of the National Academy of Sciences of the United States of America 2001, 98 (5), 2604-9.
27. Tsuzuki, Y.; Mouta Carreira, C.; Bockhorn, M.; Xu, L.; Jain, R. K.; Fukumura, D., Pancreas microenvironment promotes VEGF expression and tumor growth: novel window models for pancreatic tumor angiogenesis and microcirculation. Laboratory investigation; a journal of technical methods and pathology 2001, 81 (10), 1439-51.
28. Fukumura, D.; Yuan, F.; Monsky, W. L.; Chen, Y.; Jain, R. K., Effect of host microenvironment on the microcirculation of human colon adenocarcinoma. The American journal of pathology 1997, 151 (3), 679-88.
29. Sardi, I.; la Marca, G.; Cardellicchio, S.; Giunti, L.; Malvagia, S.; Genitori, L.; Massimino, M.; de Martino, M.; Giovannini, M. G., Pharmacological modulation of blood-brain barrier increases permeability of doxorubicin into the rat brain. American journal of cancer research 2013, 3 (4), 424-32.
30. Lin, N. U.; Bellon, J. R.; Winer, E. P., CNS metastases in breast cancer. Journal of clinical oncology : official journal of the American Society of Clinical Oncology 2004, 22 (17), 3608-17.
31. Fellner, S.; Bauer, B.; Miller, D. S.; Schaffrik, M.; Fankhanel, M.; Spruss, T.; Bernhardt, G.; Graeff, C.; Farber, L.; Gschaidmeier, H.; Buschauer, A.; Fricker, G., Transport of paclitaxel (Taxol) across the blood-brain barrier in vitro and in vivo. The Journal of clinical investigation 2002, 110 (9), 1309-18.
32. Minami, T.; Okazaki, J.; Kawabata, A.; Kuroda, R.; Okazaki, Y., Penetration of cisplatin into mouse brain by lipopolysaccharide. Toxicology 1998, 130 (2-3), 107-13.
33. Gretz, J. E.; Norbury, C. C.; Anderson, A. O.; Proudfoot, A. E.; Shaw, S., Lymph-borne chemokines and other low molecular weight molecules reach high endothelial venules via specialized conduits while a functional barrier limits access to the lymphocyte microenvironments in lymph node cortex. The Journal of experimental medicine 2000, 192 (10), 1425-40.
34. Sixt, M.; Kanazawa, N.; Selg, M.; Samson, T.; Roos, G.; Reinhardt, D. P.; Pabst, R.; Lutz, M. B.; Sorokin, L., The conduit system transports soluble antigens from the afferent lymph to resident dendritic cells in the T cell area of the lymph node. Immunity 2005, 22 (1), 19-29.

35. Nolte, M. A.; Belien, J. A.; Schadee-Eestermans, I.; Jansen, W.; Unger, W. W.; van Rooijen, N.; Kraal, G.; Mebius, R. E., A conduit system distributes chemokines and small blood-borne molecules through the splenic white pulp. The Journal of experimental medicine 2003, 198 (3), 505-12.
36. Roozendaal, R.; Mempel, T. R.; Pitcher, L. A.; Gonzalez, S. F.; Verschoor, A.; Mebius, R. E.; von Andrian, U. H.; Carroll, M. C., Conduits mediate transport of low-molecular-weight antigen to lymph node follicles. Immunity 2009, 30 (2), 264-76.
37. Phan, T. G.; Grigorova, I.; Okada, T.; Cyster, J. G., Subcapsular encounter and complement-dependent transport of immune complexes by lymph node B cells. Nature immunology 2007, 8, 992-1000.
38. Carrasco, Y. R.; Batista, F. D., B cells acquire particulate antigen in a macrophage-rich area at the boundary between the follicle and the subcapsular sinus of the lymph node. Immunity 2007, 27 (1), 160-71.
39. Kaminskas, L. M.; Kota, J.; McLeod, V. M.; Kelly, B. D.; Karellas, P.; Porter, C. J., PEGylation of polylysine dendrimers improves absorption and lymphatic targeting following SC administration in rats. Journal of controlled release : official journal of the Controlled Release Society 2009, 140 (2), 108-16.
40. Gekle, M., Renal tubule albumin transport. Annual review of physiology 2005, 67, 573-94.
41. Purcell, M.; Neault, J. F.; Tajmir-Riahi, H. A., Interaction of taxol with human serum albumin. Biochimica et biophysica acta 2000, 1478 (1), 61-8.
42. Neault, J. F.; Tajmir-Riahi, H. A., Interaction of cisplatin with human serum albumin. Drug binding mode and protein secondary structure. Biochimica et biophysica acta 1998, 1384 (1), 153-9.
43. Agudelo, D.; Berube, G.; Tajmir-Riahi, H. A., An overview on the delivery of antitumor drug doxorubicin by carrier proteins. International journal of biological macromolecules 2016, 88, 354-60.
44. Barakat, R. R.; Markman, M.; Randall, M. E., Principles and practice of gynecologic oncology. 5th ed.; Philadelphia: Wolters Kluwer Lippincott Williams & Wilkins: 2009. p386.
45. Bertucci, C.; Ascoli, G.; Uccello-Barretta, G.; Di Bari, L.; Salvadori, P., The binding of 5-fluorouracil to native and modified human serum albumin: UV, CD, and 1H and 19F NMR investigation. Journal of pharmaceutical and biomedical analysis 1995, 13 (9), 1087-93.
46. Bocci, G.; Danesi, R.; Di Paolo, A. D.; Innocenti, F.; Allegrini, G.; Falcone, A.; Melosi, A.; Battistoni, M.; Barsanti, G.; Conte, P. F.; Del Tacca, M., Comparative pharmacokinetic analysis of 5-fluorouracil and its major metabolite 5-fluoro-5,6-dihydrouracil after conventional and reduced test dose in cancer patients. Clinical cancer research : an official journal of the American Association for Cancer Research 2000, 6 (8), 3032-7.
47. Adair, T. H.; Guyton, A. C., Modification of lymph by lymph nodes. II. Effect of increased lymph node venous blood pressure. The American journal of physiology 1983, 245 (4), H616-22.
48. Adair, T. H.; Guyton, A. C., Modification of lymph by lymph nodes. III. Effect of increased lymph hydrostatic pressure. The American journal of physiology 1985, 249 (4 Pt 2), H777-82.

49. Adair, T. H.; Moffatt, D. S.; Paulsen, A. W.; Guyton, A. C., Quantitation of changes in lymph protein concentration during lymph node transit. The American journal of physiology 1982, 243, H351-9.
50. Knox, P.; Pflug, J. J., The effect of the canine popliteal node on the composition of lymph. The Journal of physiology 1983, 345, 1-14.
51. Jafarnejad, M.; Woodruff, M. C.; Zawieja, D. C.; Carroll, M. C.; Moore, J. E., Jr., Modeling Lymph Flow and Fluid Exchange with Blood Vessels in Lymph Nodes. Lymphatic research and biology 2015, 13 (4), 234-47.
52. Kourtis, I. C.; Hirosue, S.; de Titta, A.; Kontos, S.; Stegmann, T.; Hubbell, J. A.; Swartz, M. A., Peripherally administered nanoparticles target monocytic myeloid cells, secondary lymphoid organs and tumors in mice. PloS one 2013, 8 (4), e61646.
53. Horiike, M.; Iwami, S.; Kodama, M.; Sato, A.; Watanabe, Y.; Yasui, M.; Ishida, Y.; Kobayashi, T.; Miura, T.; Igarashi, T., Lymph nodes harbor viral reservoirs that cause rebound of plasma viremia in SIV-infected macaques upon cessation of combined antiretroviral therapy. Virology 2012, 423 (2), 107-18.
54. North, T. W.; Higgins, J.; Deere, J. D.; Hayes, T. L.; Villalobos, A.; Adamson, L.; Shacklett, B. L.; Schinazi, R. F.; Luciw, P. A., Viral sanctuaries during highly active antiretroviral therapy in a nonhuman primate model for AIDS. Journal of virology 2010, 84 (6), 2913-22.
55. Deleage, C.; Wietgrefe, S. W.; Del Prete, G.; Morcock, D. R.; Hao, X. P.; Piatak, M., Jr.; Bess, J.; Anderson, J. L.; Perkey, K. E.; Reilly, C.; McCune, J. M.; Haase, A. T.; Lifson, J. D.; Schacker, T. W.; Estes, J. D., Defining HIV and SIV Reservoirs in Lymphoid Tissues. Pathogens & immunity 2016, 1 (1), 68-106.

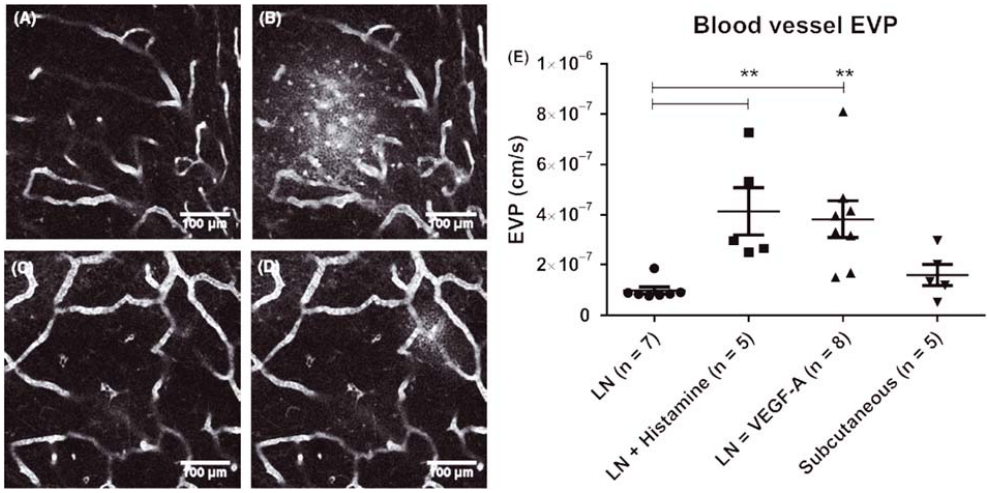

Figure 1. Blood vessel effective vascular permeability.
A) Intravital multiphoton microscopy demonstrates presence of FITC-BSA in lymph node blood vasculature of a BALB/c mouse ~ 30 seconds after intravenous injection. B) Image of the same location as A ~14 minutes later shows FITC-BSA extravasation; most apparent in the left half of the image. C-D) Images at 30 seconds (C) and 14 minutes (D) after injection show extravasation of FITC-BSA in the interstitial space after VEGF-A treatment in a different BALB/c mouse. E) EVP measurements performed in normal, histamine treated and VEGF-A treated lymph nodes, as well as subcutaneous blood vessels. Mean and SEM are reported. ** = $p < 0.01$ using Dunn's multiple comparisons test (ANOVA).

	Molecular weight (Da)	Lipophilicity	Charge
5-FU	130	Low	Negative
Paclitaxel	854	High	Negative
Cisplatin	300	Low	Neutral
Doxorubicin	580	Low	Positive

Table 1. Chemotherapeutic drug properties.

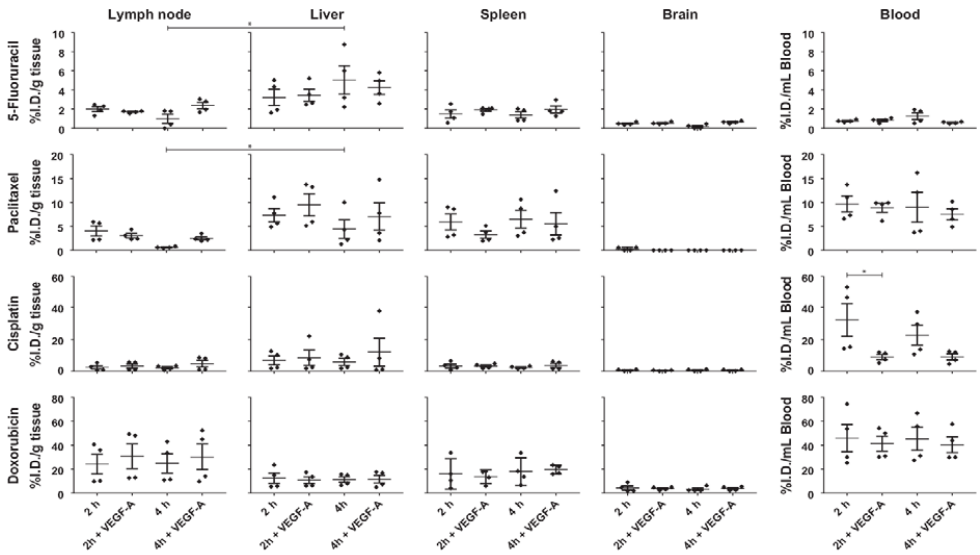

Figure 2. Chemotherapeutic drug concentrations in normal and VEGF-A treated lymph nodes.
This figure shows data for all measured chemotherapeutic drugs (5-FU, paclitaxel, cisplatin and doxorubicin) at 2 hours and 4 hours after drug injection, with and without VEGF-A treatment. N=4 per group, mean and SEM are reported. * = p <0.05 using an unpaired nonparametric Mann-Whitney *t* test or Dunn's multiple comparisons test (ANOVA).

Site	Strain	*2D* Method	*3D* Method	References
Brain	SCID	~5.0×10^{-8} cm/s		22
Liver	SCID	~2.7×10^{-8} cm/s		25
Pancreas	SCID	~5.0×10^{-8} cm/s		24
Subcutaneous blood vessels	SCID	~5.0×10^{-8} cm/s		22
Subcutaneous blood vessels	C57BL/6	~7.5×10^{-8} cm/s		23
Subcutaneous blood vessels	BALB/c		$1.6 \pm 0.4 \times 10^{-7}$ cm/s	
Lymph node	BALB/c		$9.9 \pm 1.5 \times 10^{-8}$ cm/s	
Lymph node + Histamine	BALB/c		$4.1 \pm 0.9 \times 10^{-7}$ cm/s	
Lymph node + VEGF-A	BALB/c		$3.8 \pm 0.7 \times 10^{-7}$ cm/s	

Table 2. Summary of effective vascular permeability measurements in mice employing FITC-BSA in a 2D or 3D method.

7. Methicillin-resistant Staphylococcus aureus pathogenicity causes sustained lymphatic dysfunction

Dennis Jones[1,2], Eelco FJ Meijer[1,2], Cedric Blatter[2,3], Shan Liao[1,5], Ethel Pereira[1,2], Echoe Bouta[1,2], Keehoon Jung[1,2], Shan Min Chin[1,2], Peigen Huang[1,2], Lance L. Munn[1,2], Benjamin J. Vakoc[2,3], Michael Otto[4] and Timothy P. Padera[1,2*]

[1]Edwin L. Steele Laboratory, Department of Radiation Oncology, MGH Cancer Center, Massachusetts General Hospital, 100 Blossom Street, Boston, Massachusetts 02114, USA. [2]Harvard Medical School, Boston, Massachusetts 02115, USA. [3]Wellman Center for Photomedicine, Massachusetts General Hospital, Boston, Massachusetts 02114, USA. [4]Laboratory of Bacteriology, National Institute of Allergy and Infection Disease, National Institutes of Health, Bethesda, MD 20814, USA. [5]Present address: Department of Microbiology, Immunology and Infectious Diseases, University of Calgary, 3330 Hospital Drive NW, Calgary, Alberta T2N 4N1 Canada. *To whom correspondence should be addressed: Timothy P. Padera (tpadera@steele.mgh.harvard.edu)

Science Translational Medicine, In Press.

Abstract:
Methicillin-Resistant *Staphylococcus aureus* (MRSA) is a major cause of morbidity and mortality worldwide and is a frequent cause of skin and soft tissue infections (SSTIs). SSTIs are strongly associated with co-morbidities that have impaired lymphatic vessel function, including lymphedema. SSTIs also frequently recur in patients and sometimes lead to acquired lymphedema. However, the mechanism of how SSTIs can be both the consequence and cause of lymphatic vessel dysfunction is not known. Intravital imaging revealed both an acute reduction in lymphatic vessel contractility and lymph flow after localized MRSA infection as well as chronic lymphatic impairment long after MRSA is cleared and inflammation is resolved. Associated with decreased lymphatic function was the loss and disorganization of lymphatic muscle cells (LMCs), critical for lymphatic contraction. *In vitro*, incubation of MRSA-conditioned supernatant led to LMC death. Proteomic analysis identified several accessory gene regulator (*agr*)- controlled MRSA exotoxins that contribute to LMC death. Infection with *agr* mutant MRSA resulted in sustained lymphatic function compared to animals infected with wild type MRSA. Our findings suggest that *agr* is a promising target to preserve lymphatic vessel function and promote immunity during SSTIs.

Introduction:
Skin and soft tissue infections (SSTIs) are caused by microbial invasion of the epidermis, for which there are 14 million out-patient visits annually in the United States (*1)*. Patients are generally treated with oral and topical antibiotics. However, complicated infections may additionally require intravenous antibiotics, leading to nearly 500,000 hospital admissions each year in the US (*2,3)*. The most common pathogens associated with bacterial infections of the skin and underlying tissues are beta-hemolytic *Streptococci* and *Staphylococcus aureus,* including strains of methicillin-resistant *Staphylococcus aureus* (MRSA) (*4)*. The resistance of MRSA to antibiotics, along with an increasing incidence of infections, has become an increasing public health concern for individuals in the community and hospital settings (*5)*, and underscores the need for treatments that target both MRSA colonization and its pathogenesis (*6)*. These infections can often recur and are associated with patients with impaired lymphatic function, including those with lymphedema (*7,8)*. Further SSTIs can also lead to secondary lymphedema (*7*), suggesting that SSTIs can be both the consequence and cause of impaired lymphatic function. However, little is known about how bacteria interact with lymphatic vessels. Understanding this relationship will be critical to developing future therapies and vaccination strategies that maintain lymph flow to improve clearance of MRSA and toxins as well as promote antigen delivery to the lymph node for robust immune responses.

The lymphatic vasculature consists of a network of vessels critical for maintenance of tissue homeostasis, fluid balance, immune function, absorption of dietary fat and lipid transport (*9)*. Disruption or malfunction of lymphatic vessels can result in lymphedema, presented as local fluid retention and tissue swelling (*10)*. Primary lymphedema has a genetic etiology that leads to lymphatic insufficiency (*11-14)*. In contrast, secondary lymphedema is more common and is triggered by obstruction or damage to lymphatic vessels, including iatrogenic damage, inflammation or infection—either bacterial or parasitic (*15,16)*. Individuals with lymphedema are prone to develop erysipelas and underlying tissue cellulitis (*17)*.

Lymph flow is controlled by a combination of factors that propel lymph to the lymph nodes for immune surveillance and filtration (*18,19)*. Primarily, the organized lymphatic muscle cells (LMCs) that cover collecting lymphatic vessels periodically contract to drive lymph forward (*20)*. Calcium (Ca^{2+}) signaling in LMCs drives contraction in response to chemical and mechanical stimuli such as endothelium-derived factors and lymph flow, respectively (*21,22)*. Nitric oxide, a vasodilator produced by the endothelium in normal and inflammatory conditions, has been shown to have a context-dependent effect on lymphatic contraction. In normal physiology, loss of nitric oxide has been shown to strengthen, blunt, or have no effect on lymphatic contraction (*23-25)*. We have previously reported using mathematical modeling that spatiotemporal changes in Ca^{2+} and nitric oxide generate complementary feedback loops that respond to local pressure and shear stress, and are sufficient to drive lymph flow (*26)*. Perturbations in either Ca^{2+} or nitric oxide signaling such as blocking Ca^{2+} channels and increasing nitric oxide production, respectively, have been shown to significantly compromise lymphatic contraction (*23,24,27,28)*.

Results:
Establishment of a localized MRSA infection model
To examine a potential relationship between MRSA infection and lymphatic function, we established a MRSA infection model of the mouse hindlimb, a location analogous to the commonly

affected lower extremities in human SSTIs (*29,30)*. Neutrophils infiltrated the hindlimb and draining lymph node **(SFig.1a-d)** within 24 hours post-infection. Lymphangiography revealed dilated afferent lymphatic vessels to the popliteal lymph node, which we designate here as PLVs, compared to PLVs of uninfected mice (**Fig. 1a-b**, **SFig. 1a,e)**.

Acute inhibition of lymphatic function after MRSA infection

Since dilated lymphatic vessels are associated with lymphatic dysfunction (*31)*, we measured the ability of PLVs to contract using intravital fluorescence microscopy **(Fig. 1a**) (*32)*. MRSA infection caused a significant impairment in lymphatic contraction compared to uninfected animals (**Fig. 1a-b, and Movies S1 and S2**). The strength of PLV contraction, as measured by ejection fraction—the theoretical fractional volume of lymph expelled with each vessel contraction—declined significantly after infection (**Fig. 1c)**. As shown in **Fig. 1d**, PLVs from infected animals also showed a significant decrease in phasic contraction frequency compared to uninfected controls.

To determine if lymph flow inside PLVs was also decreased, we employed a recently developed label-free method to identify PLVs (**Fig. 1e)** and directly measure instantaneous total lymph velocity (basal and pulsatile flow) *in vivo* by Doppler optical coherence tomography (DOCT) (*33)*. In uninfected mice, 90% of the lymph velocity measurements showed distinct peaks in flow in the PLV (**Fig. 1e).** Four days after infection, only 33% of the lymph velocity measurements were pulsatile, with others showing constant, yet reduced lymph velocity compared to uninfected animals **(Fig. 1e-f)**. Taken together, mice infected with MRSA demonstrated significant inhibition of lymphatic vessel contraction and lymph velocity during active infection.

Resolution of inflammation and infection clearance

Subcutaneous infection of mice with MRSA led to a transient infection, with the peak of bacterial burden in the infected skin and underlying muscle, as well as in the lymph node, at 4 days post-infection **(Fig. 2a)**. Consistent with previous results for subcutaneous MRSA infections in mice, MRSA in skin (*34)* and ipsilateral popliteal lymph node (PLN) was not detected by colony formation assays 30 days post-infection **(Fig. 2a)**. Similar results were obtained using qPCR to detect *mecA* and *thermonuclease*—both *Staphylococcal*-specific genes **(SFig. 2a-b)**. Concomitant with the presence of inflammatory cells during early infection **(SFig.1a-d)**, a gene array measured an increase in several key genes that mediate the host inflammatory response **(Fig. 2b)**. Notably, IL-1β—a protein essential for host defense against *S. aureus (35)*—was the most highly upregulated gene four days after infection. In contrast, 60 days after infection, the inflammatory gene profile mirrored the expression profile of uninfected mice. These data show MRSA clearance and resolution of inflammation by 30 and 60 days post-infection, respectively.

Chronic inhibition of lymphatic function after clearance of MRSA

By 120 days post-infection, lymphatic vessel diameter had returned to the normal range found in most uninfected animals **(SFig. 2c)**. Surprisingly, the strength **(Fig. 2c)** and frequency **(Fig. 2d)** of PLV contraction remained impaired after clearance of infection at day 30 and impairment was sustained 120 days post-infection ($p<0.05$). Using DOCT to measure lymph flow **(Fig. 2e)**, we found pulsatile lymph flow in only 50% of the mice measured after MRSA clearance (35 days post-MRSA infection) compared to 90% of mice in the control group **(Fig. 2e).** Additionally, measurements made 35 days post-MRSA infection showed limited net flow velocity **(Fig. 2f)**

($p<0.05$), comparable to flow velocity measurements 4 days post-infection. Surprisingly, only 28% of mice at 260 days post-MRSA infection showed pulsatile lymph flow. Net lymph velocity was also decreased in MRSA-infected mice relative to age-matched controls 260 days post-infection **(SFig. 2d)**($p<0.05$).

Nitric oxide inhibition and lymphatic function during infection

We hypothesized that nitric oxide produced by infiltrating cells during MRSA infection could disrupt the temporal and spatial nitric oxide gradients established by lymphatic endothelial cells (*24,27,36)*, similar to sterile inflammation (*24)*. Using immunofluorescence, inducible nitric oxide synthase (iNOS) was identified in inflammatory cells in the skin and within the abscess (**Fig. 3a)**. iNOS-positive cells were often found in proximity to lymphatic vessels (**Fig. 3a)**, suggesting a potential role for iNOS in inhibiting lymphatic contraction. Unexpectedly, the majority of iNOS-positive cells did not stain positively for Gr-1, a marker of neutrophils and myeloid-derived suppressor cells (MDSCs) (**Fig. 3b).** Depletion of Gr-1+ cells led to greater reduction of lymphatic contraction **(SFig. 3a)**, likely due to the critical role of Gr-1+ cells in host defense during acute infection (*37)*. These findings are in contrast to the role of Gr-1+ MDSCs in a model of sterile inflammation (*24)*. Next, we tested whether MRSA-derived lipoteichoic acid (LTA), through production of iNOS by macrophages (*38)*, inhibited lymphatic contraction during MRSA infection. Purified LTA injected into mouse hindlimb decreased lymphatic contraction in a dose-dependent manner (**Fig. 3c**), but did not impair lymphatic contraction in iNOS deficient mice (iNOS KO) (**Fig. 3c**). This suggests that LTA acts through iNOS to reduce the strength of lymphatic function, similar to sterile inflammation (*24)*. Although the concentration of LTA at day 4 of MRSA infection was comparable to purified LTA at the same time point **(S.Fig 3b)**, iNOS KO mice infected with MRSA maintained a significant reduction in lymphatic contraction, suggesting bacterial-derived LTA is not solely responsible for inhibiting lymphatic contraction **(Fig. 3d)**. Further, animals injected with LTA showed normal lymphatic contraction 30 and 60 days after LTA injection **(S.Fig 3c)**.

Another source of nitric oxide is MRSA itself, which use nitric oxide synthase oxygenase (saNOS) to catalyzes nitric oxide production from L-arginine (*39)*. Infection of wild-type mice with MRSA lacking saNOS (ΔsaNOS) resulted in reduced lymphatic vessel contraction (**Fig. 3d**). Similarly, infection of iNOS KO mice with ΔsaNOS MRSA did not improve PLV contraction (**Fig. 3d**). These results suggest that nitric oxide—produced by iNOS or bacterial saNOS—is not the sole inhibitor of lymphatic contraction during infection.

Inhibition of inflammation and lymphatic function during infection

The inflammatory cytokines IL-1β, TNF-α (both elevated in **Fig. 2b**) and IL-6 have been previously shown to decrease lymphatic contraction and lymph flow (*40)*. Although MyD88 null mice (MyD88 KO) show attenuated production of these cytokines after intravenous *S. aureus* challenge (*41,42)*, lymphatic contraction in MRSA-infected MyD88 KO mice revealed no improvement in lymphatic function (measured by intravital microscopy) 4 days after infection, compared to infected WT mice **(SFig. 3d)**. Additionally, prophylactic and therapeutic neutralization of TNF-α yielded no benefit in lymphatic function during MRSA infection **(SFig. 3e)**. Finally, mice treated prophylactically and during active infection with non-steroidal anti-inflammatory drugs (NSAIDs)—the cyclooxygenase inhibitors acetylsalicylic acid (aspirin) or etodolac—did not exhibit enhanced lymphatic contraction **(SFig. 3f)** relative to vehicle control.

Loss of lymphatic muscle cells after MRSA infection

Since reducing host inflammation and inflammatory cytokines did not improve lymphatic function **(Fig 3, SFig. 3a,d-f)**, we analyzed the cellular integrity of PLVs after MRSA infection. To this end, we performed immunohistochemical staining on hindlimb tissue. Using CD31 to identify blood and lymphatic vessels **(SFig. 4a)**, we found decreased α-SMA staining of the PLV and adjacent posterior tibial artery 36 hours after infection **(Fig. 4a)**. No apoptotic α-SMA cells were detected using TUNEL staining **(Fig. 4a).** Since this finding suggested decreased lymphatic muscle and smooth muscle cell coverage, we next used mice that express DsRed under the control of the α-smooth muscle actin gene promoter (αSMA-DsRed) (*24)* to identify the LMCs of FITC dextran-filled lymphatic vessels **(Fig. 4b)**. Immunofluorescent staining and confocal microscopy of PLVs revealed decreased LMC coverage and altered DsRed localization 4 days post-infection **(Fig. 4b-c)** ($p<0.05$). Additionally, loss of SMC coverage was measured in the posterior tibial artery **(Fig. 4a-b, SFig. 4b)**. In contrast to smooth muscle cells **(SFig. 4b)**, LMC coverage was not completely regained 30 days post-infection **(Fig. 4c-d)**. Interestingly, LMCs showed an elongated pattern of αSMA distribution after infection. To confirm LMC loss, we analyzed the expression of αSMA by immunofluorescence using optically cleared hindlimb tissue. In agreement with findings from αSMA-DsRed reporter mice, infection of wild type mice led to attenuated LMC coverage 4 days post infection ($p<0.05$) with partial recovery 30 days after infection **(Fig. 4e-f)**. Surprisingly, 260 days post-infection, decreased LMC coverage persisted ($p<0.05$) and LMCs displayed abnormal morphology and distribution of αSMA compared to the corresponding uninfected contralateral leg of the same animal **(Fig. 4g-h)**.

MRSA-induced lymphatic muscle cell death

MRSA can damage biological membranes in several cell types, leading to cell death (*43)*. We investigated whether MRSA could cause death of LMCs. To this end, we isolated LMCs from murine PLVs and cultured them *in vitro* **(SFig. 5a)**. After 24 hours of incubation with MRSA-conditioned supernatant, LMC viability *in vitro* was significantly diminished **(Fig. 5a)** compared to control media (tryptic soy broth, TSB) ($p<0.05$).

Lysis of lymphatic muscle cells by MRSA protein(s)

Since LMCs are critical for lymphatic contraction, we sought to further assess the mechanism of LMC death. To determine if the relevant secreted factor(s) in the MRSA-conditioned supernatant were proteins, we pretreated MRSA-conditioned supernatant with trypsin. To test the relevance to human disease mechanisms, we added MRSA-conditioned supernatant, pretreated with trypsin, to human smooth muscle cells hSMCs. Trypsin abolished the lethality of MRSA-conditioned supernatant on hSMCs **(SFig. 6a)**, suggesting that protein(s) mediate the observed cell death. Since TUNEL-positive cells were only found within abscesses **(SFig. 6b)**, mechanisms other than apoptosis likely operates to cause LMC death *in vivo*. We next asked if cellular lysis represents the mechanism of MRSA-induced cell death of LMCs. We incubated MRSA conditioned supernatant with LMCs or hSMCs for 6-18 hrs. Subsequently, we collected the media and assessed MRSA cytotoxicity by measuring the release of lactate dehydrogenase (LDH) into the media. The LDH release assay indicated MRSA cytolysis for LMCs **(Fig. 6b)** and hSMCs **(SFig. 6c)**.

Identification of toxins in MRSA-conditioned supernatant

We used mass spectrometry to analyze the supernatant fraction from the MRSA strain USA300

JE2 and found 233 proteins that were highly enriched in the supernatant compared to control media **(Fig. 5b)**. Toxin expression in the MRSA-conditioned supernatant was abundant (see full list of proteins identified in the **Supplemental Table**), accounting for 9% of identified proteins with known function **(SFig. 7a)**. Expression of many toxins is primarily dependent on the accessory gene regulator (*agr*) operon **(Fig. 5c)**. Based on their high expression level in MRSA supernatant, we chose to investigate the effect of delta hemolysin, alpha-hemolysin and phenol soluble modulin alpha-1 (PSMα1) on LMCs.

Death of lymphatic muscle cells from MRSA toxins

To this end, we added recombinant delta hemolysin, alpha hemolysin or PSMα1 to LMCs *in vitro*. Incubation of each toxin with LMCs led to cell lysis, with PSMα1 causing the greatest degree of cytolysis **(Fig. 5d)**. However, genetic deletion of delta hemolysin (*hld*) or alpha hemolysin (*hla*) did not render LMCs viable after incubation with conditioned media from these respective mutants **(Fig. 5e)**. Incubation of conditioned media from a genetic deletion of *psmα* (including *psmα1* through *psmα*4) resulted in minimal improvement in LMC viability, also seen in a mutant with combined disruption of the *psmα*, *psmβ*, and *hld* (combined deletion) loci **(Fig. 5e)**. *In vivo*, lymphatic contraction **(Fig. 5f)** and frequency **(Fig. 5g)** of mice infected with *hld*, *psm*, and combined deletion mutants remained significantly reduced after 30 days relative to PBS sham infected mice. LMC coverage after infection with mutants was comparable to that of WT MRSA **(Fig. 5h)**. Taken together, these data suggest a combinatory or compensatory role for toxins towards LMC lethality. To this point, an alpha hemolysin neutralizing antibody was sufficient to prevent hSMC viability loss from recombinant alpha hemolysin **(SFig. 7f)** ($p<0.05$), but had no effect on the lethality from MRSA-conditioned supernatant **(SFig. 7g)** ($p>0.05$).

Effect of MRSA on additional cells associated with blood and lymphatic vasculature

To determine the mechanism for loss of vascular SMCs (**Fig. 4b, SFig, 4a-b**), we incubated MRSA-conditioned supernatant with murine SMCs **(SFig. 7c)** and found that MRSA-conditioned supernatant killed murine SMCs. To determine if MRSA had an effect on lymphatic endothelial cells (LECs), we cultured primary human LECs with MRSA supernatant and showed LEC lethality **(SFig. 5c, SFig. 7d)**. Taken together, these data suggest that MRSA cytotoxicity is not limited to LMCs of the lymphatic vasculature and explain the loss of smooth muscle cells of the posterior tibial artery.

Interestingly, the individual effects of alpha hemolysin, delta hemolysin and PSMs appear to be cell-specific, as delta hemolysin and PSMs appear to play critical roles in human **(SFig. 7b,e)** and murine **(SFig. 7c)** SMC death, but not LMC **(Fig. 5e)** killing *in vitro*. Deletion of *hla* and *psmβ* in MRSA also resulted in improved viability in lymphatic endothelial cells **(SFig. 7d)**.

***agr*-dependent inhibition of lymphatic function**

Next, we employed an *agr* mutant of the USA300 strain of MRSA, which has diminished production of several virulence-associated genes including *hld* (delta hemolysin) and *hla* (alpha hemolysin) (*44,45)*. Further, *agr* mutant of the USA300 strain of MRSA had no detectable PSM expression (*46)*. Using mass spectrometry, we also found enrichment of several toxins in wild type MRSA supernatant compared to *agr* mutant supernatant **(Fig. 5c)**. Unlike WT MRSA-conditioned supernatant, *agr* mutant-conditioned supernatant was not cytotoxic and did not cause death of LMCs, SMCs or LECs **(Fig. 6a, SFig 7b-d).** *In vivo*, mice infected with *agr* mutant MRSA had

LMC coverage comparable to uninfected mice **(Fig. 6c)**. Further *agr* mutant-infected mice showed stronger lymphatic function relative to mice infected with the parental strain at day 30, which is after clearance of MRSA **(Fig. 6d and Movies S3 and S4)**. The strength of PLV contraction (ejection fraction) in *agr* mutant-infected mice was 58% stronger relative to the contraction of animals infected with WT MRSA. Several animals showed contraction strength similar to that of uninfected mice **(Fig. 6e)**. Moreover, the frequency of lymphatic vessel contraction was significantly faster in *agr* mutant-infected mice compared to WT MRSA **(Fig. 6f)**. Of note, the contraction frequency of *agr* mutant-infected mice was increased relative to uninfected mice, potentially compensating for the moderately lower ejection fraction. Taken together, these data suggest that *agr*-dependent MRSA toxins are primarily responsible for long-term inhibition of lymphatic function.

Discussion:
MRSA compromises and evades host immune responses by several mechanisms, including, but not limited to, suppressing chemotaxis of leukocytes, toxin-mediated killing of leukocytes and the production of superantigens to impair the immune response (*47)*. Here, we used the endemic USA300 strain of CA-MRSA, a common agent of serious bacterial infections in the United States, to investigate its effect on lymphatic vessels in a murine model of infection. Our data show that a single MRSA infection inhibits lymphatic contraction long after the infection is cleared.

Using a novel label-free method to measure lymph flow velocity by DOCT in the mouse, we show, for the first time, reduction of lymph flow velocity during MRSA infection. We found that tissue remodeling and associated fluid accumulation due to infection added difficulty to obtaining lymph velocity measurements at day 4 post-infection. However, we were able to obtain accurate lymph velocity measurements with DOCT that suggest lymphatic vessels do not exhibit strong, pulsatile flow after MRSA infection. This is consistent with our findings from studying lymphatic contraction using fluorescence microscopy.

Several mechanisms have been shown to alter the strength of lymphatic contraction. These include physical, neural and humoral influences (*20)*. In particular, nitric oxide concentrations are able to dictate lymphatic contraction frequency and amplitude (*24,48-50)*. Although we measured a marked increase in inflammatory cytokine production and nitric oxide-producing infiltrating cells at the peak of MRSA infection, we found that inhibition of host-derived nitric oxide and other inflammatory signaling mediators did not improve lymphatic function during MRSA infection. Several lines of evidence support this finding, including deletion of inducible nitric oxide synthesis in mice and nitric oxide synthase oxygenase in MRSA, each of which led to lymphatic dysfunction after infection that was comparable to their wild-type counterparts. Likewise, inhibition of the cyclooxygenase pathway and inflammatory cytokines did not improve lymphatic function. The absence of inflammatory molecules even though lymphatic function was still impaired after MRSA clearance suggested underlying damage to lymphatic vessels, perhaps established during the acute stage of infection. We reason that MRSA toxins might act to compromise lymphatic function.

From this study, we report a new mechanism of lymphatic impairment. *In vitro and in vivo,* we show that MRSA causes LMC cell death. These data suggest a causal connection between LMC loss and lymphatic dysfunction. We found the factor(s) that mediated LMC death to be

proteinaceous and *agr*-dependent. Using a proteomics approach, we identified and investigated several molecules capable of killing LMCs—alpha hemolysin, delta hemolysin and PSMalpha. Alpha hemolysin, delta hemolysin, and PSMs are positively regulated by the global regulatory quorum sensing system, agr (*46)*. Consistent with protection of LMCs from cytotoxicity *in vitro* and *in vivo*, animals infected with an *agr* null mutant exhibited normal lymphatic function.

In agreement with other studies, the PSM β-type peptides were less cytolytic (towards LMCs and SMCs in our study) than the α-type peptides (*51)*. Several PSMs are able to lyse a variety of eukaryotic cell types (*51)*. It has been proposed that this is due to membrane perturbation of cells in a receptor independent manner (*52)*. Alpha-hemolysin also showed the ability to kill LMCs *in vitro*, but this result did not translate to the mechanism of MRSA induced LMC death. Alpha-hemolysin is known to cause indiscriminate cell death at high concentrations (*53)*, and this may explain the discrepancy in our results with recombinant alpha hemolysin and mutants deficient in alpha hemolysin. Taken together, these results suggest that *agr*-dependent production of alpha hemolysin, delta hemolysin and PSMα cause LMC death. However, we cannot rule out synergism with other *agr*-controlled toxins in contributing to LMC death.

The death of LMCs and the apparent slow regeneration of LMCs **(Fig. 4c)** explain how lymphatic function can be impaired long after MRSA have been cleared and the toxins are no longer present in the system. Further, the coupling of slow LMC regeneration with MRSA recurrence may explain the cyclical pattern of lymphatic deterioration and reinfection in some SSTI patients. Investigations into therapeutic approaches to accelerate LMC regeneration are needed and may provide an alternative treatment to restore lymphatic function in patients with recurrent SSTIs.

The identification of a bacterial-derived mechanism for LMC death represents a critical first step in mechanistic analyses of how MRSA impairs lymphatic function. However, more work is needed to understand lymphatic muscle regeneration and whether altered LMC morphology after infection is indicative of functional differences compared to LMCs of uninfected mice. We also cannot rule out an effect on lymphatic endothelial cells *in vivo*, which also contribute to the maintenance of lymphatic pumping. However, targeting *agr* signaling may overcome the cell-specific and compensatory effects of individual MRSA toxins to improve lymphatic function and immunity.

Although the ability to evaluate lymphatic vessel function in MRSA-infected mice provides significant insight into the effect of MRSA post-infection, our model is limited in that it is not a recurrent model of infection. Animals are maintained in a controlled sterile environment and mice do not develop secondary chronic lymphedema. Another limitation of this study is that it does not address a role, if any, for *Streptococci* and methicillin susceptible *S.aureus* (MSSA) on lymphatic impairment, as Group A Streptococci and MSSA are also common pathogens associated with SSTIs (*4)*. It is likely that MSSA can blunt lymphatic function through agr-mediated toxin production, albeit MSSA toxin production is lower than that of MRSA (*44)*.

In lymphedema patients, recurring episodes of SSTIs lead to further damage of the lymphatic system, resulting in lymph flow deterioration (*54)*. Emerging evidence suggests both T and B lymphocyte-mediated adaptive immune responses are generated after *S. aureus* infection *(55)*. In patients with pre-existing lymphedema or progressive lymphedema as a result of recurring infections, we expect local immune deficiency due to the ineffective transport of antigen to the

local draining lymph nodes, representing another mechanism by which *S. aureus* inhibits the adaptive immune responses to its advantage. When lymphatic function is impaired, the protein-rich and stagnant lymphatic fluid may facilitate bacterial growth. Further, impaired lymphatic function also inhibits bacterial clearance through the lymphatic system, resulting in bacterial and toxin accumulation that will impair both innate and adaptive immunity and increase the risk of recurrent infections.

Our data provide a mechanistic framework for the chronic reduction of lymph flow in patients after MRSA infection. Neutralization of MRSA pathogenicity as part of the treatment of MRSA-induced cellulitis may help intervene in the vicious cycle of SSTI, lymph flow deterioration, lymphedema and recurrent infection in these patients.

Materials and Methods

Study design

The goal of this study was to determine the effect of MRSA infection on lymphatic vessel function. Using a model of community-associated MRSA infection in the hindlimb, we assessed lymphatic function by performing lymphatic contraction experiments previously established (24,33). We deemed a 25% difference in lymphatic pumping or lymph flow with an anticipated standard deviation of 20% as biologically significant. At an alpha=0.05 and a beta of 0.80, we determined sample size based on prior and gained experience regarding the success rate of lymphatic pumping and lymph flow, respectively. No animals were excluded from lymphatic contraction studies pending successful surgical exposure of lymphatic vessel. The criteria for exclusion of animals for lymph flow experiments are described in the materials and methods and involved the ability to obtain a clear image of the vessel and calculate a Doppler angle of less than 85 degrees. αSMA-DsRed transgenic mice were visualized and immunofluorescence staining of αSMA^{+} lymphatic muscle cells of WT mice was performed to analyze LMC coverage of lymphatic vessels on multiple days post-infection. Each analysis represents a terminal experiment, not a longitudinal study of the same animal. Researchers were blinded to the details of the infection during image analysis. Both male and female mice were used and were age-matched between all comparator groups. Cell viability and cell lysis assays were used to measure killing of LMCs, hSMCs, mSMCs, and LECs by MRSA-conditioned supernatant from strain (s) simultaneously grown overnight in similar conditions. Cell culture experiments to investigate the effects of MRSA-conditioned supernatant or recombinant *S. aureus* toxins on cells were performed in duplicate or triplicate in three to five independent experiments. All data are presented as means ± SEM, unless stated otherwise in the figure legend. The methods used to support these findings are described in the Materials and Methods/Supplementary Materials and Methods. Statistical tests used to establish significance and associated *p* values are described in the figure legends.

Animals

In vivo studies were initiated in 5-8 week old male and female C57BL/6, $iNOS^{-/-}$ C57BL/6, MyD88-$^{-/-}$C57BL/6 (generous gift from Dr. Alessio Fassano), $LysM^{gfp/gfp}$ C57BL/6 mice (generous gift from Dr. Thomas Graf) and αSMA^{P}-DsRed/C57BL/6 mice. All mice were bred and maintained in our Cox-7 gnotobiotic animal colony or at the Center for Comparative Medicine and Animal Laboratory Resources at Massachusetts General Hospital. All procedures were performed following the guidelines of the Institutional Animal Care and Use Committee of the Massachusetts General Hospital.

***S. aureus* strains**
The clinical MRSA isolate, CA-MRSA USA300 LAC, had 3 non-essential plasmids removed to create the CA-MRSA USA300 JE2 strain (*56)*. Additionally, the NE27 mutant was created by mutagenesis from *mariner*-based transposon *bursa aurealis* resulting in an erythromycin-resistant deletion strain of JE2. Both isolates were obtained from the Network on Antimicrobial Resistance in *Staphylococcus aureus* (NARSA; Chantilly, VA). Wild type and isogenic deletion mutants of the *agr* regulatory system, alpha hemolysin, delta hemolysin, psmα, psmβ, and psmαβhld (TKO) in the LAC (USA300) strain, are described previously (*44,46,57-59)*.

Infection
MRSA strains were subcultured until they reached their exponential growth phase, washed with sterile PBS once and resuspended in sterile PBS. Mice were anesthetized with ketamine/xylazine (10/100 mg/kg i.p.). Fur was shaven from the hindlimb. 2-4 x 10^6 c.f.u. of MRSA were injected subcutaneously (using a 29 gauge 1/2" insulin syringe) into the hindlimb, proximal to the ankle, in a 50µL volume of sterile PBS. A similar procedure was performed with lipoteichoic acid (Invivogen, Cat # tlrl-pslta) after resuspension in sterile PBS.

Isolation of murine lymphatic muscle cells and blood smooth muscle cells
While in solution of Hanks Balanced Saline Solution, fat and surrounding connective tissue were removed from the posterior tibial artery and adjacent afferent lymphatic vessels to the popliteal lymph node. To make 5 mL of enzyme solution, Collagenase Type II and Soybean Trypsin Inhibitor (Worthington) were added to Hanks Balanced Saline Solution at 1 mg/mL. 35µL of elastase (Worthington) and 50 µL Penicillin/Streptomycin were added. Next, enzyme solution was added to minced fragments of popliteal artery or lymphatic vessels and allowed to incubate at 37°C, 5% CO_2 for 4 hours with occasional agitation. Cell outgrowth was allowed to proceed for 5 days.

Preparation of MRSA-Conditioned supernatant
Planktonic culture-conditioned medium was prepared by growing an overnight culture of indicated MRSA strain in Trypticase Soy Broth (TSB; BD Biosciences, Franklin Lakes, NJ, USA) under shaking conditions (200 rpm) at 37°C for 12-18 hrs. Afterwards, the bacteria were centrifuged at 6,000 rpm for 10 min and subsequently the supernatant was filtered through a 0.22-µm pore-size PES filter (Olympus Plastics) to produce cell-free conditioned medium.
The cell-free conditioned MRSA medium was mixed at a 1:1 dilution with muscle cell culture medium. 1:1 dilution of cell culture medium with TSB medium as a control was performed in parallel. Where indicated, MRSA-conditioned medium was treated with 0.0625% trypsin (final percentage in solution) for 18-24 h at 37°C to degrade proteins. Trypsin was heat-inactivated at 100°C for one hour and allowed to cool to room temperature before supernatant was incubated with cells.

Lymphatic contraction model
Mice were anesthetized with ketamine/xylazine (10/100 mg/kg i.p.) and 3 µL of 2% FITC-Dextran (2 million molecular weight; ThermoFisher Scientific Cat. #D7137) was interstitially injected in the footpad. Surgical preparation and intravital imaging were performed as described (*24,32)*. Briefly, the leg skin and underlying connective tissue near the afferent lymphatic vessel to the

popliteal lymph node (PLV) were carefully excised. Time-lapse images (360 images separated by 210 ms) of the exposed afferent lymphatic vessels to the popliteal lymph node were captured while imaging with an inverted fluorescence microscope. For each mouse, we imaged two to three lymphatic segments and took images every 15 minutes for four time points. Using in-house MATLAB codes, time-lapse images were analyzed to track the position of the vessel wall and frequency measured using the peak-and-valley method as described previously (*24,32)*. We used average results collected from a single mouse to represent the lymphatic contraction parameters for that animal.

Measuring lymphatic flow

To measure lymph flow inside murine collecting lymphatic vessels, we employed a recently developed label-free method for directly measuring lymph flow velocity *in vivo* by Doppler optical coherence tomography (DOCT) (*33)*. This technique measures the velocity of lymph fluid, both basal and pulsatile, and relies only upon the absolute movement of lymph relative to the laser beam. Mice were anesthetized with Ketamine/Xylazine (100 mg/10 mg per Kg body weight). The surgical procedure to expose the PLV was performed as described previously (*24,32)*. Anesthetized mice were transferred *to a heating pad to maintain* body *temperature* at 37°C.

Hydration of the PLV and surrounding tissue was maintained with physiological saline while measuring lymph flow. Repeated five-minute DOCT measurements are acquired from a fixed location within a lymphangion, in between lymphatic valves. Next, the measurements are processed to produce a structural image and the scattering signals within the lymphatic vessel are analyzed using an algorithm designed specifically to measure the lymph flow signal. Three-dimensional imaging is used to measure the lymphatic vessel orientation and thereby the Doppler angle of the flow, the latter being mandatory to calculate flow speed (from Doppler shift). For these measurements, a structural image showing clear vessel-tissue boundary and absence of signal artifact within the vessel lumen is of paramount importance. In addition, a Doppler angle less than 85 degrees and a lymphatic vessel within 100 microns from the tissue surface are needed to guarantee trustworthy results. Data not adhering to these criteria were excluded for analysis.

Twenty-four 8-12 week old C57BL/6 female mice were infected with 2-4 x 10^6 c.f.u. of MRSA-USA 300 JE2 and lymphatic flow was measured at either four days (n=8), 35 days (n=16) or 260 days after infection (n=7). Eight mice served as uninfected controls. Lymphatic flow was measured using M-Mode acquisition until two measurements per mouse were obtained without consequential x, y or z drift, as judged by the investigators. Mouse limbs were positioned lower than the abdomen on a 15 degree tilted stage and measurements were acquired and subsequently analyzed as described previously (*33)*. In the control group 19/25 measurements were successful in 6/8 mice. Out of eight mice four days after CA-MRSA infection, four could not be imaged due to excessive postoperative bleeding resulting from severe inflammation during active bacterial infection. In the remaining four mice, 3/13 measurements were successful, all from the same mouse. Our experience shows the limitations of DOCT imaging during acute bacterial infection. After 35 days, 17/46 measurements were successful in 6/12 mice. In this group, four mice did not show intact collecting vessels within 100 microns from the tissue surface and therefore no measurements could be acquired.

Cell viability assays
10,000-20,000 hSMCs or 1,000-5000 mLMCs, delivered in 200 µl of respective media were allowed to adhere overnight to the bottom of a 48-well plate. After 24 to 48 hours of exposure to MRSA-conditioned supernatant or TSB, the CellTiter-Glo® Luminescent Cell Viability Assay (Promega) was performed according to instructions. Briefly, 100µl of medium was removed from the wells of the plates containing medium, and 100µl of room temperature CellTiter-Glo® Reagent was added. Plates were rocked for two minutes in the dark and incubated for an additional eight minutes or longer (while protected from light) before reading luminescent output on an FLUOstar® Omega series luminescence microplate reader.

Statistical Methods
Statistical analyses were completed with Prism 7 (Graph- Pad, San Diego, CA, USA). Statistical significance was determined with either a one-way analysis of variance (ANOVA) with the Fisher's Least Significance Difference post hoc test, or two-tailed unpaired Student's *t* test, as appropriate. Statistical significance was set at $p < .05$. All statistical tests were two-sided.

Acknowledgements: We sincerely thank Dr. Jean C. Lee of Harvard Medical School for critical discussion and Julie Bubeck-Wardenburg of the University of Chicago for generously supplying the alpha hemolysin mutant MRSA strain. We also thank Janssen Biotech, Inc. for contributing the blocking anti-TNFα mAb. We thank the Harvard University Mass Spectrometry and Proteomics Resource Laboratory for sample analysis.

Funding: This work was supported by the National Institutes of Health under award numbers R21AI097745 (TPP), DP2OD008780 (TPP), R01CA214913 (TPP) and R01HL128168 (TPP, LLM). Research reported in this publication was supported in part by the Center for Biomedical OCT Research and Translation through Grant Number P41EB015903, awarded by the National Institute of Biomedical Imaging and Bioengineering of the National Institutes of Health. This work as supported in part by the National Cancer Institute Federal Share of Proton Income CA059267 (TPP, BJV), National Cancer Institute R01CA163528 (BJV), Massachusetts General Hospital Executive Committee on Research ISF (TPP), and the Intramural Research Program of the National Institute of Allergy and Infectious Diseases Grant Number ZIA AI000904-16 (MO). This work was also supported in part by the UNCF-Merck Science Initiative Postdoctoral Fellowship (DJ), Burroughs Wellcome Fund Postdoctoral Enrichment Program Award (DJ), NIH NCI F32CA183465 (DJ) and the Swiss National Science Foundation (CB).

Author Contributions: D.J. and T.P.P. conceived and designed the study and analyzed data. D.J., E.F.J.M., E.P., E.B., K.J. and S.M.C. designed and performed experiments and analyzed data. C.B. and B.J.V. conducted imaging analyses and contributed imaging tools. P.H. contributed αSMA^{P}-DsRed/C57BL/6 mice. S.L. and L.L.M. contributed to the development of imaging tools. M.O. contributed MRSA strains and data interpretation. D.J. and T.P.P. wrote the manuscript, which all coauthors commented on.

Competing Financial Interests: None

References

1. Zheng, W., A. Aspelund, and K. Alitalo, Lymphangiogenic factors, mechanisms, and applications. J Clin Invest, 2014. 124(3): p. 878-87.
2. Banerji, S., et al., LYVE-1, a new homologue of the CD44 glycoprotein, is a lymph-specific receptor for hyaluronan. J Cell Biol, 1999. 144(4): p. 789-801.
3. Wigle, J.T. and G. Oliver, Prox1 function is required for the development of the murine lymphatic system. Cell, 1999. 98(6): p. 769-78.
4. Martinez-Corral, I., et al., Nonvenous origin of dermal lymphatic vasculature. Circ Res, 2015. 116(10): p. 1649-54.
5. Yang, Y. and G. Oliver, Development of the mammalian lymphatic vasculature. J Clin Invest, 2014. 124(3): p. 888-97.
6. Zawieja, D.C., Contractile physiology of lymphatics. Lymphat Res Biol, 2009. 7(2): p. 87-96.
7. Iliff, J.J., et al., A Paravascular Pathway Facilitates CSF Flow Through the Brain Parenchyma and the Clearance of Interstitial Solutes, Including Amyloid β. Sci Transl Med, 2012. 4(147): p. 147ra111.
8. Li, J., et al., Efficacy of B cell depletion therapy for murine joint arthritis flare is associated with increased lymphatic flow. Arthritis Rheum, 2013. 65(1): p. 130-8.
9. Aspelund, A., et al., The Schlemm's canal is a VEGF-C/VEGFR-3–responsive lymphatic-like vessel. The Journal of Clinical Investigation, 2014. 124(9): p. 3975-3986.
10. Wiig, H., et al., Immune cells control skin lymphatic electrolyte homeostasis and blood pressure. The Journal of Clinical Investigation, 2013. 123(7): p. 2803-2815.
11. Klotz, L., et al., Cardiac lymphatics are heterogeneous in origin and respond to injury. Nature, 2015. 522(7554): p. 62-67.
12. Hoshida, T., et al., Imaging steps of lymphatic metastasis reveals that vascular endothelial growth factor-C increases metastasis by increasing delivery of cancer cells to lymph nodes: therapeutic implications. Cancer Res, 2006. 66(16): p. 8065-75.
13. Dieterich, L.C., C.D. Seidel, and M. Detmar, Lymphatic vessels: new targets for the treatment of inflammatory diseases. Angiogenesis, 2014. 17(2): p. 359-71.
14. Skobe, M., et al., Induction of tumor lymphangiogenesis by VEGF-C promotes breast cancer metastasis. Nat Med, 2001. 7(2): p. 192-8.
15. Mortimer, P.S. and S.G. Rockson, New developments in clinical aspects of lymphatic disease. J Clin Invest, 2014. 124(3): p. 915-21.
16. Hos, D., et al., Antilymphangiogenic therapy to promote transplant survival and to reduce cancer metastasis: what can we learn from the eye? Semin Cell Dev Biol, 2015. 38: p. 117-30.
17. Goel, S., et al., Effects of vascular-endothelial protein tyrosine phosphatase inhibition on breast cancer vasculature and metastatic progression. J Natl Cancer Inst, 2013. 105(16): p. 1188-201.
18. Pereira, E.R., et al., The lymph node microenvironment and its role in the progression of metastatic cancer. Semin Cell Dev Biol, 2015. 38: p. 98-105.
19. Card, C.M., S.S. Yu, and M.A. Swartz, Emerging roles of lymphatic endothelium in regulating adaptive immunity. J Clin Invest, 2014. 124(3): p. 943-52.
20. Tewalt, E.F., et al., Lymphatic endothelial cells induce tolerance via PD-L1 and lack of costimulation leading to high-level PD-1 expression on CD8 T cells. Blood, 2012. 120(24): p. 4772-82.

21. Teijeira, A., E. Russo, and C. Halin, Taking the lymphatic route: dendritic cell migration to draining lymph nodes. Semin Immunopathol, 2014. 36(2): p. 261-74.
22. Baluk, P., et al., Functionally specialized junctions between endothelial cells of lymphatic vessels. J Exp Med, 2007. 204(10): p. 2349-62.
23. Schmid-Schonbein, G.W., Microlymphatics and lymph flow. Physiological Reviews, 1990. 70(4): p. 987-1028.
24. Witte, M.H., et al., Lymphangiogenesis and lymphangiodysplasia: from molecular to clinical lymphology. Microsc Res Tech, 2001. 55(2): p. 122-45.
25. Pflicke, H. and M. Sixt, Preformed portals facilitate dendritic cell entry into afferent lymphatic vessels. J Exp Med, 2009. 206(13): p. 2925-35.
26. Randolph, G.J., V. Angeli, and M.A. Swartz, Dendritic-cell trafficking to lymph nodes through lymphatic vessels. Nat Rev Immunol, 2005. 5(8): p. 617-28.
27. Schumann, K., et al., Immobilized chemokine fields and soluble chemokine gradients cooperatively shape migration patterns of dendritic cells. Immunity, 2010. 32(5): p. 703-13.
28. Miteva, D.O., et al., Transmural flow modulates cell and fluid transport functions of lymphatic endothelium. Circ Res, 2010. 106(5): p. 920-31.
29. Weber, M., et al., Interstitial dendritic cell guidance by haptotactic chemokine gradients. Science, 2013. 339(6117): p. 328-32.
30. von der Weid, P.Y. and D.C. Zawieja, Lymphatic smooth muscle: the motor unit of lymph drainage. Int J Biochem Cell Biol, 2004. 36(7): p. 1147-53.
31. Davis, M.J., et al., Determinants of valve gating in collecting lymphatic vessels from rat mesentery. Am J Physiol Heart Circ Physiol, 2011. 301(1): p. H48-60.
32. Skalak, T.C., G.W. Schmid-Schonbein, and B.W. Zweifach, New morphological evidence for a mechanism of lymph formation in skeletal muscle. Microvasc Res, 1984. 28(1): p. 95-112.
33. Eisenhoffer, J., et al., Importance of valves and lymphangion contractions in determining pressure gradients in isolated lymphatics exposed to elevations in outflow pressure. Microvasc Res, 1995. 49(1): p. 97-110.
34. Gasheva, O.Y., D.C. Zawieja, and A.A. Gashev, Contraction-initiated NO-dependent lymphatic relaxation: a self-regulatory mechanism in rat thoracic duct. J Physiol, 2006. 575(Pt 3): p. 821-32.
35. Margaris, K.N. and R.A. Black, Modelling the lymphatic system: challenges and opportunities. J R Soc Interface, 2012. 9(69): p. 601-12.
36. Baxter, L.T. and R.K. Jain, Transport of fluid and macromolecules in tumors. I. Role of interstitial pressure and convection. Microvasc Res, 1989. 37(1): p. 77-104.
37. Roose, T. and M.A. Swartz, Multiscale modeling of lymphatic drainage from tissues using homogenization theory. J Biomech, 2012. 45(1): p. 107-15.
38. Hagendoorn, J., et al., Endothelial nitric oxide synthase regulates microlymphatic flow via collecting lymphatics. Circ Res, 2004. 95(2): p. 204-9.
39. Liao, S., et al., Method for the quantitative measurement of collecting lymphatic vessel contraction in mice. J Biol Methods, 2014. 1(2).
40. Robinson, H.A., et al., Non-invasive Optical Imaging of the Lymphatic Vasculature of a Mouse. J Vis Exp, 2013(73).
41. Rahimi, H., et al., Lymphatic imaging to assess rheumatoid flare: mechanistic insights and biomarker potential. Arthritis Res Ther, 2016. 18: p. 194.

42. Sevick-Muraca, E.M., S. Kwon, and J.C. Rasmussen, Emerging lymphatic imaging technologies for mouse and man. J Clin Invest, 2014. 124(3): p. 905-14.
43. Proulx, S.T., et al., Use of a PEG-conjugated bright near-infrared dye for functional imaging of rerouting of tumor lymphatic drainage after sentinel lymph node metastasis. Biomaterials, 2013. 34(21): p. 5128-37.
44. Chong, C., et al., In vivo visualization and quantification of collecting lymphatic vessel contractility using near-infrared imaging. Sci Rep, 2016. 6: p. 22930.
45. Liao, S., et al., Impaired lymphatic contraction associated with immunosuppression. Proc Natl Acad Sci U S A, 2011. 108(46): p. 18784-9.
46. Brandon Dixon, J. and M.J. Weiler, Bridging the divide between pathogenesis and detection in lymphedema. Semin Cell Dev Biol, 2015. 38: p. 75-82.
47. Tiwari, P., et al., Breast and gynecologic cancer-related extremity lymphedema: a review of diagnostic modalities and management options. World J Surg Oncol, 2013. 11: p. 237.
48. Cady, B., Regional lymph node metastases; a singular manifestation of the process of clinical metastases in cancer: contemporary animal research and clinical reports suggest unifying concepts. Ann Surg Oncol, 2007. 14(6): p. 1790-800.
49. Fisher, B., et al., Twenty-five-year follow-up of a randomized trial comparing radical mastectomy, total mastectomy, and total mastectomy followed by irradiation. N Engl J Med, 2002. 347(8): p. 567-75.
50. Halsted, W.S., I. The Results of Radical Operations for the Cure of Carcinoma of the Breast. Ann Surg, 1907. 46(1): p. 1-19.
51. Cascinelli, N., et al., Immediate or delayed dissection of regional nodes in patients with melanoma of the trunk: a randomised trial. WHO Melanoma Programme. Lancet, 1998. 351(9105): p. 793-6.
52. Starz, H., et al., A micromorphometry-based concept for routine classification of sentinel lymph node metastases and its clinical relevance for patients with melanoma. Cancer, 2001. 91(11): p. 2110-21.
53. Clarke, M., et al., Effects of radiotherapy and of differences in the extent of surgery for early breast cancer on local recurrence and 15-year survival: an overview of the randomised trials. Lancet, 2005. 366(9503): p. 2087-106.
54. Falkson, C.B., How do I deal with the axilla in patients with a positive sentinel lymph node? Curr Treat Options Oncol, 2011. 12(4): p. 389-402.
55. Morton, D.L., et al., Final trial report of sentinel-node biopsy versus nodal observation in melanoma. N Engl J Med, 2014. 370(7): p. 599-609.
56. Hellman, S., Karnofsky Memorial Lecture. Natural history of small breast cancers. J Clin Oncol, 1994. 12(10): p. 2229-34.
57. Podgrabinska, S. and M. Skobe, Role of lymphatic vasculature in regional and distant metastases. Microvasc Res, 2014. 95C: p. 46-52.
58. Stacker, S.A., et al., Lymphangiogenesis and lymphatic vessel remodelling in cancer. Nat Rev Cancer, 2014. 14(3): p. 159-72.
59. Padera, T.P., et al., Lymphatic metastasis in the absence of functional intratumor lymphatics. Science, 2002. 296(5574): p. 1883-6.
60. Karpanen, T., et al., Vascular endothelial growth factor C promotes tumor lymphangiogenesis and intralymphatic tumor growth. Cancer Res, 2001. 61(5): p. 1786-90.

61. Stacker, S.A., et al., VEGF-D promotes the metastatic spread of tumor cells via the lymphatics. Nat Med, 2001. 7(2): p. 186-91.
62. Padera, T.P., et al., Differential response of primary tumor versus lymphatic metastasis to VEGFR-2 and VEGFR-3 kinase inhibitors cediranib and vandetanib. Mol Cancer Ther, 2008. 7(8): p. 2272-9.
63. Issa, A., et al., Vascular endothelial growth factor-C and C-C chemokine receptor 7 in tumor cell-lymphatic cross-talk promote invasive phenotype. Cancer Res, 2009. 69(1): p. 349-57.
64. Gogineni, A., et al., Inhibition of VEGF-C modulates distal lymphatic remodeling and secondary metastasis. PLoS One, 2013. 8(7): p. e68755.
65. Karnezis, T., et al., VEGF-D promotes tumor metastasis by regulating prostaglandins produced by the collecting lymphatic endothelium. Cancer Cell, 2012. 21(2): p. 181-95.
66. Roberts, N., et al., Inhibition of VEGFR-3 activation with the antagonistic antibody more potently suppresses lymph node and distant metastases than inactivation of VEGFR-2. Cancer Res, 2006. 66(5): p. 2650-7.
67. Tammela, T., et al., Photodynamic ablation of lymphatic vessels and intralymphatic cancer cells prevents metastasis. Sci Transl Med, 2011. 3(69): p. 69ra11.
68. Barankay, T., et al., Oxygen pressure in small lymphatics. Pflugers Arch, 1976. 366(1): p. 53-9.
69. Hangai-Hoger, N., et al., Microlymphatic and tissue oxygen tension in the rat mesentery. Am J Physiol Heart Circ Physiol, 2004. 286(3): p. H878-83.
70. Jeong, H.S., et al., Investigation of the Lack of Angiogenesis in the Formation of Lymph Node Metastases. J Natl Cancer Inst, 2015. 107(9).
71. Arapandoni-Dadioti, P., et al., Angiogenesis in ductal breast carcinoma. Comparison of microvessel density between primary tumour and lymph node metastasis. Cancer Lett, 1999. 137(2): p. 145-50.
72. Naresh, K.N., A.Y. Nerurkar, and A.M. Borges, Angiogenesis is redundant for tumour growth in lymph node metastases. Histopathology, 2001. 38(5): p. 466-70.
73. Akita, H., et al., Effects of neoadjuvant chemotherapy on primary tumor and lymph node metastasis in esophageal squamous cell carcinoma: additive association with prognosis. Dis Esophagus, 2009. 22(4): p. 291-7.
74. Medich, D., et al., Preoperative chemoradiotherapy and radical surgery for locally advanced distal rectal adenocarcinoma: pathologic findings and clinical implications. Dis Colon Rectum, 2001. 44(8): p. 1123-8.
75. Kuerer, H.M., et al., Clinical course of breast cancer patients with complete pathologic primary tumor and axillary lymph node response to doxorubicin-based neoadjuvant chemotherapy. J Clin Oncol, 1999. 17(2): p. 460-9.
76. Cox, C., et al., What is the burden of axillary disease after neoadjuvant therapy in women with locally advanced breast cancer? Curr Oncol, 2013. 20(2): p. 111-7.

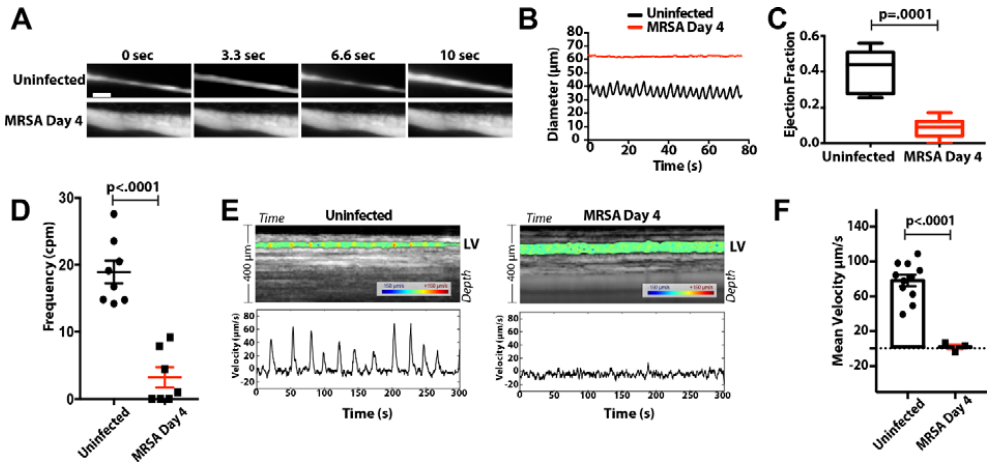

Fig. 1. Collecting popliteal lymphatic vessels exhibit diminished contraction and lymph velocity following MRSA infection.
C57BL/6 mice were infected subcutaneously in the hindlimb with 2-4 x 10^6 c.f.u. of MRSA for four days or left uninfected. **(A)** Representative sequential images from intravital microscopy of popliteal lymphatic vessels perfused with FITC Dextran 2 million MW (sec, seconds) **Scale bar**=50 µm (See Supplementary Movies 1 and 2). **(B)** Representative traces from lymphatic vessel wall measurements show lymphatic diameter and contraction over time (s,seconds). **(C)** Ejection fraction is related to the strength of lymphatic vessel contraction (n=8-12 each group). **(D)** Frequency indicates the cpm (counts per minute) of lymphatic vessel contractions in uninfected mice and mice infected with WT MRSA after 4 days (n=8-12 each group). **(E)** Top Panel: Representative depth vs. time image of the optical coherence tomography intensity signal (grayscale) from a fixed transverse location that is used to identify the upper and lower boundaries of lymphatic vessels in uninfected animals and during active infection (Day 4). LV, lymphatic vessel. Instantaneous lymph velocity (color) in the lymphatic vessel in uninfected animals and during active infection (Day 4) is overlaid on lymphatic vessels. Bottom Panel: Representative trace of instantaneous mean velocity of lymph flow averaged over the vessel cross-sectional area in uninfected animals and during active infection (Day 4). **(F)** Time-averaged mean velocity of lymph flow in uninfected animals and during active infection (n=3-11 measurements each group). For **C,D, and F,** statistical analysis was performed using Student's unpaired two-sided *t* test. Error bars show mean ± s.e.m.

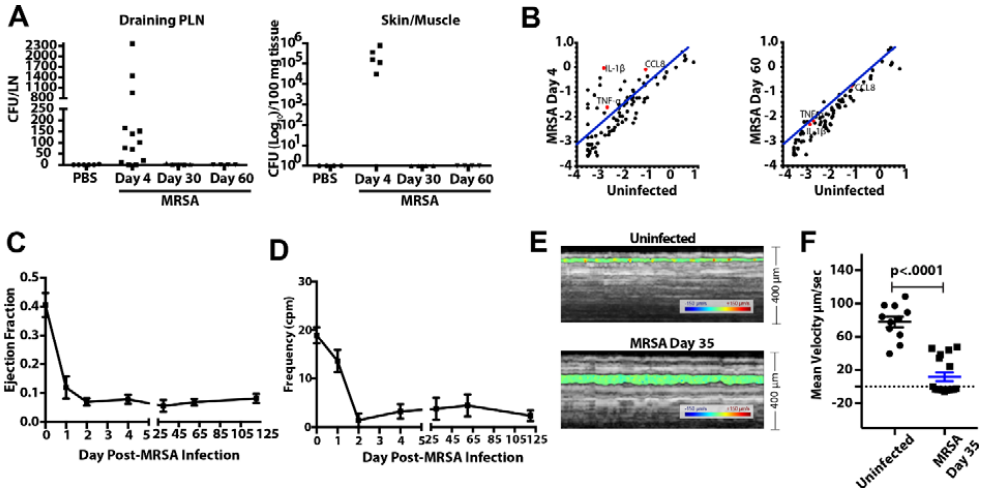

Fig. 2. Lymphatic vessel dysfunction persists after clearance of MRSA.
(A) Infectious burden measured by colony formation assay in the draining popliteal lymph node (left) at indicated time points (n=6-14 all groups). Infectious burden in the skin and underlying muscle tissue (right) from the site of infection at indicated time points (n=4-5 all groups). **(B)** Gene expression array of mouse inflammatory cytokines and receptors comparing tissue from the site of infection collected at day 4 (left) and 60 (right) post-MRSA infection. The graph plots normalized gene expression levels (log_{10}) from control (uninfected) skin and muscle tissue on the x-axis versus day 4 or day 60 post-infection on the y-axis. Black squares above the blue line identify up-regulated genes and black squares below the blue line indicate down-regulated genes. Individual samples were loaded into each qPCR array plate and normalized to skin from uninfected mice. **(C)** Ejection fraction and **(D)** frequency show the strength and number (counts per minute, cpm), respectively, of lymphatic vessel contractions over time (n=3-8/group at each time point representing a different cohort of mice; days 1, 2, 4, 30, 60 and 120 were measured). **(E)** Representative depth vs. time image of the depth-resolved optical coherence tomography intensity from a fixed transverse location that is used to identify the upper and lower boundaries of lymphatic vessels in uninfected animals and after clearance of infection (D35). Instantaneous lymph velocity (color) in the lymphatic vessel in uninfected animals and after clearance of infection (D35) is overlaid on lymphatic vessels. **(F)** Time-averaged mean velocity of lymph in uninfected animals and after clearance of infection (D35; n=11-17 measurements in each group). Statistical analysis was performed using Student's unpaired two-sided *t* test **(F)**. Error bars show mean ± s.e.m.

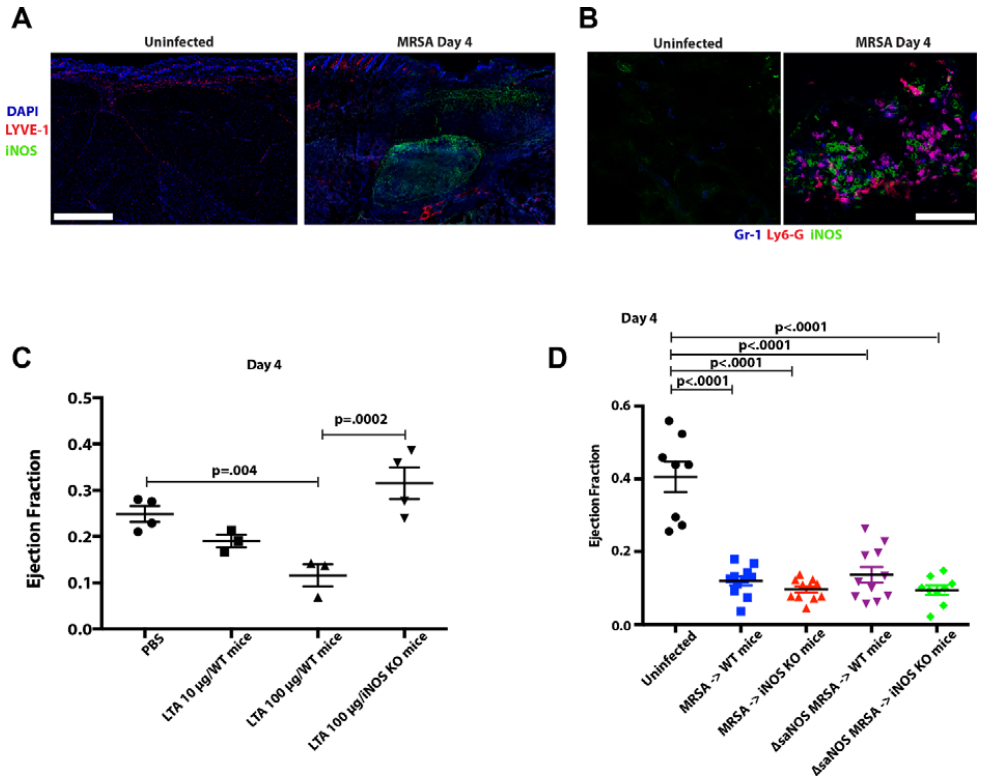

Fig. 3. Inhibition of iNOS is not sufficient to restore lymphatic vessel contraction during MRSA infection. **(A)** Representative sections of control skin (from uninfected mice) and skin 4 days post-MRSA infection. Lymphatic vessels were identified with anti-LYVE-1 antibody (**red**) and nuclei with DAPI (**blue**). Anti-iNOS antibody (**green)** identified iNOS-positive cells. **Scale bar**=300 µm. **(B)** Serial sections to the images in **(A)** was stained with anti-Gr-1 antibody (**blue**), anti-iNOS antibody (**green**) and anti-Ly6G antibody (**red**). **Scale bar**=50 µm. **(C)** 50 µL of sterile PBS or 50 µL of lipoteichoic acid (LTA) suspended in sterile PBS was injected into the hindlimb of C57BL/6 mice and C57BL/6-iNOS$^{-/-}$ mice. On day 4 post-injection, the ejection fraction shows the strength of lymphatic vessel contraction from indicated concentrations of LTA (n=3-4 each group). **(D)** C57BL/6 mice were injected subcutaneously in the hindlimb with PBS (uninfected) or infected subcutaneously in the hindlimb with 2-4 x 10^6 c.f.u. of WT MRSA or MRSA deficient in nitric oxide production (ΔsaNOS). C57BL/6-iNOS$^{-/-}$ mice were infected subcutaneously in the hindlimb with 2-4 x 10^6 c.f.u. of WT MRSA or ΔsaNOS MRSA. Ejection fraction four days after infection shows the strength of lymphatic vessel contraction among respective groups (n=8-11 each group). For **C, and D,** One-Way ANOVA comparison with Fisher's least significant difference (LSD) post-hoc analysis was used to determine significance. Error bars show mean ± s.e.m.

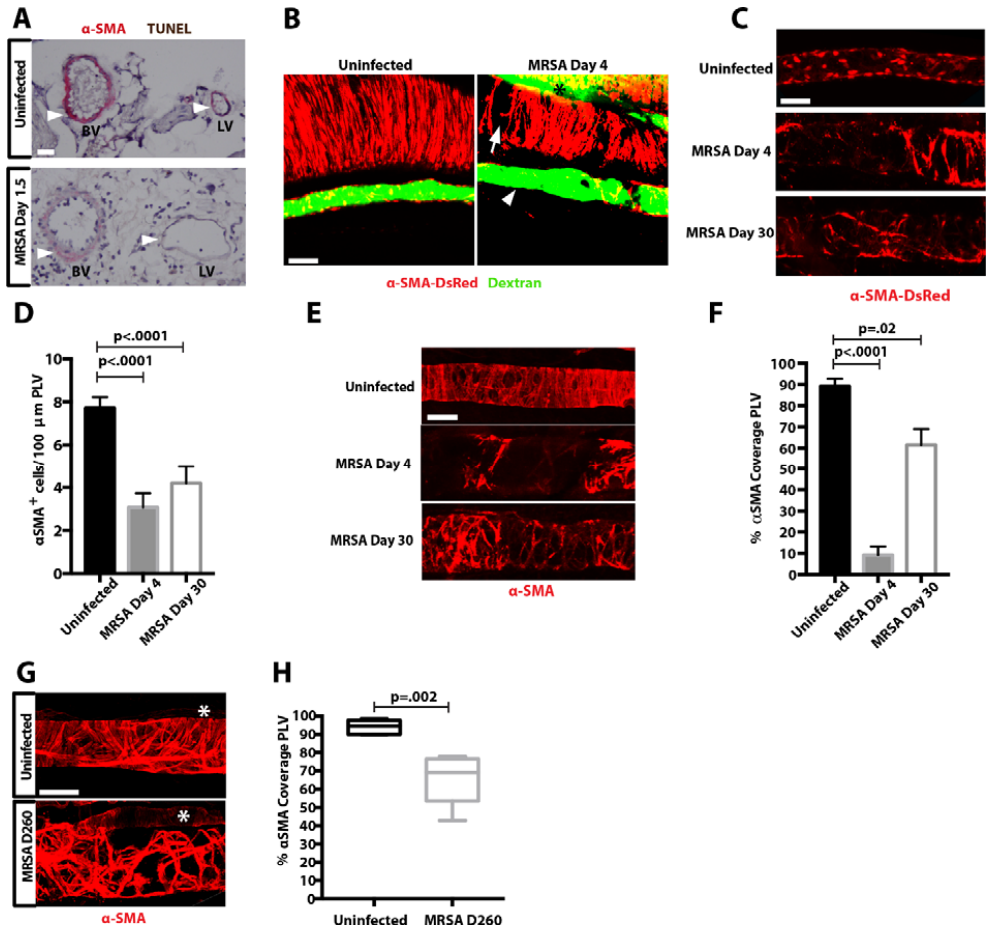

Fig. 4. Infection-induced lymphatic dysfunction is associated with decreased coverage of lymphatic muscle cells. **(A)** Representative immunohistochemical images of mouse hindlimb stained with αSMA (crimson, arrowhead) and TUNEL (brown). There were no TUNEL-positive cells in these sections, in contrast to the positive control (see SFig. 6b). **Scale bar**=40 µm **(B)** Representative intravital image from segment of PLV of an αSMA^{P}DsRed/C57BL/6 mouse interstitially injected with FITC Dextran (2 million MW). Asterisk indicates site of FITC-dextran leakage. Arrowhead indicates regional absence of lymphatic muscle cells. Arrow indicates regional absence of smooth muscle cells on blood vessels. **Scale bar**=100 µm **(C)** Representative intravital image from PLV segments of αSMA^{P}DsRed/C57BL/6 mice on indicated days. **Scale bar**=100 µm. **(D)** Quantification of αSMA-positive cells per 100 µM of PLV; n=8 mice (control, uninfected); n=6 mice (day 4 and day 30). **(E)** Representative image from PLV segments of C57BL/6 mice, stained with anti-αSMA, on indicated days. **Scale bar**=100 µm. **(F)** Computer-automated quantification of % αSMA-positive area of PLV; n=3-4 mice for each group. **(G)** Representative image from a segment of PLV stained with anti-αSMA (**red**) 260 days post-infection and corresponding control (contralateral) PLV. **Scale bar**=25 µm. Asterisk indicates adjacent blood vessel (posterior tibial artery). **(H)** Computer-automated quantification of % αSMA coverage of PLV 260 days post-infection or corresponding age matched control (contralateral) popliteal lymphatic vessel (n=5 both groups).

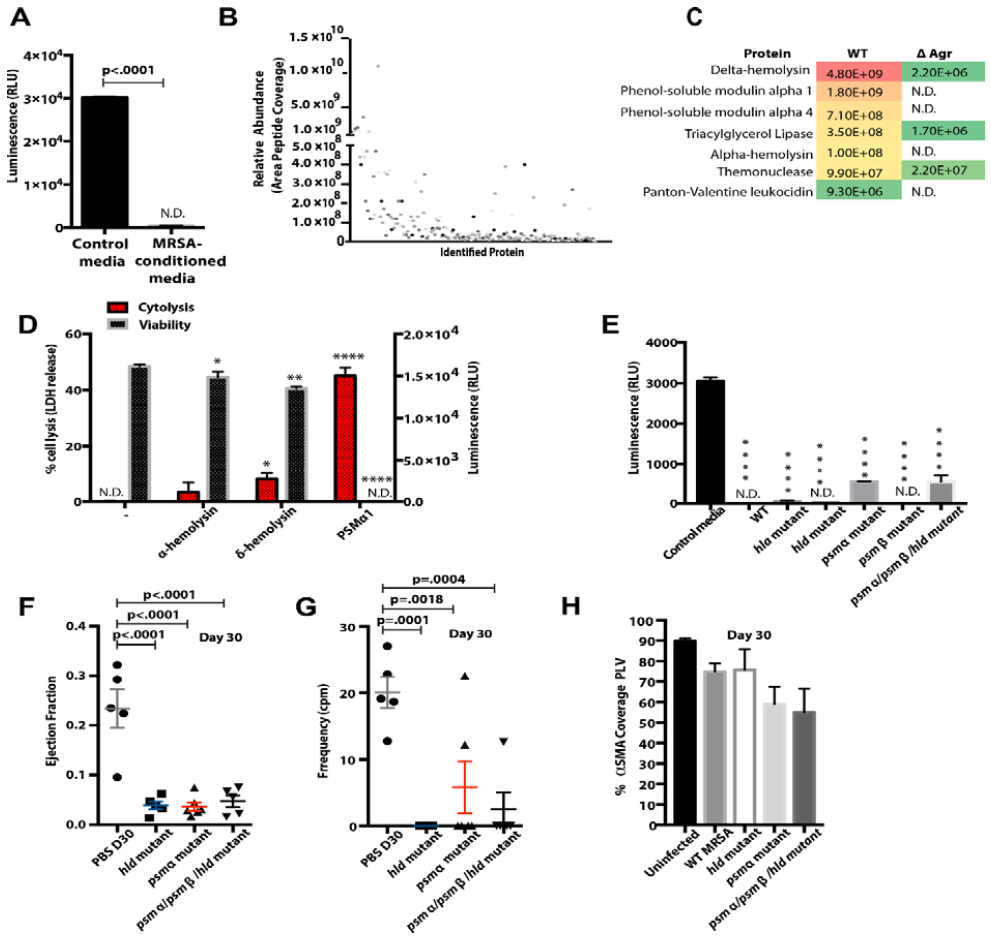

Fig. 5. Effect of MRSA toxins on lymphatic muscle cells and lymphatic function.
(A) Mouse lymphatic muscle cell (LMC) viability analysis (RLU, relative luciferase units) after exposure for 24 hours to control media (tryptic soy broth), or MRSA-conditioned media. **(B)** Identification by mass spectrometry of the relative abundance of proteins (area) from <100 kDa fraction of MRSA-conditioned media. **(C)** Heat map of the most highly expressed toxins, as identified by mass spectrometry; also depicted is the corresponding toxin expression level in the absence of the accessory gene regulator (*agr*). **(D)** Graph depicting lactate dehydrogenase (LDH) release from LMCs (left Y-axis) and cell viability (RLU, relative luciferase units (right Y-axis)) after incubation for 24 hours with normal growth media only (-) α-hemolysin (1.0 μg/mL), δ-hemolysin (100 μg/mL), or PSMα1 (100 μg/mL). * p <.05; ** p< .001, **** p< .001 relative to untreated control for cytolysis and cell viability, respectively. **(E)** Cell viability analysis (RLU, relative luciferase units) of murine lymphatic muscle cells after exposure for 24 hours to control media (tryptic soy broth), MRSA-conditioned media or conditioned media of isogenic MRSA mutants, as indicated. Asterisks indicate p <.0001 relative to control media. hla=alpha hemolysin, hld=delta hemolysin. **(F)** Lymphatic ejection fraction and **(G)** frequency of lymphatic vessel contractions was measured in mice infected with wild type or indicated mutant MRSA strains. **(H)** Computer-automated quantification of % αSMA-positive area of PLV in animals 30 days post infection with wild type or indicated mutant MRSA strain; n=3-4 mice for each group. For **E-H,** statistical analysis was performed by One-Way ANOVA comparison with Fisher's Least Significance Difference post-hoc analysis. Error bars show mean ± s.e.m.

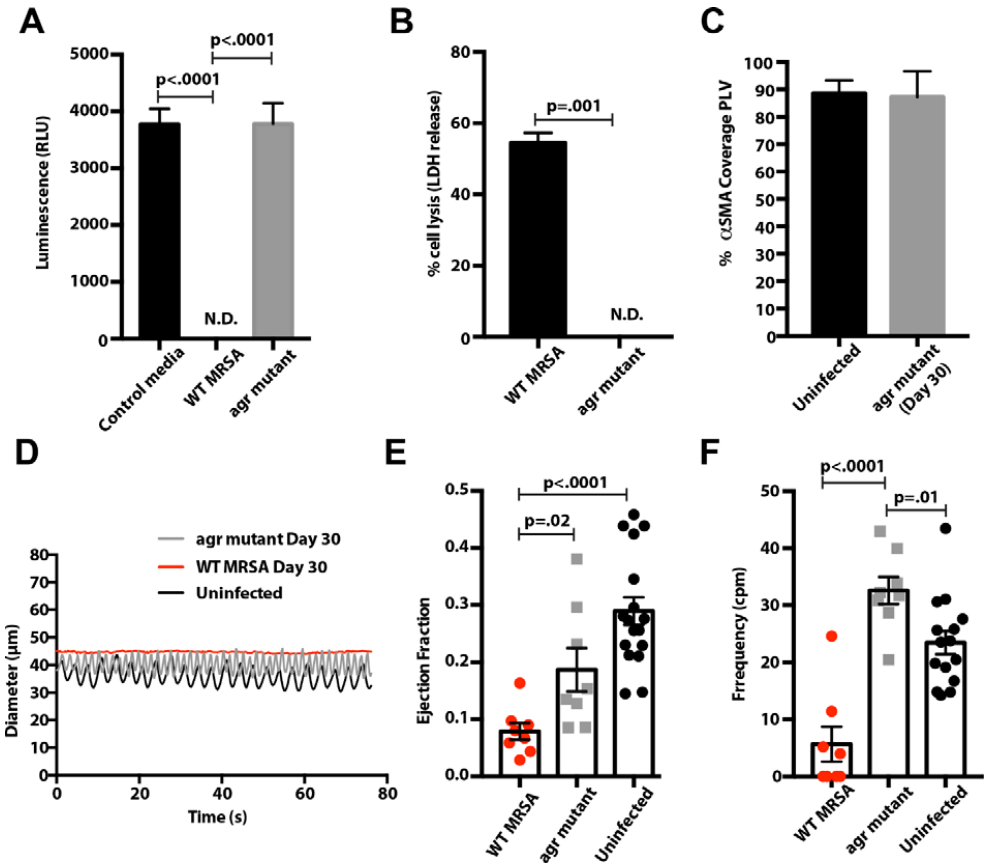

Fig. 6. MRSA virulence proteins cause lymphatic muscle cell death and diminished lymphatic function.
(A) Mouse lymphatic muscle cell (LMC) viability analysis (RLU, relative luciferase units) after exposure for 24 hours to control media (tryptic soy broth), *agr* mutant-conditioned media or MRSA-conditioned media. **(B)** Lactate dehydrogenase (LDH) release from LMCs incubated with conditioned medium from WT or *agr* mutant MRSA. **(C)** Computer-automated quantification of % αSMA-positive area of PLV in uninfected animals and animals 30 days post-*agr*-mutant MRSA infection; n=3-4 mice for each group. **(D)** Representative traces from lymphatic vessel wall measurements show lymphatic diameter and contraction over time (s,seconds) in uninfected mice and mice infected with WT or *agr* mutant MRSA for 30 days. **(E)** Ejection fraction shows the strength of lymphatic vessel contraction in uninfected mice and mice infected with WT or *agr* mutant MRSA for 30 days. **(F)** Frequency indicates the cpm (counts per minute) of lymphatic vessel contractions in uninfected mice and mice infected with WT or *agr* mutant MRSA for 30 days. For **E and F,** statistical analysis was performed by One-Way ANOVA comparison with Fisher's Least Significance Difference post-hoc analysis. Error bars show mean ± s.e.m.

Appendix

Cover Nature Protocols August 2017 Volume 12(8)

Discussion

Eelco F.J. Meijer

The lymphatic system drains fluid and metabolic waste from tissues and provides a route for antigen and antigen presenting cells to move from tissue to lymph nodes where systemic immune responses can be initiated. When the lymphatic system becomes dysfunctional, immune function is impaired (including clearing infections) and the ability to maintain fluid balance and tissue homeostasis is compromised. Both lymphatic vessels and lymph nodes are of paramount importance in keeping the system fully operational. The role of the lymphatic system has been implicated in a wide array of extremely clinically relevant diseases, including inflammatory settings like bacterial infections, lymphedema, cancer and cancer metastasis [1]. To do this end, the research presented in this thesis addresses several critical unmet needs by developing and implementing novel imaging methods for studying both lymphatic vessels and lymph nodes in health and disease.

In **chapter 2**, we describe the microsurgical preparation and implantation of a chronic lymph node window (CLNW) of the murine inguinal lymph node to facilitate imaging of the lymph node in physiological and pathological settings [2]. Our protocol demonstrates how the inguinal LN has minimal morphological, cellular and biochemical changes for the first 14 days after CLNW implantation and how significant movement of the lymph node can be prevented after CLNW implantation and during imaging sessions. However, slight rotational changes cannot always be avoided hence using an imaging method that can acquire images in both horizontal and vertical axes will guarantee to be able to identify the same imaging region. We show that after these 14 days, mild inflammation and gradual loss of perfusion in cortical blood vessels becomes apparent, and therefore we would not recommend imaging the CLNW past 14 days. In addition, the CLNW provides visual access predominantly to the lymph node cortical region, although deeper regions can be visualized depending on the imaging method used. Altogether, we demonstrate by providing examples of images and videos how imaging modalities can be used to investigate lymph node anatomy, metastasis formation and (cancer) cell movement and interactions within 14 days after CLNW implantation.

Measurements of transvascular transport have been proven invaluable in studying numerous *in vivo* processes, including vascular abnormalities and treatments in disease states like cancer and inflammation [3]. In **chapter 3**, we summarize methods to measure transvascular transport as we describe a method for estimating effective vascular permeability (EVP) using *2D* imaging [4-6], as well a recently developed *3D* method using multiphoton microscopy [7, 8] which we optimized. This *3D* method yields a more realistic measurement of EVP. In contrary to the *2D* method for calculating EVP, all vessels are mathematically considered as a single vessel in the *3D* method. A downside of this approach is that permeability differences among single vessels cannot be estimated. However, the result (mean over all vessels) is more accurate if the vessel masking is adequate. Another advantage of this *3D* method is that it is optimized for both subcutaneous tumor imaging using a dorsal skinfold chamber and lymph node imaging using the CLNW, although other tissues might need slightly altered acquisition settings or image processing steps for an accurate vessel mask.

In vivo assessment of lymph transport has proven extremely challenging. Yet, accurate *in vivo* measurements of lymph flow velocity and lymph volumetric flow will be critical in understanding disease processes. Several methods have been developed to look at specific parameters of lymphatic functioning like contractions [9], valve functioning and fluid transport [10-12], however

they intrinsically change the parameters to be measured by their obligatory use of exogenous labels and cannot directly quantify lymph flow. In addition, because the lymphatic network is filled from the periphery, lymph cannot be labelled simultaneously all throughout the body and label concentrations will inherently differ depending on the distance from the injection site. Therefore, in **chapter 4**, we developed a method that allows direct label-free measurement of lymph flow *in vivo* by Doppler optical coherence tomography (DOCT) [13, 14]. Although DOCT is already used to measure velocity and flow in blood vessels [15] and video microscopy can be used to measure cell transport in lymphatic vessels [16], measuring actual lymph was not accomplished in lymphatic vessels because of the small signal-to-noise ratio (SNR) of lymph compared to blood. First, we developed an algorithm that could discriminate between static (tissue) and moving signals (lymph) using a short-time Fourier transform on the complex scattering signal and subsequently fitting each spectrum within the spectrogram to a parametric model comprising two Gaussians and a white noise background. In short, the center position of the Gaussian describing the spectrally broad signal estimates the Doppler shift induced by (and linearly correlated to) lymph flow. The time-invariant Gaussian centered on time 0, represents the static signal from the immobile tissue. Secondly, we performed simultaneous measurements with DOCT and a previously described fluorescence photobleaching method to validate and calibrate our method in the mouse ear. Thirdly, we performed the first direct and label-free depth-resolved measurements of pulsatile lymph flow velocities *in vivo*. These were acquired in collecting lymphatic vessels at a single location without injecting any (i.e. fluorescent) label. The temporal resolution was set at 0.25 s with a sampling rate of 50 kHz (our system limit). We subsequently altered the acquisition to a sinusoidal scan pattern at 1.04 kHz with a 0.96 s temporal resolution so we could additionally acquire vessel diameter changes, which enabled us to calculate the actual lymph flow from the transverse flow velocity profile and the luminal segmentation.

A drawback of this approach (and other lymphatic imaging methods) is the limited imaging depth, which requires resection of the skin prior to imaging. DOCT has an imaging penetration of approximately 2-10 mm, but even within this range signals attenuate rapidly with depth and because of the small SNR of lymph, a loss of signal is undesirable and leads to inaccurate measurements. Nevertheless, this method using DOCT advances the field of lymphatic research by enabling single-location label-free, high-speed, and simultaneous measurements of lymphatic contraction, lymph flow velocity, and lymph volumetric flow in collecting lymphatic vessels.

In **chapter 5** we describe additional modifications to the DOCT experimental setup, thereby extending the technique to support the simultaneous measurement of flow and contraction in three neighboring lymphangions and the status (i.e., open vs closed) of the valves present in-between each lymphangion [17]. Using the same 50 kHz system for image acquisition, the duration of the five measurements together is 430 ms, which is effectively simultaneous and sufficient to objectify lymphatic flow and contractile dynamics. We demonstrate the usefulness of this method in both normal mice and in a model of sterile inflammation.

However, to allow for sufficient spatial resolution and measurement locations, the temporal resolution had to be improved by injecting Intralipid and therewith improving the SNR. While this would be a problem when looking at physiologic lymph velocity and flow, for studying cooperation between neighboring lymphangions the injection does not interfere since conditions are equal. Improving the system sampling rate (>50 kHz) could also remove the need for injected

materials. From these experiments, we confirm that valves are biased-open and that valves may stay continuously open during pumping and retrograde flow, similar to what has been observed in other *ex vivo* and computational models [18-26]. Valve closings are a rare event in our experiments. Generally, we observe simultaneous contractions and flow peaks in the three successive lymphangions, although these contractions might be quasi-synchronous and an occasional phase shift was observed. These findings tremendously improve our insights to lymphatic vessel functioning and provide the framework for further studies to fully understand lymphangion and valve synchronicity.

Disease recurrence in cancer patients initially diagnosed without nodal metastasis or with nodal micrometastases is common, even if they underwent systemic therapies. This shows systemic therapy does not always eradicate small pockets of cancer cells [27]. Furthermore, in the pre- and micro-metastatic setting no lymph node angiogenesis has been reported [28] and lymphoid tissues (spleen, lymph nodes, and gut-associated lymphoid tissues) have been identified as pharmacologic sanctuaries from anti-retroviral therapy [29, 30]. Taken together, we hypothesized that micrometastases and isolated metastatic cancer cells might similarly find pharmacologic sanctuary from chemotherapy, even in the case of normal lymph node blood vasculature. Studying lymph node blood vasculature might therefore give insights into why systemic cancer therapies fail. In **chapter 6**, we utilized the CLNW [2] and the method to measure EVP [31] (as described in chapters 2 and 3, respectively) to investigate physiologic lymph node EVP and whether altering EVP can improve chemotherapy penetration in the murine lymph node [32]. We performed the first measurements of physiologic lymph node EVP and found that lymph node EVP can be increased ~fourfold by VEGF-A treatment, although not resulting in a significant increase in the maximum drug concentrations of chemotherapeutic drugs (with varying drug properties) as measured by high-performance liquid chromatography. A likely explanation could be that fluid flux through the lymph node can cause washout of drugs, which may dominate vascular permeability as the main determinate of drug accumulation.

From these findings, we hypothesize that increasing lymph node blood vessel EVP is unlikely to increase therapy effectiveness of the various tested chemotherapy drugs without changing their drug properties, reducing drug washout, and/or specific lymph node blood vasculature targeting instead of systemic altering of EVP. In addition, current and future studies can be repeated in the pre- and micro-metastatic setting and perhaps methods can be developed to measure direct lymph node drug efflux to improve our understanding of the fate of injected (chemotherapeutic) drugs. To this end, more research on the subject can be performed to eventually improve therapies targeting metastatic lesions in the lymph node.

Chapter 7 describes how Methicillin-Resistant *Staphylococcus aureus* (MRSA), a frequent cause of skin and soft tissue infections (SSTIs) in patients [33] resulting high morbidity and costs, causes chronic decreased lymphatic function. Using direct fluorescence and DOCT imaging, we show reduction in lymphatic vessel contractility and lymph flow after MRSA infection in the mouse hindlimb, even long after MRSA is cleared and inflammation is resolved. To unravel the responsible mechanism, we hypothesized based on previous work [34-36] that nitric oxide (NO) produced by infiltrating cells during MRSA infection could disrupt the temporal and spatial NO gradients established by lymphatic endothelial cells that are required for sustained lymphatic contraction. However, depletion of the infiltrating cells worsened the phenotype. Therefore, we

tested whether MRSA-derived lipoteichoic acid could be responsible for the phenotype. While inhibiting lymphatic contraction, we found that LTA did so through inducible nitric oxide synthase (iNOS). However, MRSA infected iNOS knockout mice still showed decreased lymphatic function. Hence, LTA was not primarily responsible for the phenotype. MRSA can also produce bacterial NO, but MRSA lacking the NO synthase oxygenase responsible for its production inhibited lymphatic function as well. Then, since NO could not be identified as the sole mediator of lymphatic dysfunction during MRSA infection, we tried inhibiting inflammatory cytokines (e.g. TNF-α) which were markedly increased during active infection. Using MyD88 null mice, which inhibits toll-like receptor signaling through NFκB, and various non-steroidal anti-inflammatory drugs, no increase in lymphatic function could be identified.

Next, we analyzed the cellular integrity of the lymphatic vessels after MRSA infection. To this end, we performed immunohistochemical staining and used α-smooth muscle actin (αSMA)-DsRed mice to identify smooth muscle cells and lymphatic muscle cells (LMCs) on blood and lymphatic vessels, respectively. We found that during MRSA infection as well as after subsequent bacterial clearance that there was a loss and disorganization of LMCs, which are critical for lymphatic contraction. Using proteomic analysis, several MRSA exotoxins controlled by the accessory gene regulator (*agr*) operon were subsequently identified to be responsible for LMC loss. This demonstrates *agr* to be a promising target in preserving lymphatic vessel function in patients infected with MRSA. While MRSA is a common and extremely virulent pathogen, other bacteria frequently causing SSTIs like *Streptococci* (especially Group A Streptococci) and methicillin susceptible *S.aureus* (MSSA) have not been tested in this study. The slow regeneration of LMCs together with its associated impaired lymphatic and immune function may explain the frequent reinfections that often occur in patients with recurrent SSTIs. In addition to preventing lymphatic muscle cell death, improving LMC regeneration might be a promising approach in these patients.

Altogether, this thesis demonstrates novel imaging methods and their application for studying lymphatic vessel and lymph node physiology and pathology. By employing direct fluorescence imaging, multiphoton microscopy and Doppler optical coherence tomography, our current understanding advanced and available tools expanded in the field of lymphatic research. Future research is needed to further elucidate presented findings and to be able to translate these murine studies to the clinic.

References

1. Padera, T.P., E.F. Meijer, and L.L. Munn, The Lymphatic System in Disease Processes and Cancer Progression. Annu Rev Biomed Eng, 2016.
2. Meijer, E.F.J., et al., Murine chronic lymph node window for longitudinal intravital lymph node imaging. Nat Protoc, 2017. 12(8): p. 1513-1520.
3. Jain, R.K., Transport of molecules across tumor vasculature. Cancer Metastasis Rev, 1987. 6(4): p. 559-93.
4. Gerlowski, L.E. and R.K. Jain, Microvascular permeability of normal and neoplastic tissues. Microvasc Res, 1986. 31(3): p. 288-305.
5. Yuan, F., et al., Microvascular permeability of albumin, vascular surface area, and vascular volume measured in human adenocarcinoma LS174T using dorsal chamber in SCID mice. Microvasc Res, 1993. 45(3): p. 269-89.

6. Yuan, F., et al., Microvascular permeability and interstitial penetration of sterically stabilized (stealth) liposomes in a human tumor xenograft. Cancer Res, 1994. 54(13): p. 3352-6.
7. Brown, E.B., et al., In vivo measurement of gene expression, angiogenesis and physiological function in tumors using multiphoton laser scanning microscopy. Nat Med, 2001. 7(7): p. 864-8.
8. Denk, W., J.H. Strickler, and W.W. Webb, Two-photon laser scanning fluorescence microscopy. Science, 1990. 248(4951): p. 73-6.
9. Liao, S., et al., Method for the quantitative measurement of collecting lymphatic vessel contraction in mice. J Biol Methods, 2014. 1(2).
10. Robinson, H.A., et al., Non-invasive Optical Imaging of the Lymphatic Vasculature of a Mouse. J Vis Exp, 2013(73).
11. Chong, C., et al., In vivo visualization and quantification of collecting lymphatic vessel contractility using near-infrared imaging. Sci Rep, 2016. 6: p. 22930.
12. Szuba, A., et al., The third circulation: radionuclide lymphoscintigraphy in the evaluation of lymphedema. J Nucl Med, 2003. 44(1): p. 43-57.
13. Blatter, C., et al., In vivo label-free measurement of lymph flow velocity and volumetric flow rates using Doppler optical coherence tomography. Sci Rep, 2016. 6: p. 29035.
14. Vakoc, B.J., et al., Three-dimensional microscopy of the tumor microenvironment in vivo using optical frequency domain imaging. Nature medicine, 2009. 15(10): p. 1219-1223.
15. Wang, Y., et al., Pilot study of optical coherence tomography measurement of retinal blood flow in retinal and optic nerve diseases. Invest Ophthalmol Vis Sci, 2011. 52(2): p. 840-5.
16. Dixon, J.B., et al., Measuring microlymphatic flow using fast video microscopy. J Biomed Opt, 2005. 10(6): p. 064016.
17. Blatter, C., et al., Simultaneous measurements of lymphatic vessel contraction, flow and valve dynamics in multiple lymphangions using optical coherence tomography. J Biophotonics, 2017.
18. Davis, M.J., et al., Determinants of valve gating in collecting lymphatic vessels from rat mesentery. American Journal of Physiology - Heart and Circulatory Physiology, 2011. 301(1): p. H48-H60.
19. Rahbar, E. and J.E. Moore, Jr., A model of a radially expanding and contracting lymphangion. J Biomech, 2011. 44(6): p. 1001-7.
20. Bertram, C.D., et al., Consequences of intravascular lymphatic valve properties: a study of contraction timing in a multi-lymphangion model. Am J Physiol Heart Circ Physiol, 2016. 310(7): p. H847-60.
21. Kunert, C., et al., Mechanobiological oscillators control lymph flow. Proc Natl Acad Sci U S A, 2015. 112(35): p. 10938-43.
22. Wilson, J.T., et al., Confocal image-based computational modeling of nitric oxide transport in a rat mesenteric lymphatic vessel. J Biomech Eng, 2013. 135(5): p. 51005.
23. Wilson, J.T., et al., Determining the combined effect of the lymphatic valve leaflets and sinus on resistance to forward flow. J Biomech, 2015. 48(13): p. 3584-90.
24. Jamalian, S., et al., Network Scale Modeling of Lymph Transport and Its Effective Pumping Parameters. PLoS One, 2016. 11(2): p. e0148384.
25. Bertram, C.D., C. Macaskill, and J.E. Moore, Jr., Pump function curve shape for a model lymphatic vessel. Med Eng Phys, 2016. 38(7): p. 656-63.

26. Baish, J.W., et al., Synchronization and Random Triggering of Lymphatic Vessel Contractions. PLoS Comput Biol, 2016. 12(12): p. e1005231.
27. Straver, M.E., et al., Towards rational axillary treatment in relation to neoadjuvant therapy in breast cancer. Eur J Cancer, 2009. 45(13): p. 2284-92.
28. Jeong, H.S., et al., Investigation of the Lack of Angiogenesis in the Formation of Lymph Node Metastases. J Natl Cancer Inst, 2015. 107(9).
29. Thomas, S.N. and A. Schudel, Overcoming transport barriers for interstitial-, lymphatic-, and lymph node-targeted drug delivery. Curr Opin Chem Eng, 2015. 7: p. 65-74.
30. Bourry, O., et al., Effect of a short-term HAART on SIV load in macaque tissues is dependent on time of initiation and antiviral diffusion. Retrovirology, 2010. 7: p. 78.
31. Meijer, E.F., et al., Measuring Vascular Permeability In Vivo. Methods Mol Biol, 2016. 1458: p. 71-85.
32. Meijer, E.F., et al., Lymph node effective vascular permeability and chemotherapy uptake. Microcirculation, 2017.
33. Liu, C., et al., Clinical practice guidelines by the infectious diseases society of america for the treatment of methicillin-resistant Staphylococcus aureus infections in adults and children: executive summary. Clin Infect Dis, 2011. 52(3): p. 285-92.
34. Scallan, J.P. and M.J. Davis, Genetic removal of basal nitric oxide enhances contractile activity in isolated murine collecting lymphatic vessels. J Physiol, 2013. 591(8): p. 2139-56.
35. Liao, S., et al., Impaired lymphatic contraction associated with immunosuppression. Proc Natl Acad Sci U S A, 2011. 108(46): p. 18784-9.
36. Nagai, T., E.A. Bridenbaugh, and A.A. Gashev, Aging-associated alterations in contractility of rat mesenteric lymphatic vessels. Microcirculation, 2011. 18(6): p. 463-73.

Samenvatting in het Nederlands

(Summary in Dutch)

Het lymfestelsel is een essentieel onderdeel in het lichaam, verantwoordelijk voor een goede vochtbalans, het creëren van immuunreacties, alsmede de opname van vetten vanuit de darm. Het disfunctioneren van het lymfestelsel kan lymfoedeem, darm malabsorptie en immuunstoornissen (waaronder infecties) teweegbrengen. Daarnaast is bekend dat het lymfestelsel disfunctioneert bij andere ziektebeelden, zoals recidiverende huidinfecties, sommige neurologische aandoeningen (zoals Multiple Sclerose en de ziekte van Alzheimer), reumatoïde artritis, glaucoom, hypertensie, schildklieraandoeningen, orgaan afstoting en atherosclerose. Ook heeft het lymfestelsel een belangrijke rol bij kanker, omdat kankercellen kunnen uitzaaien via het lymfestelsel en de aanwezigheid van uitzaaiingen veel consequenties heeft voor de prognose en therapiemogelijkheden van een kankerpatiënt. Het is uiterst relevant te beseffen dat het lymfestelsel bij zoveel ziektebeelden een belangrijke rol speelt.

Lymfe is de vloeistof in het lymfestelsel, afkomstig uit de extracellulaire ruimte van weefsels. Het soort weefsel en de processen die zich afspelen in het weefsel bepalen de consistentie van het lymfe. Vloeistof treedt binnen door kleppen in de kleinere lymfevaten, de “initial lymphatic vessels”. Immuuncellen kunnen ook het lymfestelsel betreden via deze kleinere lymfevaten. Lymfe wordt vervolgens getransporteerd via grotere lymfevaten (“collecting lymphatic vessels”) en lymfeklieren, om zo uiteindelijk in de bloedbaan terug te keren. Deze “collecting lymphatic vessels” bevatten gespecialiseerde lymfatische spiercellen en kleppen in het lumen. Transport van lymfe wordt veroorzaakt door een samenspel tussen de inhoud van het lymfevat, de lymfevat kleppen, de zwaartekracht, spierbewegingen van het lichaam en spiercontracties van de grotere lymfevaten. Er bestaan beeldvormingstechnieken om naar het functioneren van lymfevaten te observeren en objectiveren, echter zijn deze technieken niet in staat om alle wetenschappelijke vragen die er zijn te beantwoorden. Hoe lymfevaten precies werken is daarom onbekend.

Om ziektes zoals kanker te kunnen behandelen en nieuwe therapieën te kunnen ontwikkelen of ontdekken, is het bestuderen van zowel het ziektebeeld als de normale fysiologie essentieel. Immers, een abnormale situatie kan pas herkend worden als de normale situatie bekend is. In dit proefschrift worden meerdere wetenschappelijke methoden en wetenschappelijke studies beschreven, welke ontwikkeld en uitgevoerd zijn door mijzelf en collega’s, om onbeantwoorde vragen over de fysiologie en pathologie van het lymfestelsel te kunnen beantwoorden. Beeldvorming van het lymfestelsel staat centraal in onderstaande hoofdstukken.

In **hoofdstuk 4 en 5** wordt het ontwikkelen van nieuwe beeldvormingstechnieken beschreven welke in staat zijn het functioneren van de grotere lymfevaten te objectiveren. Huidige methoden — nabij-infrarood fluorescentie beeldvorming (NIRF), directe fluorescente beeldvorming, en lymfescintigrafie — kunnen naar lymfevat spiercontracties, klepfunctie, en in mate naar vloeistof transport kijken middels injectie van fluorescent materiaal of een radio-isotoop. Echter, het injecteren van vloeistof in de lymfebanen verandert de normale fysiologische situatie in het lymfevat, wat onderzoek naar de normale situatie ernstig beperkt. Daarbij kunnen geen van deze huidige technieken direct de stroomsnelheid meten van lymfe. Door gebruik te maken van Doppler optical coherence tomography (Doppler OCT; DOCT) beschrijven wij in **hoofdstuk 4** een nieuwe methode welke ons in staat stelt om tegelijkertijd lymfestroomsnelheid, spiercontracties en vloeistoftransport te objectiveren in een lymfevat zonder het hoeven injecteren van exogene middelen. **Hoofdstuk 5** demonstreert een doorontwikkeling van deze beeldvormingstechniek, waarin wij beschrijven hoe deze methode gebruikt kan worden om lymfestroomsnelheid,

spiercontracties en vloeistoftransport in meerdere segmenten van het lymfevat te objectiveren, met beeldvorming van tussenin gelegen bewegende lymfekleppen. Deze technieken bieden de mogelijkheid om veel van de huidige wetenschappelijke vragen over de functie van lymfevaten te beantwoorden.

Hoofdstuk 7 demonstreert de waarde van Doppler OCT door disfunctioneren van lymfevaten te objectiveren bij huid- en weke delen infecties door een (klinisch) veel voorkomende pathogene huidbacterie, genaamd *Staphylococcus aureus*. Dergelijke infecties gaan gepaard met hoge morbiditeit, aanzienlijke mortaliteit en hoge kosten. Wij laten zien dat de MRSA (methicilline resistente *Staphylococcus aureus*) huidbacterie zowel acuut als chronische lymfevat disfunctie kan veroorzaken in ledematen in een muismodel, waarbij de schade blijft bestaan nadat het lichaam de infectie heeft geklaard. Naast verminderde contractiliteit en lymfetransport door de disfunctionerende lymfevaten, zien we ook een vermindering van lymfatische spiercellen op de lymfevaten welke normaliter cruciaal zijn voor contractiliteit. Bij verdere analyse vonden wij dat bepaalde MRSA exotoxines (bacteriële gifstoffen) verantwoordelijk zijn voor lymfevat disfunctie en dat deze exotoxines geproduceerd worden door een stuk van het bacteriële DNA genaamd de "accessory gene regulator (*agr*)" operon. *Agr* is daarom een mogelijk doelwit om lymfevat disfunctie en recidiverende infecties te voorkomen bij patiënten met huid- en weke delen infecties. Bij reeds geleden schade aan de lymfevaten zou toekomstig onderzoek naar het regenereren van lymfatische spiercellen mogelijk uitkomst kunnen bieden.

Naast het verbeteren van beeldvorming van lymfevaten, kon het bestuderen van lymfeklieren ook verbeterd worden. Het grondig bestuderen van de (patho-)fysiologie van lymfeklieren werd beperkt, omdat er geen goed muismodel bestond om gedurende meerdere weken beeldvorming van dezelfde lymfeklier te verrichten. Een dergelijk model zou nuttig zijn voor het bestuderen, dan wel behandelen van immuunreacties en ziektebeelden, zoals kanker uitzaaiingen. In **hoofdstuk 2** beschrijven wij het resultaat van een door ons ontwikkeld microchirurgisch model (chronic lymph node window; CLNW) welke het mogelijk maakt om gedurende 14 dagen beeldvorming van dezelfde lymfeklier te kunnen verrichten in een levende muis.

Het is bekend dat kanker uitzaaiingen een slechte prognose geven bij kankerpatiënten en dat meestal de uitzaaiingen de daadwerkelijke doodsoorzaak zijn. Desondanks blijft het moeilijk om uitzaaiingen adequaat te behandelen. De meeste therapieën zijn gericht om de primaire tumor te behandelen en niet de uitzaaiingen die zich hebben genesteld in ander weefsel, waar een kankercel zich bewezen anders zal gedragen en anders zal reageren op therapieën. Bloedvaten verspreiden geneesmiddelen door het lichaam, maar de geneesmiddelen komen alleen in het weefsel terecht als ze ook de bloedbaan kunnen verlaten. Helaas is onderzoek naar geneesmiddel penetratie in lymfeklieren weinig verricht. Om meer inzicht te krijgen in geneesmiddel penetratie, maken wij gebruik van het CLNW tezamen met multifoton microscopie, om een methode te ontwikkelen om driedimensionaal vasculaire permeabiliteit (doorlaatbaarheid) te kunnen meten in de bloedvaten van weefsels (zie **hoofdstuk 3).**

In **hoofdstuk 6** wordt deze methode gebruikt om driedimensionaal de vasculaire permeabiliteit van bloedvaten en de penetratie van chemotherapie in de lymfeklier te meten. Door middel van VEGF-A (een wetenschappelijk veelgebruikt eiwit) laten wij zien dat de vasculaire permeabiliteit veelvuldig verhoogd kan worden in de lymfeklier. Echter, de penetrantie van verschillende

chemotherapeutische middelen wordt hier niet door verbeterd, ondanks de intraveneuze toediening van chemotherapeutica. Deze discrepantie wordt mogelijk verklaard doordat lymfe door de lymfeklier heen stroomt, wat chemotherapeutische middelen als het ware uit de lymfeklier weg kan spoelen. Uit dit onderzoek blijkt dat (alleen) het verhogen van de vasculaire permeabiliteit in de lymfeklier niet voldoende is om chemotherapie effectiever te maken voor het behandelen van lymfeklier uitzaaiingen. Deze nieuwe bevindingen bieden echter wel nieuwe inzichten voor toekomstig onderzoek om medicamenteuze behandeling van lymfeklieren te kunnen verbeteren.

Concluderend demonstreert dit proefschrift de ontwikkeling en mogelijkheden van nieuwe beeldvormingstechnieken om lymfevat- en lymfeklierfysiologie en -pathologie te kunnen bestuderen. Door gebruik te maken van directe fluorescente beeldvorming, multifoton microscopie en Doppler OCT hebben de beschreven hoofdstukken een significante bijdrage geleverd aan de huidige kennis van het lymfestelsel, bijbehorende ziektebeelden en mogelijkheden voor toekomstig onderzoek. Verder onderzoek zal nodig zijn om de vertaalslag naar de kliniek te kunnen maken.

Curriculum vitae auctoris

In 2006, Eelco graduated from the Wolfert van Borselen bilingual secondary school after obtaining his International Baccalaureate English A2 Higher Level and subsequently applied and enrolled at the English-speaking University College Roosevelt (UCR, former Roosevelt Academy). In 2009, he graduated cum laude for the pre-medical program at UCR and applied for the Selective Utrecht Medical Master (SUMMA) in order to pursue his dream of becoming both an MD and researcher. In October 2013, he received his MD and MSc in Clinical Research. From January 2014 until December 2016, Eelco was employed as a Postdoctoral Research Fellow at the E.L. Steele Lab for Tumor Biology (Massachusetts General Hospital / Harvard Medical School) under direct supervision of associate prof. dr. TP Padera. This was concurrently his PhD trajectory for University Utrecht, during which he conducted the research described in this thesis under supervision of promotor prof. dr. IHM Borel Rinkes and co-promotors dr. J Hagendoorn and associate prof. dr. TP Padera. In 2017, Eelco returned to the clinic as a surgical resident. He is currently employed at *Gelderse Vallei Hospital*, the Netherlands.

Invited speaker

- Gordon Research Conference: Lymphatics. Title: *Label-Free In-Vivo Measurement of Lymph Flow Velocity using Doppler Optical Coherence Tomography.*

Publications (chronological order)

- Jones, D., et al. Methicillin-resistant Staphylococcus aureus pathogenicity causes sustained lymphatic dysfunction. Sci Transl Med. 2017. In Press.
- Lippok, N., et al. Definitive depolarization signatures in nanomedicine. Nat Phot. 2017. In Press.
- Meijer, E.F.J., et al., Murine chronic lymph node window for longitudinal intravital lymph node imaging. Nat Protoc, 2017. 12(8): p. 1513-1520.
- Blatter, C. & Meijer, E.F.J., et al., Simultaneous measurements of lymphatic vessel contraction, flow and valve dynamics in multiple lymphangions using optical coherence tomography. J Biophotonics, 2017.
- Meijer, E.F., et al., Lymph node effective vascular permeability and chemotherapy uptake. Microcirculation, 2017.
- Ubink, I., et al., Surgical and Oncologic Outcomes After Major Liver Surgery and Extended Hemihepatectomy for Colorectal Liver Metastases. Clin Colorectal Cancer, 2016. 15(4): p. e193-e198.
- Padera, T.P., E.F. Meijer, and L.L. Munn, The Lymphatic System in Disease Processes and Cancer Progression. Annu Rev Biomed Eng, 2016. 18: p. 125-58.
- Blatter, C., et al., In vivo label-free measurement of lymph flow velocity and volumetric flow rates using Doppler optical coherence tomography. Sci Rep, 2016. 6: p. 29035.
- Meijer, E.F., et al., Measuring Vascular Permeability In Vivo. Methods Mol Biol, 2016. 1458: p. 71-85.
- Hoogstraat, M., et al., Detailed imaging and genetic analysis reveal a secondary BRAF(L505H) resistance mutation and extensive intrapatient heterogeneity in patients treated with vemurafenib. Pigment Cell Melanoma Res, 2015. 28(3): p. 318-23.
- Meijer, E.F., et al., Central inhibition of refractory overactive bladder complaints, results of an inpatient training program. J Pediatr Urol, 2015. 11(1): p. 21.e1-5.

Acknowledgements

Dear prof.dr. Borel Rinkes and dr. Hagendoorn, dear Inne and Jeroen,
You made all of this possible and I cannot be more grateful. You saw my potential and offered me your support to apply for a position in the Padera lab. I never imagined I would end up doing research abroad, especially in a lab this excellent. It has been a superb experience during which I have grown as a professional and as a person. Thank you for responding to my countless updates and all our meetings in person. My sincerest gratitude for your unfathomable support and guidance along the way, whilst being such thoughtful and amazing individuals.

Dear associate prof.dr. Padera, dear Tim,
It must have been a combination of excellent referees and perhaps the easy access to "stroopwaffles and bitterballs", you happily accepted me into your lab. Tim, not only are you extremely good at what you do, you are just as sincere and caring for anyone under your wings. Thank you for your never-ending support, the countless meetings, all the lab gloves I made you wear and the many times you taught me how to fix the microscopes. You showed me the ropes, how research is supposed to be done. I am most grateful for all the lessons learned, for all the late-night emails, and most of all for your trust and time invested in me. I consider it an immense privilege to have worked under the mentorship of such a great scientist, boss and person.

Dear MGH/HMS collaborators, dear prof.dr. Jain, associate prof.dr. Vakoc, prof.dr. Baish, associate prof.dr. Fukumura, associate prof.dr. Munn, assistant prof.dr. Huang, prof.dr. Bouma and prof.dr. Taghian,
It has been an honor and privilege working with such bright minds, true experts in the field. Thank you for all the meetings, the intellectual discussions, and knowledge conveyed. It has been a fruitful collaboration.

Dear dr. Koudijs, prof.dr. de Jong and prof.dr. Cornelisse,
My utmost gratitude for seeing my potential so early on in my career. You inspired me and created my enthusiasm for science. Thank you for your support during my MD training and my time in Boston.

Members of the thesis committee, dear prof.dr.ir. Lagendijk, prof.dr. Kranenburg, prof.dr. van Gulik, prof.dr. Friedl, and prof.dr. van Hillegersberg,
Thank you for taking place in my thesis committee.

Dear Boston friends, roommates and colleagues, dear Justin, KB, Noah, Cedric, Dmitriy, Dennis, Echoe, Ethel, Keehoon, Koen, Ruoxu, Christina, Jonas, Stephany,
It has been so much fun these last couple of years! Thanks guys for all the laughs, discussions, coffees, dinners, PC, road trips and beers. I know some of you won't be able to make it Dec 1, but the offer to visit the Netherlands will always stand. Thank you all for your kindness and friendship, I hope to see each other soon. Special thanks to dr. Dmitriy Kedrin, thanks buddy for the amazing cover artwork!

Dear colleagues of the E.L. Steele Lab, dear Julia Kahn, Sylvie Roberge, Elizabeth Garzon and Phyllis McNally, thank you for all the help and support throughout the years. Not to forget the many lab happy hours we hosted and the fun Steele Lab annual retreats. You keep the lab running! Dear Meenal, Gino, Giorgio, Ivy, Liz and other fellows, grad students, and technicians of the Steele Lab, it has been a pleasure working with you.

Dear colleagues at the Department of Surgery at *Gelderse Vallei Hospital,*
Thank you all for the warm welcome. I look forward to the times ahead.

Dear paranymphs, dear Cedric (dr. Blatter) and Dennis (dr. Jones),
Not only did we pursue (and accomplish!) some great science, we also made countless epic memories. You were of paramount importance to making my time in Boston a success, both personally and professionally. Friends, I look forward to having you stand beside me during my defense.

Dear friends and family,
So many people wondered where that infinite supply of Dutch cheese and stroopwaffles came from! Thank you for the all the messages, the visits, and most of all happily awaiting my return.

Dear Mom and Dad,
Ever since I can remember you were there for me, 24/7, no exceptions. Dad, you even flew to the USA to secure my apartment when the US consulate could not deliver my visa on time. That also meant you had to spend New Year's Eve alone, during a blizzard, yet nothing could stop you. Thank you for always being there for me, guiding me to who I have become and what I have achieved. Thank you for your love and support.

Dear Ralph,
Despite the US-European time difference, we spoke and laughed just as much. I am lucky to have you as my brother.

Dear Jelena,
Last but not least. I am happy to have you by my side.